# ABSTRACT

Title of dissertation:     EXPERIMENTAL STUDY OF
                           ENTROPY GENERATION AND
                           SYNCHRONIZATION IN NETWORKS
                           OF COUPLED DYNAMICAL SYSTEMS

                           Aaron Morgan Hagerstrom
                           Doctor of Philosophy, 2015

Dissertation directed by:  Professor Rajarshi Roy
                           Department of Physics


This thesis describes work in two areas: unpredictability in a system with both single photon detection and chaos, and synchronization in networks of coupled systems.

The unpredictability of physical systems can depend on the scale at which they are observed. For example, single photons incident on a detector arrive at random times, but slow intensity variations can be observed by counting many photons over large time windows. We describe an experiment in which a weak optical signal is modulated by feedback from a single-photon detector. We demonstrate that at low photon rates, the photon arrivals are described by Poisson noise, while at high photon rates, the intensity of the light shows a deterministic chaotic modulation. Furthermore, we show that measurements of the entropy rate can resolve both noise and chaos, and describe the relevance of this observation to random number generation.

We also describe an experimental system that allows for the study of large networks of coupled dynamical systems. This system uses a spatial light modulator (SLM) and a camera in a feedback configuration, and has an optical nonlinearity due to the relationship between a spatially-dependent phase shift applied by the modulator, and the intensity measured by the camera. This system is a powerful platform for studying synchronization in large networks of coupled systems, because it can iterate many ($\sim 1000$) maps in parallel, and can be configured with any desired coupling matrix. We use this system to study cluster synchronization. It is often observed that networks synchronize in clusters. We show that the clusters that form can be predicted based on the symmetries of the network, and their stability can be analyzed. This analysis is supported by experimental measurements.

The SLM feedback system can also exhibit chimera states. These states were first seen in models of large populations of coupled phase oscillators. Their defining feature is the coexistence of large populations of synchronized and unsynchronized oscillators in spite of symmetrical coupling configurations and homogeneous oscillators. Our SLM feedback system provided one of the first two experimental examples of chimera states. We observed chimeras in coupled map lattices. These states evolve in discrete time, and in this context, "coherence" and "incoherence" refer to smooth and discontinuous regions of a spatial pattern.

# EXPERIMENTAL STUDY OF ENTROPY GENERATION AND SYNCHRONIZATION IN NETWORKS OF COUPLED DYNAMICAL SYSTEMS

by

Aaron Morgan Hagerstrom

Dissertation submitted to the Faculty of the Graduate School of the
University of Maryland, College Park in partial fulfillment
of the requirements for the degree of
Doctor of Philosophy
2015

Advisory Committee:
Professor Rajarshi Roy, Chair/Advisor
Professor Thomas E. Murphy, Co-Advisor
Dr. Louis M. Pecora
Professor Christopher Jarzynski
Professor Daniel Lathrop
Professor Edward Ott

# Table of Contents

# List of Figures

# Chapter 1:   Introduction

Like many important concepts in science, chaos was discovered several times. Poincaré encountered chaos while studying the three-body problem in orbital dynamics [1] in the early 20th century. Chaos was also experimentally observed in the sinusoidally-driven van der Pol oscillator 1927, and described mathematically in this context the 1950s [2, 3]. One of the first scientists to realize the far-reaching importance of chaos was Lorenz, who discovered chaos while working on a simplified model of convection in the atmosphere. His paper from 1963, *Deterministic Nonperiodic Flow* [4] described many ideas that are central to the modern understanding of chaos, including dissipative dynamics in phase space, the fractal structure of attractors (which he described in a qualitative way), and sensitivity to initial conditions. This sensitivity to initial conditions is the property of chaos that allows for random number generation.

The idea that chaos can be used to generate random numbers is old – older than the use of the word "chaos" to describe unpredictable nonperiodic motion in deterministic systems. The word "chaos" has been in use since 1975 [5], although its meaning has evolved somewhat over the years [6].

In 1947 [7, 8] Ulam and von Neumann showed that the logistic map,

$$x_{t+1} = 4x_t(1 - x_t), \tag{1.1}$$

generates one bit of information with every iteration. They introduced the change of variables $x_t = \sin^2(\pi z_t)$, and showed that Equation 1.1 has an explicit solution.

$$z_t = 2^t z^0 \bmod 1 \tag{1.2}$$

This solution gives a concrete example of how a deterministic system can generate information. If the initial condition, $z^0$, is written in binary, then, according to Equation 1.2, the decimal place is moved to the right one place for each iteration. The trailing, insignificant digits of $z$ become more significant as time passes. If, at each iteration, one reads out the binary digit to the right of the decimal place, one will find a string of random bits that is as unbiased as a fair coin. There are specific values of $z^0$ for which this is not the case, for example 0.11111111111111..., and 0.10101010101010...., but almost all real numbers on the interval [0,1] have as many 0's as 1's, and in general, an equal number of occurrences of the bit patterns of length $d$. In other words, almost all real numbers have one bit of entropy per binary digit [9]. By amplifying differences in initial conditions, chaos makes these insignificant trailing bits of information large enough to measure [10].

## 1.1   Entropy generation in a photon-counting feedback loop

Since in 2008, chaotic semiconductor lasers have been used to generate random numbers [11]. These systems are appealing for (at least) two reasons. First, they

are fast (on the order of $10^9$ to $10^{12}$ bits per second) [12]. Second, random bits generated by physical processes offer additional cryptographic security compared to pseudorandom algorithms because their unpredictability can be attributed to a fundamentally unpredictable physical process.

Not all physical random number generators are based on chaos. Another, much longer used, physical source of unpredictability is the detection of single photons [13, 14]. Several commercial devices, which are marketed as "quantum random number generators" are currently being sold [15], which are based on weak light sources and photon-counting detectors. One scheme employs a beam splitter and two detectors, so that whenever a photon arrives, one detector or the other detects the photon, yielding either a 0 or a 1. Another scheme involves harvesting entropy from the random time intervals between photon arrivals [16].

In this thesis, we describe an experimental system with unpredictability due to both chaotic dynamics and discrete photon arrivals. It similar to earlier opto-electronic feedback loops [17, 18]. These feedback loops are known to have complex dynamics that can be tuned anywhere between fixed points and high-dimensional chaos, and whose timescales can be tuned over a wide range [19, 20]. By incorporating a photon-counting detector, we are able to observe a transition from shot noise to chaos with increasing photon rate. Furthermore, we find that the type of unpredictability we observe – shot noise or chaos – depends on our scales of observation in both time and value.

These results have immediate relevance to physical random number generation. Usually, physical random number generators are evaluated based on their

ability to produce bit streams free of bias and correlation [21, 22]. Physical systems usually have both bias (for example, non-identical detectors) and correlation (dynamical correlation times, finite detector bandwidth). In practice, post-processing is very often employed to improve the statistical properties of a noise source. It can be difficult to assess whether the entropy in the resulting bit stream should be attributed to the physical noise source or the post-processing procedure. Furthermore, the designer of a physical random number generator must decide how frequently to sample their system and to what resolution they should measure it. So, they should be aware of the effect of coarse graining on the entropy rate of their system. We show that the scaling of the entropy rate with sampling resolution can be attributed to either chaos or shot noise depending on the photon count rate and sampling resolution.

## 1.2    Synchronization in networks of coupled dynamical systems

Often, networks of coupled dynamical systems will synchronize in clusters. Up until a few years ago, only anecdotal examples could be analyzed in detail [23–26]. We show here that the symmetries of a network can be used to predict the clusters that form in an arbitrary network. The master stability function formalism has proven to be a very useful paradigm for the study of global synchronization in networks of coupled systems [27]. This technique examines the linear stability of the globally-synchronous solution. We present here the linear stability analysis of cluster synchronization, and show that the symmetries of a network can be used to

determine a coordinate transformation that vastly simplifies the this analysis. Now, due to work presented here, it is possible to predict and analyze the stability of a great number of cluster-synchronous states in a given arbitrary network. We also present an experimental verification of the predictions made by this technique. In the experiment, a novel bifurcation called "isolated synchronization" is observed, where a single cluster looses synchrony while others remain synchronized. This bifurcation can also be explained in terms of the symmetries of the network.

In larger networks, one is often interested in dynamical behaviors that persist in the the "thermodynamic limit", where the number of oscillators becomes infinite. The Kuramoto model of coupled phase oscillators [28] is particularly appealing because it can be shown analytically that in the thermodynamic limit a population of phase oscillators undergoes a phase transition from unsynchronized to synchronized behavior with increasing coupling strength.

In the early 2000's, it was realized that in certain coupling configurations, Kuramoto oscillators could form "chimera states" in which there were coexisting synchronized and unsynchronized populations [29–31]. It was not until 2012 that such states were observed in experiment [32,33]. Now, there are several quite diverse experimental examples of chimera states [32–38]. Here, we describe one of the first two experimental observations of chimera states.

## 1.3 Organization of this thesis

Chapter 2 describes the photon-counting feedback loop. The operation of the components in the loop will be described, as well as some details of the digital implementation of the signal processing and data acquisition. Finally, the transition between shot noise and deterministic chaos will be described, and illustrated by examining time series plots, Poincaré sections, autocorrelation functions, and the growth of the variance in the number of photon counts with the counting time window.

Chapter 3 describes the quantification of entropy production in the photon-counting feedback loop. This chapter also contains brief descriptions of some basic concepts from information theory, and a couple of different analyses of the entropy rate of a Poisson process. This material, while not new, provides an illustration of important concepts and a point of reference for understanding the experimental results. The main goal of this chapter is to show that the entropy rate of the photon counting feedback loop reflects chaos at large scales and high photon rates, and shot noise at small scales and low photon rates.

Chapter 4 describes cluster synchronization. A lot of space will be devoted to describing the linear stability analysis of the cluster-synchronous state, and how the symmetries of the network are crucial in predicting with clusters form and analyzing their stability. We experimentally demonstrate cluster synchrony in a few networks. In one of these networks, the symmetries are far from obvious, and we show that computational group theory can be used to analyze cluster synchrony in

this network. In another network, the symmetries are obvious by inspection, and we use this network as an example to show both the diversity of possible patterns and the method for predicting them and analyzing their stability.

Chapter 5 describes an experimental observation of chimera states. These chimera states exist in a coupled map lattice, and have some qualitative similarities and differences compared with chimera states in populations of phase oscillators. A one-dimensional and a two-dimensional version of the same system are be compared, and a few basic theoretical results are be given.

Chapter 6 presents a list of questions. These are ideas that arose during our investigation that I did not have time to pursue.

## Chapter 2: Photon Counting Optoelectronic Feedback Loop

## 2.1  Overview

This chapter describes an optoelectronic feedback loop in which noise due to discrete photon arrivals plays an important role in the dynamics. The chapter proceeds as follows: Section 2.2 describes the motivation for this experiment, and highlights some previous work on similar experimental systems in order to provide some historical context. Section 2.2.1 describes the the configuration of the feedback loop, and describes the difference between this experiment, which incorporates noise from individual photons, and earlier experiments. Section 2.3 describes the digital signal processing and data acquisition in this experiment. Section 2.4 describes how the photon statistics change from Poisson statistics to low-dimensional chaos as the photon rate increases, and how different scales of observation resolve different features of the dynamics. The next chapter discusses entropy production in this

system in the wider context of random number generation.

## 2.2   Motivation and background

In many situations, continuous variables are used to model processes which are comprised of many individual, random occurrences. For example it is common to model the birth and death of organisms in a population by differential equations [39]. Another example is the arrival of individual photons at a detector [40], which is often both modeled and measured as a continuously variable intensity. It is often the case that both large scale deterministic fluctuations and small scale noise are present. We have constructed a model system in which small-scale shot noise from individual photon arrivals is coupled to large scale chaotic dynamics. We describe how the unpredictability of this system depends on the scale at which it is observed. At small scales, we resolve individual photon arrivals, and at large scales we resolve low-dimensional deterministic dynamics. This chapter quantifies the scale dependence in terms of the autocorrelation function, the distribution of photon arrivals in a time window, and the dependence of the variance of this quantity on the time window. The next chapter describes how entropy production in this system reflects both processes.

The experimental system we discuss in this chapter is modeled after earlier experiments with optoelectronic feedback loops. Optoelectronic feedback loops have become a widely-used test bed to study many concepts in nonlinear dynamics [17]. They have several features that make them appealing as a model system:   the

timescales, dimensionality and Lyapunov spectra of their dynamics can be tuned over a wide range, they are well-modeled by a fairly simple delay-differential equation, and they can be constructed from widely-available telecommunications components. The wide bandwidth and separation of timescales possible in these systems allows for breathers [19, 20], and a multistability between a large number of periodic modes [41]. The high dimensionality of these systems allows them to exhibit chimera states [38], and allows for their use in reservoir computing [42]. Optoelectronic feedback loops have been used to demonstrate high speed chaos-based communication over existing fiber optic telecommunications infrastructure [43]. Finally, optoelectronic oscillators have been used extensively as a model system to study the synchronization of networks of coupled chaotic systems [18, 44–46].

The complex dynamics displayed by optoelectronic feedback loops are due to four features of their dynamics: feedback with gain, time delay, filtering, and nonlinearity. These are common features of a variety of oscillators. Feedback with gain is a way of continually injecting energy into a system to ensure that the dynamics do not decay into a trivial state. Feedback loops will typically have a finite bandwidth, and these bandwidth limitations can often be modeled as a filter. We introduced a filter using digital signal processing, but this is not necessary in all situations [19]. Time delay, which we denote here as $T_d$, is often due to finite propagation time for signals. Some implementations of optoelectronic feedback loops use long optical fibers or coaxial cables [17, 19]. Here, we implement delay using digital processing. Time delay allows for high-dimensional dynamics. The phase space of a time-delayed system is infinite-dimensional, because, in order to determine the time

10

evolution of a system with time-delayed feedback, one must know the history of its previous behavior over an interval of time. The initial condition is a function of time, rather than a point in phase space. Finally, there must be some nonlinearity present in order for the existence of chaos. Nonlinearities are usually present in feedback loops. If the feedback gain is too low, the loop cannot oscillate, and small perturbations will decay to a trivial fixed point. If the feedback gain is large enough, oscillations will grow until their growth is limited by some mechanism. Such a mechanism necessarily "turns on" when the amplitude of oscillations is large. This kind of amplitude dependence is not found in linear differential equations. In our optoelectronic feedback loop, a Mach-Zehnder modulator (MZM) imposes a sinusoidal nonlinearity.

The construction of optoelectronic feedback loops is documented in detail in the PhD theses of Adam Cohen [47], Bhargava Ravoori [48], Caitlin Williams [49], as well as in several papers [17,18]. In the interest of brevity, I will not go into great detail on the aspects of this work that are well-documented by earlier publications. Instead, I will focus on what is new in this work, namely feedback based on discrete photon arrivals.

## 2.2.1 Discrete and analog dynamics

The optoelectronic feedback loop we describe in this chapter differs from the previous experimental systems in that it incorporates a photon-counting detector whereas other experiments incorporate analog photodetectors. Thus, the discrete,
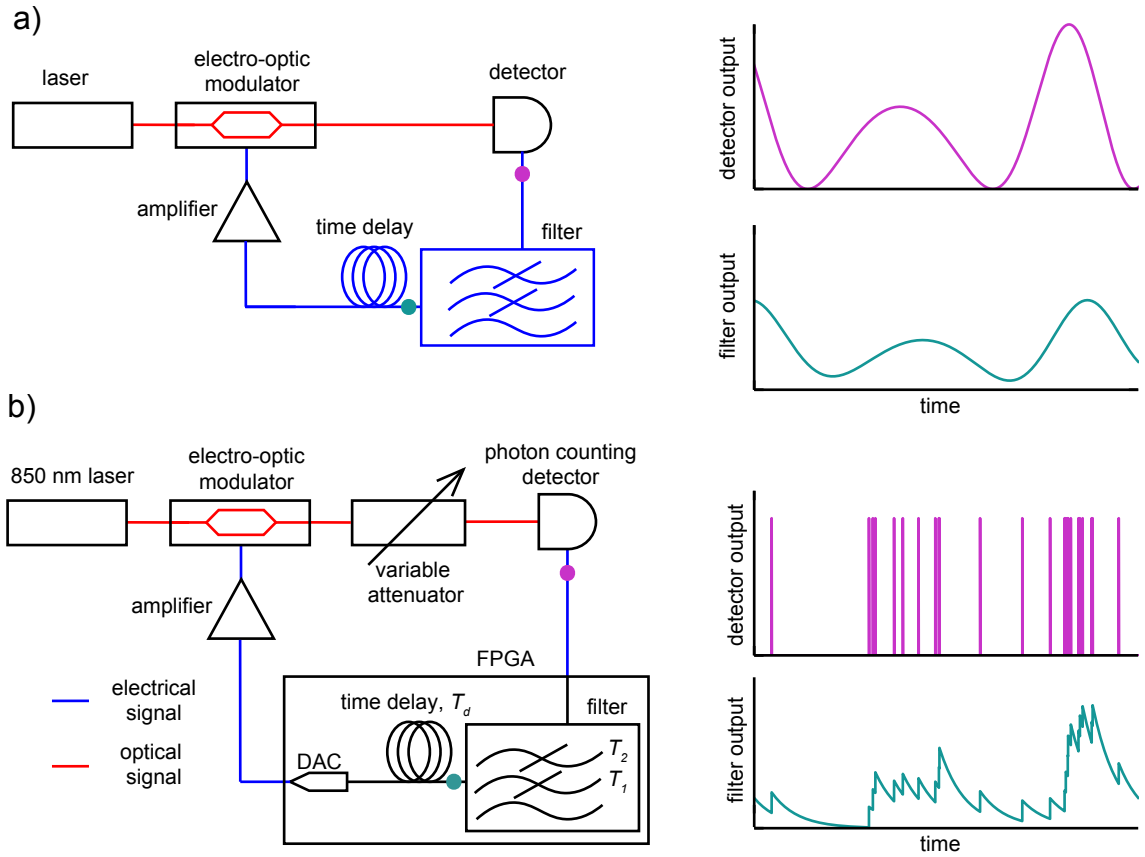
Figure 2.1: Schematic configuration of optoelectronic feedback loops with an analog photodetector a), and photon-counting detector b). Qualitative sketches of the temporal behavior of the detector output and the filter output are also shown. With an analog detector, the signal from the detector is a smooth function of time. The signal from the photon-counting detector is a series of sharp voltage pulses. The filter outputs are roughly similar on a large scale between the two systems, but the discreteness of the photon counts is visible.

stochastic individual photon arrivals are coupled with the deterministic dynamics of the feedback loop.

Figure 2.1 shows a schematic the two types of optoelectronic feedback loops, both with an analog detector (2.1a) and a photon-counting detector (2.1b). Light from a fiber-coupled continuous-wave laser passes through the MZM. The MZM modulates the optical power of the transmitted light $(P)$, according to the applied voltage $v$, so that there is a sinusoidal relationship between the transmitted optical power and the applied voltage: $P = P_0 \sin^2(\alpha v + \phi)$. The optical power transmitted through the modulator is then detected by a photodetector.

In the analog feedback loop shown in Figure 2.1a, the voltage signal from the photodetector is proportional to the optical power $v_{mod}(t) \propto P(t)$. This signal is delayed and processed by a filter, and the filter output $v(t)$ drives the modulator. The equations of motion for a deterministic optoelectronic feedback loop can be cast in this form [18]:

$$
\frac{d\boldsymbol{x}}{dt} = \boldsymbol{E}\boldsymbol{x} + \beta\boldsymbol{F}I(t)
$$
$$
I(t) = \sin^2\left[\boldsymbol{G}^T\boldsymbol{x}(t - T_d) + \phi\right]
$$

(2.1)

Here, $\boldsymbol{x}$ is the state variable of a linear, time invariant filter, matrix $\boldsymbol{E}$ and the vectors $\boldsymbol{F}$ and $\boldsymbol{G}$ describe the characteristics of the filter, $I(t)$ is the normalized intensity of light transmitted through the MZM, and $T_d$ is the time delay. The round-trip gain is denoted by $\beta$. When a photon-counting detector is used in place of an analog photodiode, as shown in Figure 2.1b, the filter variables can be modeled by a linear differential equation driven by discrete photon arrivals.

$$\frac{d\boldsymbol{x}}{dt} = \boldsymbol{E}\boldsymbol{x} + \beta\boldsymbol{F}\frac{1}{\lambda_0}\sum_{i=1}^{\infty}\delta(t - t_i) \qquad (2.2)$$

When modeling this system, the photon arrivals times, $\{t_i\}$, are generated by a non-stationary Poisson point process whose rate, $\lambda(t)$, depends on the state of the filter variables.

$$\lambda(t) = \lambda_0 I(t) = \lambda_0 \sin^2\left[\boldsymbol{G}^T\boldsymbol{x}(t - T_d) + \phi\right]. \qquad (2.3)$$

Figure 2.1 also qualitatively compares the dynamics of the filter variables as given in Equations (2.1) and (2.2). In the deterministic system shown in Figure 2.1a, both the time variation of the intensity and the filter output are smooth functions. In the photon-driven system shown in Figure 2.1b, the detector produces sharp voltage pulses whenever a photon hits it. The filter output is driven by these pulses, the discrete nature of the photon arrivals is reflected in the sharp edges of the filter output. Still, the shape of the filter output in Figure 2.1b is qualitatively similar to Figure 2.1a, at least on a coarse scale. One might expect that as the incident photon rate $\lambda_0$ increases, the dynamics of these two systems become increasingly similar.

## 2.2.2 Components of the feedback loop

In our experiment, the light source is a narrow-linewidth distributed-feedback laser with a wavelength of 850 nm. The laser is operated well above threshold, and produces a continuous wave (CW) output. The laser is coupled into a single-mode (SM) optical fiber.

After passing through the modulator and attenuator, the light is coupled into the photon counting detector. The laser wavelength of 850 nm was chosen because silicon detectors have high sensitivity in this range. We used a Geiger-mode avalanche photodiode. The dead time of this device was about 100 ns, and the dark count rate was about 100 counts/s. The dead time and dark counts limit the dynamic range of the detector. We can resolve photon rates from about $10^2$ counts/s to $10^7$ counts/s.

The light from the laser is coupled into a Mach-Zendher modulator. The power of the light exiting the modulator is related to the applied voltage by

$$P(t) = P_0 \sin^2 \left( \frac{\pi v}{2V_\pi} + \phi \right). \qquad (2.4)$$

For our modulator, $V_\pi$ is 1.6 V. The rate of photon arrivals at the detector is given by:

$$\lambda(t) = \lambda_0 \sin^2 \left( \frac{\pi v}{2V_\pi} + \phi \right) \qquad (2.5)$$

In our implementation, the filter and time delay are implemented digitally using a field-programmable gate array (FPGA). The FPGA is an Alterra Cyclone II, and it is incorporated into a KNJN Saxo-Q acquisition board. In addition to the FPGA, the Saxo-Q board has two 10-bit digital-to-analog converters (DACs) with a maximum speed of 165 MSa/s, as well as four digital-to-analog converters (ADCs) with a maximum speed of 200 MSa/s. This board also has a USB2 interface, which is used to configure the device, and communicate between a PC and the FPGA. We use the USB to set the values of filter variables and transmit photon arrival time

data to the computer.

The amplifier is a simple non-inverting amplifier with a feedback resistance of 27 kΩ, a resistance to ground of 1 kΩ, and a fixed gain of 27. Signals with sharp edges cause this amplifier to introduce ringing artifacts. To avoid this ringing, we used the two-pole filter described in the next section, whose impulse response does not have a sharp rising edge.

## 2.3   Digital Implementation on FPGA

The filtering in our system, as well as the time delay, are implemented digitally on the FPGA. In order to perform these operations, the FPGA must record each photon arrival. The photon arrival times offer the highest possible resolution of the time evolution of the system. For this reason, the FPGA is configured to transmit the photon arrival time data to a PC over a USB connection so that it can be stored. It is also convenient to have the FPGA be able receive the values of parameters over USB, so that these values can be set by computer without hard-coding them into the verilog code. This section describes how the FPGA detects photons, updates the filter variables, performs a time delay, and transmits photon data to the computer on a high level. Major design choices are justified, but low-level details of the implementation are not.

## 2.3.1 Photon Detection and Time delay

When a photon is detected by the photon-counting detector, the detector generates a TTL pulse. We connected the output of the photon-counting detector to an input pin of the FPGA, and the FPGA can be configured to update the value of a register whenever the detector generates a pulse. In practice, it was helpful to implement a deadtime in the software running on the FPGA, in order to prevent the same photon from being registered more than once. The detected photon data is then digitally time delayed, in order to introduce a time delay into our feedback loop. This delay was accomplished using a shift register.

In digital signal processing, all quantities are updated in discrete time, usually dictated by the rising or falling edge of a clock signal. A shift register is a convenient way to implement a delay in discrete time. A shift register consists of a series of locations in memory: $Y_0 \ldots Y_{N_d-1}$, where $N_d$ is the time delay in clock cycles. The value at the $i$th location at the end of the $n$th clock cycle is denoted $Y_i[n]$. On each clock cycle, each location except for $Y_{N_d-1}$ is updated by shifting the value to an adjacent location in memory.

$$Y_i[n+1] = Y_{i+1}[n] \text{ for } i = 0 \ldots N_d - 2 \tag{2.6}$$

The first location, $Y_{N_d-1}$, is updated based on whether a photon is detected or not.

$$Y_{N_d-1}[n+1] = \begin{cases} 1 & \text{if one or more photons arrived in iteration } n \\ 0 & \text{else} \end{cases} \tag{2.7}$$

The result is that the if system has been running for at least $N_d$ clock cycles (one

delay time), we have

$$
Y_0[n] =
\begin{cases}
1 & \text{if one or more photons arrived in iteration } n - N_d \\
0 & \text{otherwise.}
\end{cases}
\tag{2.8}
$$

The time-delayed photon data is represented by $Y_0[n]$, and this signal is used to update the filter variables. I used an array of size $N_d = 32768$. This leads to a maximum time delay of $T_d = \Delta t = 1.734$ ms, where $\Delta t$ is the clock cycle which is used to update the shift register, $\Delta t = 8/(151.1515 \text{ MHz}) = 52.9270$ ns.

In this experiment, two different clock signals are used for photon detection. The clock which measures the photon arrival times has a frequency of 151.1515 MHz. The clock that is used for signal processing is 8 times slower, with a speed of 18.8939 MHz. I chose this clock speed because the dead time of the detector limits the number of photons that can be detected in one delay time. With $\Delta t = 52.9270$ ns, it is possible to have two photons arrive in adjacent time bins, and so the dead time of the detector does not impose a limitation on the dynamic range of the loop.

## 2.3.2  Filter equations

The filter state variables are represented by 32-bit integers, and fixed point arithmetic is used to calculate their time evolution. For readability, in this section, I will adopt the convention that the filter variables take values between 0 and 1, although in their digital representation, they take values between 0 and $2^{32} - 1$.

The filter state-space variables are updated according to the following equa-

tions.

$$X_1[n+1] = \left(1 - \frac{\Delta t}{T_1}\right) X_1[n] + gY_0[n]$$

$$X_2[n+1] = \left(1 - \frac{\Delta t}{T_2}\right) X_2[n] + gY_0[n]$$

(2.9)

where $g$ is a factor that sets the amplitude of the filter variables, and $T_1$ and $T_2$ are the time scales of the filter. The DAC outputs a positive voltage signal, so that the voltage applied to the modulator is $v[n] = V_0(X_1[n] - X_2[n])$. $V_0$ is a constant, measured in volts, that describes the characteristics of the DAC and the amplifier.

The scale of the variables $X_1$ and $X_2$ is arbitrary. To put these variables in a physical context, we note that the MZM is driven by the voltage $v[n] = V_0(X_1[n] - X_2[n])$. So, $X_1$ and $X_2$ should be compared to $V_\pi$. Introducing the dimensionless variables $x_i = gV_0 X_i \frac{\pi}{2V_\pi}$ and $\beta = gV_0\lambda_0 \frac{\pi}{2V_\pi}$, it is straightforward to verify that equation (2.9) is the Euler discretization of

$$\frac{d}{dt}\begin{pmatrix} x_1 \\ x_2 \end{pmatrix} = \begin{pmatrix} -\frac{1}{T_1} & 0 \\ 0 & -\frac{1}{T_2} \end{pmatrix}\begin{pmatrix} x_1 \\ x_2 \end{pmatrix} + \beta \begin{pmatrix} 1 \\ 1 \end{pmatrix} \frac{1}{\lambda_0}\sum_{i=1}^{\infty}\delta(t - t_i),$$

(2.10)

which is of the same form as equation (2.2). The rate of photon arrivals is given by

$$\lambda(t) = \lambda_0 I(t) = \lambda_0 \sin^2\left[x_1(t - T_d) - x_2(t - T_d) + \phi\right].$$

(2.11)

## 2.4 Dynamics

If we take the expectation value of the random term in equation (2.10), we obtain the deterministic model, given in equation (2.1). This model has rich dynamics. It is well-known that equations of the form (2.1) will go through a series

bifurcations into to chaos as $\beta$ increases [18]. Recall that in our photon-counting feedback loop,

$$\beta = gV_0\lambda_0\frac{\pi}{2V_\pi} \tag{2.12}$$

So, if the quantity $g\lambda_0$ is kept constant as $\lambda_0$ is varied, one will see dynamics whose noisiness varies with the values of $\lambda_0$, but the analogous deterministic equation as given by equation 2.1 will be unchanged. It is also well-known that the dimensionality of chaotic systems with time delay can be tuned over a wide range, and that the dimension and number of positive Lyapunov exponents tends to increase with the time delay [50].

In this section, we will describe the dependence of the dynamics on the incident photon rate, $\lambda_0$ with $\beta T_d$ held constant at 8.87. In our implementation, the time delay is $T_d$=1.734 ms. This is set by the memory of the FPGA and the filter clock frequency $\Delta t$. For the data presented here, the modulator bias is $\phi = \pi/4$, and the filter constants $T_1$=1.2 ms, and $T_2$=60 $\mu$s. We vary the photon rate over a factor of 256, from $\lambda_0 T_d = 12.5$ ($7.20 \times 10^3$ count/s) to $\lambda_0 T_d = 3,200$ ($1.845 \times 10^6$ counts/s). As the photon rate is increased, we see a transition from Poisson shot noise to deterministic chaos.

## 2.4.1 Time series, probability distributions, and autocorrelation functions

Figure 2.2 shows several time series recorded with this system with increasing photon rate. We plot $N_w(t)$, the number of photon arrivals in the interval $[t-w,t]$. In
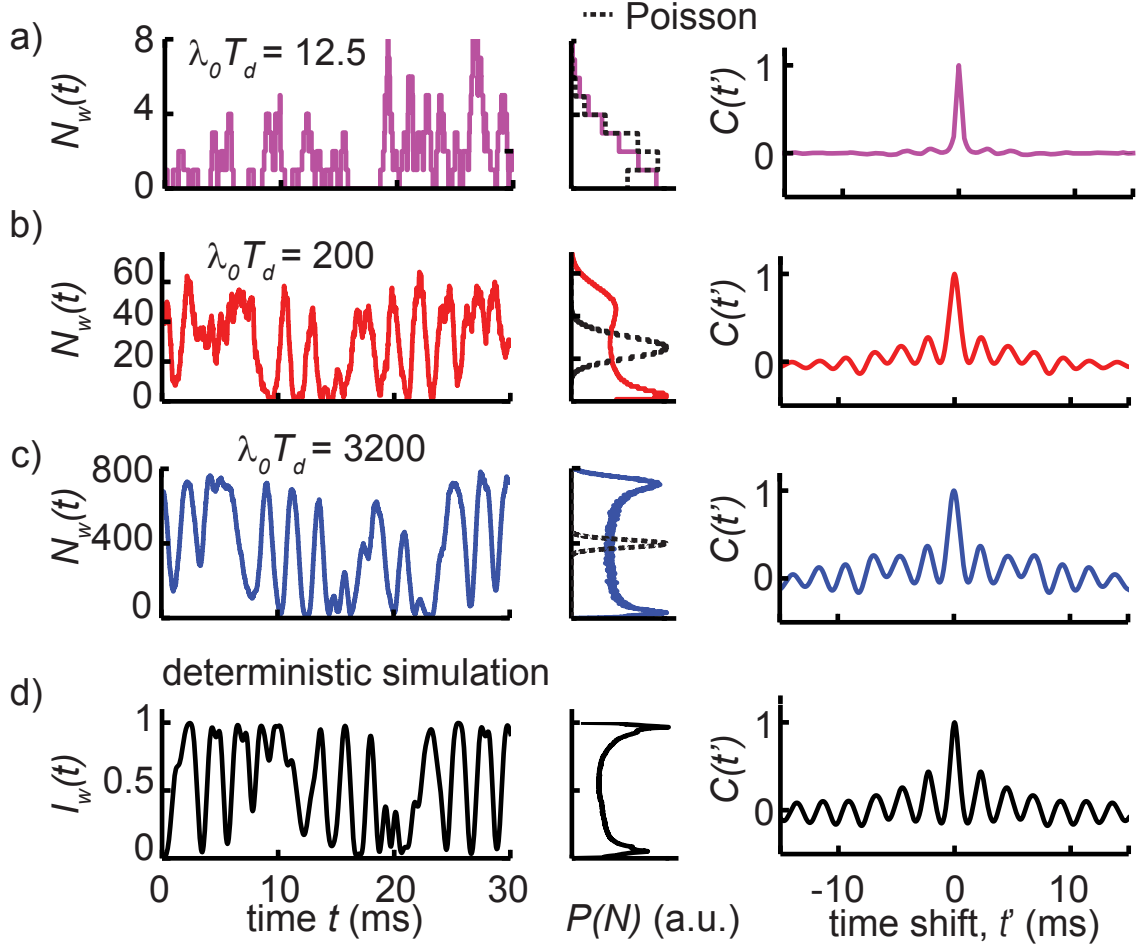
Figure 2.2: Time series, probability distributions, and autocorrelation functions. a) - c) show experimental data, and d) shows the result of a deterministic simulation of Equation 2.1. a) At a low photon rate of $\lambda_0 T_d$ = 12.5, the dynamics appear Poissonian. The time series has no visible structure, the autocorrelation function is sharply peaked at 0, and the distribution of photon counts in a window of $w = T_d/4$ is nearly Poisson. b) $\lambda_0 T_d = 200$, a slow modulation of the photon rate is evident. c) at $\lambda_0 T_d$ = 3,200, the photon rate varies smoothly, the photon count distribution is bimodal and much wider than a Poisson distribution with the same mean, and the autocorrelation function shows slow oscillations. The deterministic simulation d) shows the same features as the high photon rate data shown in c).

Figure 2.2, all of the plots were generated with $w = T_d/4$. When the incident photon rate is $\lambda_0 T_d = 12.5$, the photons appear to arrive at random, uncorrelated times as in a stationary Poisson process. Increasing the incident photon rate to $\lambda_0 T_d = 200$, a smooth modulation of the photon rate starts to become apparent. At $\lambda_0 T_d = 3,200$, $N_w(t)$ has a smooth character, and qualitatively resembles a low-dimensional chaotic signal. We also plot the results of a deterministic simulation using equation (2.1). This time series was smoothed with a moving average over a time window of width $w$ to be directly comparable with $N_w(t)$. We plot the autocorrelation function, $C(t') = \langle (N_w(t) - \bar{N}_w)(N_w(t - t') - \bar{N}_w) \rangle$, normalized so that the value of the autocorrelation function is unity at $t' = 0$. As the photon rate increases from $\lambda_0 T_d = 12.5$, the autocorrelation function changes from a $\delta$-like peak, characteristic of a Poisson process, to an oscillatory function which shows correlations at long timescales (tens of milliseconds). The autocorrelation function of the deterministic simulation time series is in close agreement with the autocorrelation function of the photon arrivals with $\lambda_0 T_d = 3,200$. Histograms of $N_w(t)$ also show a transition from a nearly Poisson distribution to a bimodal distribution. The peaks of the bimodal distribution are due to turning points imposed by the maximum and minimum values of the transmitted light through the modulator. This bimodal distribution is seen in the deterministic simulation.

### 2.4.2 Attractor visualizations

To visualize the development of chaos with increasing photon rate, we show Poincaré surfaces of section in Figure 2.3. We perform a time-delay embedding of the experimental time series $N_w(t)$, using a time delay of $\Delta = T_d/4$, by constructing a list of points in two dimensional space of the form $[N_w(t), N_w(t - \Delta)]$. Because the attractor has a dimension higher than 2, we reduce the dimensionality of the attractor by plotting the points only when the state variables pass through a codimension 1 Poincaré surface defined by $x_1 - x_2 = \pi$. The embeddings show a similar trend to the plots in Figure 2.2. We see a development of complex chaotic dynamics from discrete photon noise as the photon rate increases. The deterministic simulation is plotted for comparison, and, as in Figure 2.2, a moving average of width $w$ is employed so that the smoothed intensity time series, $I_w(t)$, is directly analogous to $N_w(t)$. The deterministic signal in Figure 2.3d can be regarded as the infinite photon rate limit of the photon counting system.

### 2.4.3 Variance

Figure 2.4 shows the dependence of the variance of $N_w$ on the window $w$ and offers another indication of the transition from shot noise to deterministic chaos. The time integral of an uncorrelated random signal executes a random walk in which the variance grows linearly with the integration time. For this reason, we plot $\text{Var}(N_w)/w$ in Figure 2.4. We see distinct asymptotic growth rates of the variance with small and large $w$. When $w$ is small, the variance reflects the Poissonian nature

23
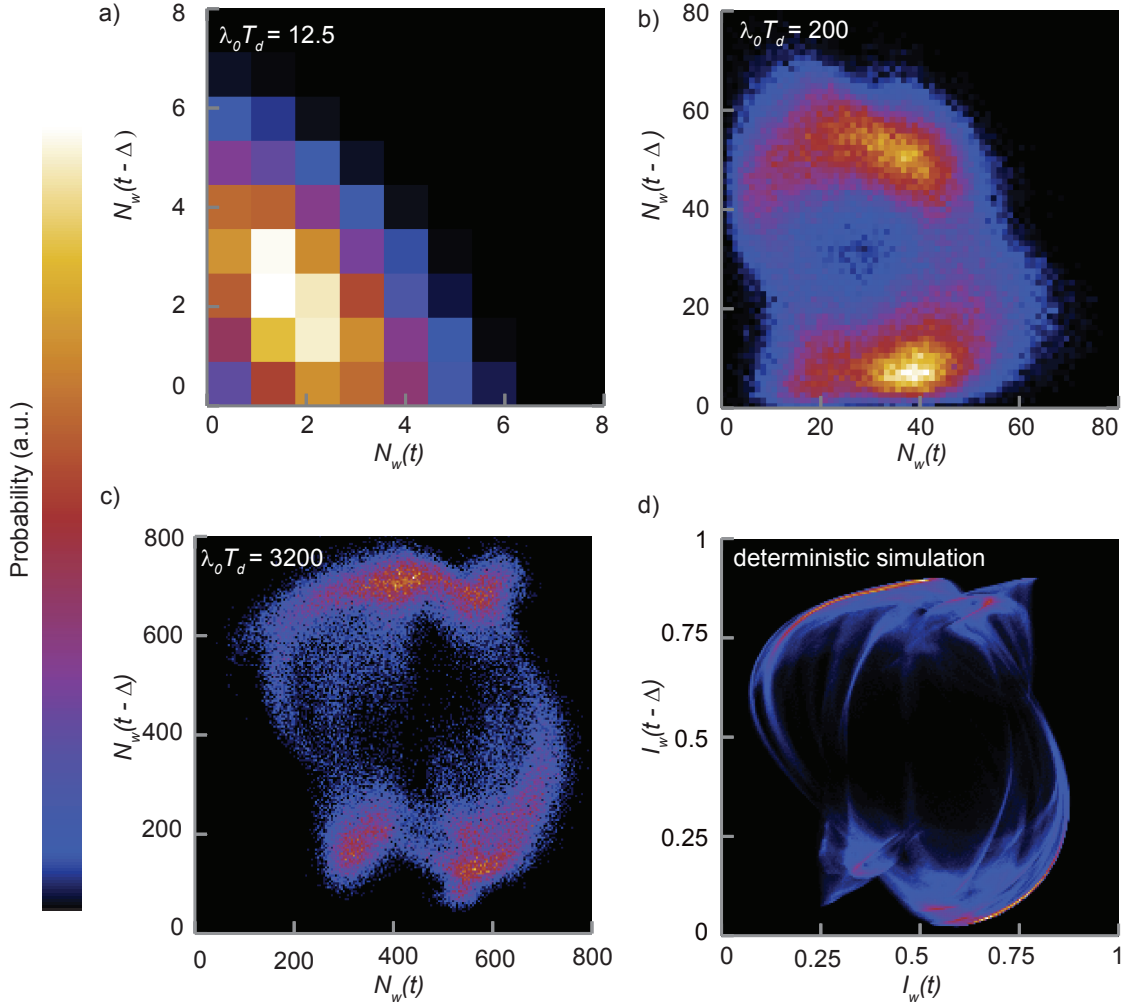
Figure 2.3: Poincaré sections. We visualize the emergence of a chaotic attractor from Poisson noise with increasing photon rate by embedding photon count time series in two dimensions with a time delay of $\Delta = T_d/4$, and reducing the dimensionality of the dynamics by plotting points only when the state of the system in phase space passes though a codimension-1 surface defined by $x_1 - x_2 = \pi$. a) - c) show experimental data, and d) shows the result of a deterministic simulation. These histograms are constructed with a bin width of 1 photon in in a) and b), 4 photons in c), and 0.005 in d)

of the photon arrivals, and the growth rate of the variance has roughly constant value of $\mathrm{Var}(N_w)/w = \lambda_0 \bar{I}$. In the limit where the counting window is much longer than the time scale of the variations in intensity, $N_w(t)$ can be regarded as the sum of the photon counts in many independent identically distributed intervals, and the central limit theorem implies that the variance will grow in proportion to $w$. As we increase the photon rate from $\lambda_0 T_d = 12.5$ to $\lambda_0 T_d = 3,200$, we see an increasing offset between the two asymptotic rates of growth of the variance. The variance can be related to the photon rate, counting window, and the unnormalized autocorrelation function, $c_I(t') = \left\langle (I(t) - \bar{I})(I(t - t') - \bar{I}) \right\rangle$ [40].

$$
\mathrm{Var}(N_w) = w \left[ \lambda_0 \bar{I} + \lambda_0^2 \underbrace{\int_{-w}^{w} dt' \left( 1 - \frac{|t'|}{w} \right) c_I(t')}_{\Theta(w)} \right] \tag{2.13}
$$

The second term in Equation (2.13) accounts for the difference between the observed variance and the variance of a Poisson process with the same rate. The quantity $\Theta(w)$ has units of time, and measures the correlations in $I(t)$ introduced by the feedback. This quantity increases from 0 to an asymptotic value $\Theta_\infty$ as $w$ increases, accounting for the shape of the curves shown in Figure 4. $c_I(t')$ and $\Theta(w)$ can be calculated from time series generated by deterministic simulations. In this case, we find $\Theta_\infty = 150 \ \mu$s. The value of $\Theta_\infty$ is related to the size of the intensity fluctuations, and the rate at which $\Theta(w)$ approaches this asymptotic value is determined by the timescales of the correlations of $I(t)$.
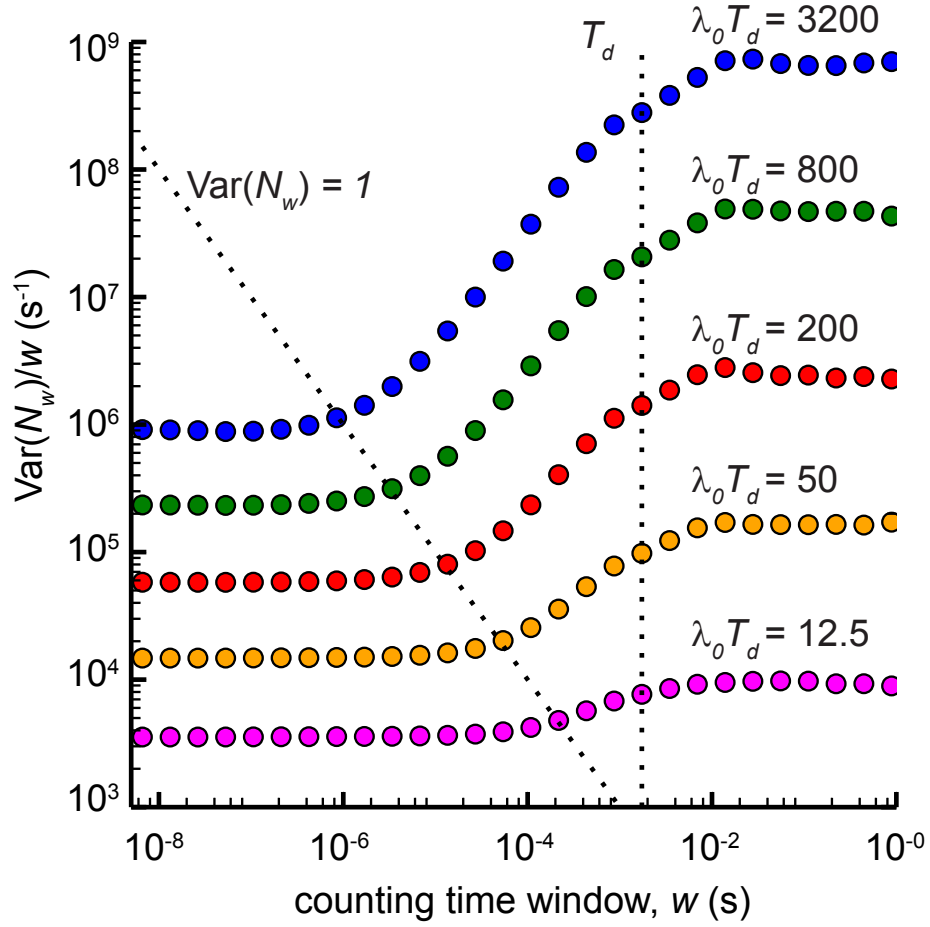
Figure 2.4: Experimental dependence of growth rate of variance on counting time window, $w$. To indicate the timescale of the deterministic dynamics we indicate $T_d$. We also show a line indicating $\mathrm{Var}(N_w) = 1$, which roughly separates timescales over which less than one photon arrives in the counting window from timescales over which many photons arrive. Distinct asymptotic values of $\mathrm{Var}(N_w)/w$ are seen in the limits of small and large $w$. The offset between these two values reflects deterministic correlations in the photon arrival rate and grows with increasing photon rate.

## Chapter 3: Entropy generation in a photon-driven feedback loop

*This chapter is based on work from the following publication*

*Aaron Morgan Hagerstrom, Thomas Edward Murphy, and Rajarshi Roy. Harvesting entropy and quantifying the transition from noise to chaos in a photon-counting feedback loop. Proceedings of the National Academy of Sciences 112(30):9258–9263, 2015.*

## 3.1 Overview

The main goal of this Chapter is to describe entropy quantification in the context of the experiment described in Chapter 2. The entropy content of datasets shown in Chapter 2 will be analyzed, and I will comment on how the entropy estimates indicate the transition from photon counting noise to chaos described in Chapter 2. Finally, I will discuss the relevance of these results in the general context of random number generation.

The Chapter is organized as follows. Section 3.2 describes why physical random number generators are important, and discusses how most researchers in this field approach the calculation of entropy rates. I will briefly discuss some of the recommendations in the draft NIST SP800-90B guidelines for physical entropy sources [52]. In Section 3.3, I give some basic definitions of information-theoretic

quantities and describe how entropy rates are calculated. In Section 3.4, I describe how to calculate the entropy rate of a constant-rate Poisson process. The results in this section, while very basic, should be familiar to anyone who wants to harvest entropy from photon arrival times. They also are a point of comparison for our experimental data. Section 3.5 shows entropy calculations applied to the deterministic model of the photon counting feedback loop. Section 3.6 describes the application of the entropy calculations to experimental data from the photon-counting feedback loop. Section 3.7 discusses the relevance of these experimental results to physical random number generation in general.

## 3.2   Background

Random numbers are very important for Monte-Carlo techniques [53] and for information security applications. In many cases, random numbers are generated using deterministic algorithms, and are called "pseudorandom numbers". The appeal of using pseudorandom numbers is clear – computers are fast, and pseudorandom number generators allow for random number generation without the need for dedicated hardware. Especially for cryptographic applications, there is a real concern that pseudorandom numbers are not good enough. A deterministic algorithm will have reproducible results, and there is a possibility that an attacker could exploit this predictability. For example, in 2012, security researchers showed that an alarming fraction – two out of every thousand – of RSA public keys collected from the Internet offer no security because they were not generated using properly-seeded ran-

dom numbers [54]. In order to avoid security weaknesses of this type, the random number generator used in Linux systems is continually re-seeded using entropy [55] harvested from events like key-strokes and mouse movements. Intel has also started to manufacture hardware-based random number generators [56]. There is still a great deal of interest in devices that harvest entropy from physical sources, both because these devices can have high speeds, and more importantly, because the unpredictability of the random numbers can be claimed to be due to a fundamentally unpredictable physical process.

A variety of mechanisms have been proposed for physical random number generation using quantum mechanics [13,14]. Several commercial devices, which are marketed as "quantum random number generators" are currently being sold [15]. Some commercial devices use weak light sources and photon-counting detectors. One scheme employs a beam splitter and two detectors, so that whenever a photon arrives, one detector or the other detects the photon, yielding either a 0 or a 1. Another scheme involves harvesting entropy from the random time intervals between photon arrivals [16].

There are also a variety of techniques for random number generation based on chaos [11, 12, 57–66]. Many of these techniques employ optical systems with a high bandwidth and fast detectors. A major advantage of these chaos-based techniques is that they are fast. Whereas the bit rates of photon-counting random number generators are measured in megabits per second, the bit rates of chaos-based random number generators are measured in gigabits or terrabits per second [12]. Some proponents of photon-counting based random number generation claim that chaos

is not "fundamentally" random, but the detection of individual photons is [15]. It is often pointed out that, on a fundamental level, the chaotic dynamics of a laser system are continually perturbed by microscopic quantum fluctuations [65, 66]. It's worth noting that not all chaos-based random number generation techniques are optical, some rely on digital electronics [58]. It's also worth noting that chaos isn't the only optical method of generating random bits. Like chaos, amplified spontaneous emission can yield bit rates in the gigabit per second range [57, 67, 68].

The bit rate is a crucial figure of merit for random number generators. Usually, the designer of a random number generator wants to show that their device can be used for practical purposes, like Monte Carlo techniques or cryptography. For these applications, it is important that they verify that their numbers are free of bias and correlation. "Bias" refers to streams of bits where "1" or "0" account for more than half of the bits. "Correlation" refers to a tendency to have longer sequences of either "0" or "1", or more generally, a situation where the value of one bit can be partially predicted based on the values of previous bits. Ideally, each bit is completely statistically independent of the other bits, and is equally likely to be either "0" or "1". In such a case, a bit stream is said to be "full entropy" or "one bit per symbol". The NIST [21] and Diehard [22] tests are commonly used to verify that a stream of bits is indeed full entropy.

Physical processes are usually not completely free of bias and correlation. In a system based on single-photon detection, there may be bias because the beamsplitter is not exactly 50/50, or because there are some small manufacturing differences between the two detectors. There can also be correlations due to non-ideal behavior

of the detectors [69]. The probability distribution of a measured quantity in a chaotic system is usually not completely uniform, so chaotic systems usually have some bias. They also tend to show deterministic correlations if sampled quickly [12, 65, 66]. So, in practice, almost all physical random number generators employ some "conditioning" to reduce bias and correlation. These approaches vary in complexity. Two of the more simple techniques are taking the logical XOR of independent bit streams [11] and numerical differentiation [60]. Taking the idea of conditioning to its logical extreme, it is of course possible to seed a pseudorandom number generator with a signal measured from a physical entropy source. Indeed, some authors employ hash functions, which will output completely full-entropy noise, regardless of how predictable their input is [70].

### 3.2.1   NIST Recommendations for Entropy Sources

The NIST [21] and Diehard [22] tests were not designed as a way to assess physical random number generators. They were designed to certify that a bit stream is free of bias and correlation. When conditioning is used, it can be difficult to claim that the entropy rate certified by these tests is due to the physical system, rather than the conditioning. Given that bias and correlation can be corrected using hash functions, NIST has drafted the new SP800-90B guidelines [52] for physical random number generators. These standards do not require that a physical noise source be free of bias and correlations. Instead, they require (among other things) that:

1. Although the noise source is not required to produce unbiased and independent outputs, it **shall** exhibit probabilistic behavior; i.e., the output **shall not** be definable by any known algorithmic rule.

31

2. The developer **shall** document the operation of the noise source; this documentation **shall** include a description of how the noise source works and rationale about why the noise provides acceptable entropy output, and **should** reference relevant, existing research and literature.

Furthermore, the new standards allow for conditioning, and several specific hash functions are approved types of conditioning. In order to justify the use of a hash function for conditioning, one must be able to assess the entropy rate of the noise source:

1. When an input string with $m$ bits of assessed entropy is provided to an approved conditioning function with an n-bit output, the resulting assessed entropy is uniformly distributed across the entire $n$-bit output. Note that if $m \geq n$, full entropy output is not necessarily provided; see item 2.

2. When an input string with $2n$ bits (or more) of assessed entropy is provided to an approved conditioning function with an n-bit output, the resulting $n$-bit output is considered to have full entropy.

So, to summarize, one must assess how much entropy one is entitled to take from a noise source, and it is not as important whether the noise source has bias and correlations. This chapter is describes one possible route towards justifying such an assessment.

### 3.2.2 Entropy Generation in Physical Systems

Entropy is usually computed from discrete quantities. Physical variables like voltage, current, and optical intensity are often either continuous, or their discretization is so fine (individual photons and electrons) that it makes sense to think of them as continuous. Bits, by contrast, are discrete – either 0 or 1. Measurements of physical systems usually involve digitizing or discretizing a quantity to some finite
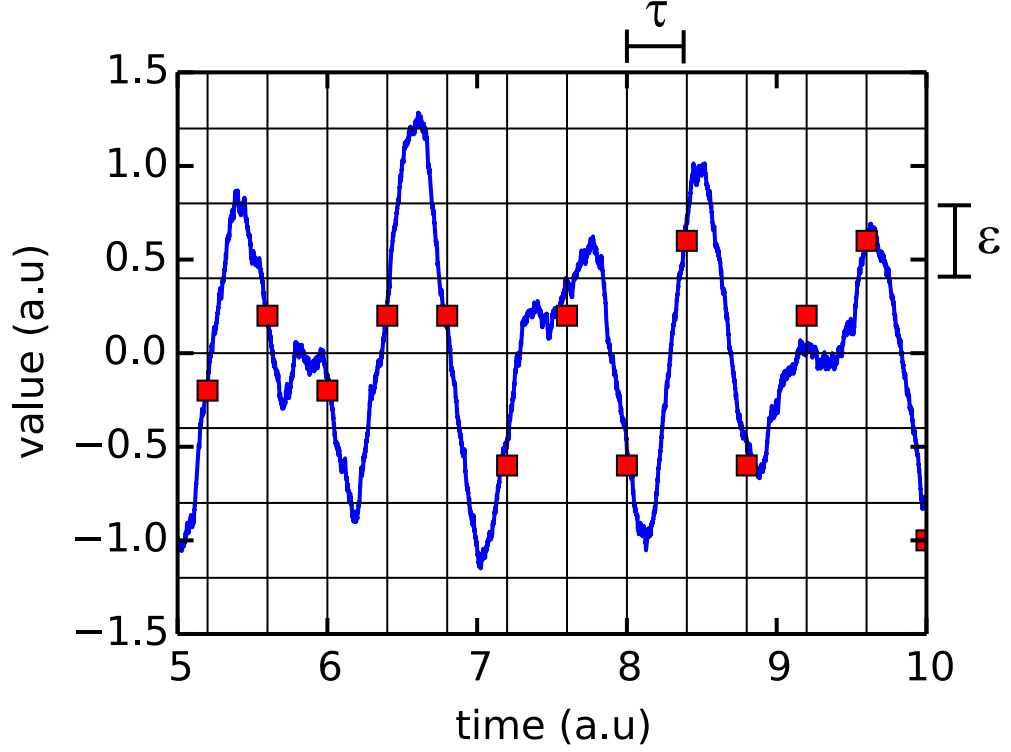
Figure 3.1: Illustration of an time trace from a physical system sampled to resolution in time $\tau$, and resolution in value $\varepsilon$. The vertical grid lines represent sampling times, and the horizontal grid lines represent bin edges.

resolution, $\varepsilon$. Measurements of a physical system are usually discrete in time as well. For example, an oscilloscope records samples at discrete times, with a time interval between measurements of $\tau$. These three parameters $\varepsilon$ and $\tau$ are often unavoidable. In some cases, on might need to consider a third variable, $w$. In the case of the photon-counting feedback loop described in Chapter 2, $w$ is the time interval over which we count photons. Rate fluctuations much faster than $1/w$ will not be resolved.

In the context of statistical mechanics, information entropy is a very important concept [71–75]. There is a rich literature on the dependence of the entropy rate, $h$, of signals harvested from physical systems on the variables $\varepsilon$ and $\tau$ [10, 76–80]. In these contexts, the entropy rate is often called the $(\varepsilon, \tau)$ entropy, and is denoted $h(\varepsilon, \tau)$. It has been shown in Brownian motion and Johnson noise in RC circuits that statistical measurements of this entropy can be related to heat dissipation [81, 82]. There have also been experimental investigations of entropy rates in convection experiments [77, 80]. The $(\varepsilon, \tau)$ entropy will have qualitatively different dependence on $\varepsilon$ and $\tau$ depending on the physical origin of the unpredictability [10, 76, 80].

## 3.3    Entropy and Entropy Rate

This section discusses a few basic concepts from information theory that will be employed in the rest of the chapter, with an emphasis on calculating the entropy rate of a dynamical system. Most of these concepts are described in standard textbooks, like [83]. For a discussion of entropy in the context of dynamics, see [10, 76, 80, 84], especially [10, 80].

This section requires some notation. This is all standard notation, but for clarity I'm making a table of definitions (3.1).

The Shannon entropy of a random variable $X$ is defined as

$$H(X) = -\sum_{x \in \mathcal{X}} p(x) \log_2 p(x). \tag{3.1}$$

Table 3.1: some notation

| Symbol | Meaning |
|---|---|
| $X$ | a generic random variable |
| $x$ | a specific value that $X$ might take, like 4 |
| $\mathcal{X}$ | the set of possible values $x$ might take |
| $p(x)$ | the probability that $X$ takes the specific value $x$ |
| $X_i$ | a random variable, the value of $X$ at time $i$ |
| $x_i$ | the value of $X_i$ in a particular realization |
| $x(t)$ | the value of $X$ at a specific time in a specific realization of the physical process |
| $p(x_i, x_j)$ | the joint probability that $X_i$ takes the value $x_i$ and $X_j$ takes the value $x_j$ |
| $p(x_i|x_j)$ | the conditional probability that $X_i$ takes the value $x_i$ given that $X_j$ takes the value $x_j$ |

The entropy of this joint probability distribution can be calculated in the same way:

$$H(X_1, X_2, \ldots, X_d) = -\sum_{x_1 \in \mathcal{X}} \sum_{x_2 \in \mathcal{X}} \cdots \sum_{x_d \in \mathcal{X}} p(x_1, x_2, \ldots, x_d) \log_2 p(x_1, x_2, \ldots, x_d).$$

(3.2)

Another important concept is conditional entropy. This is used to quantify to what extent one variable, $X_1$, can be predicted by sampling a different variable, $X_2$. Conditional entropy is defined as the expected value of the entropy of $X_1$ given that $X_2$ has been sampled and is known to have the value $x_2$:

$$H(X_1|X_2) = -\sum_{x_2 \in \mathcal{X}} p(x_2) H(X_1|X_2 = x_2)$$

$$= -\sum_{x_1 \in \mathcal{X}} \sum_{x_2 \in \mathcal{X}} p(x_1, x_2) \log_2 p(x_1|x_2)$$

(3.3)

If $X_1$ can be completely predicted by sampling $X_2$, then $H(X_1|X_2) = 0$. On the other hand, if $X_1$ and $X_2$ are independent, $H(X_1|X_2) = H(X_1)$. The conditional

entropy can be related to the entropy of a joint probability.

$$
\begin{aligned}
H(X_1|X_2) &= -\sum_{x_1 \in \mathcal{X}} \sum_{x_2 \in \mathcal{X}} p(x_1, x_2) \log_2 p(x_1|x_2) \\
&= -\sum_{x_1 \in \mathcal{X}} \sum_{x_2 \in \mathcal{X}} p(x_1, x_2) \log_2 \frac{p(x_1, x_2)}{p(x_2)} \quad\quad (3.4) \\
&= H(X_1, X_2) - H(X_2)
\end{aligned}
$$

This is called the "chain rule".

The entropy rate of a stochastic process can be measured either in bits per sample, or bits per second. For consistency with the rest of the chapter, I will write the formulas for the entropy rate in bits per second, by adding a factor of $1/\tau$, where $\tau$ is the time interval between samples. There are two definitions of the entropy rate $h$. These definitions will yield the same result for stationary processes [83], but, in practice, one is more easy to calculate.

The first definition is

$$
h_1(X) = \lim_{d \to \infty} \frac{1}{\tau d} H(X_1, X_2, \ldots, X_d). \quad\quad (3.5)
$$

In Equation 3.5, one considers patterns of increasing length $d$, and measures how the entropy of the set of patterns of length $d$ changes with $d$. If $d$ is large enough, one finds that the entropy of the set of patterns (pattern entropy) grows proportionally to $d$. This linear growth is shown in Figure 3.2.

The second definition of entropy rate is based on the extent to which the current sample, $x_i$, can be predicted based on the history of previous samples.

$$
h_2(X) = \lim_{d \to \infty} \frac{1}{\tau} H(X_d|X_{d_1}, \ldots, X_1). \quad\quad (3.6)
$$
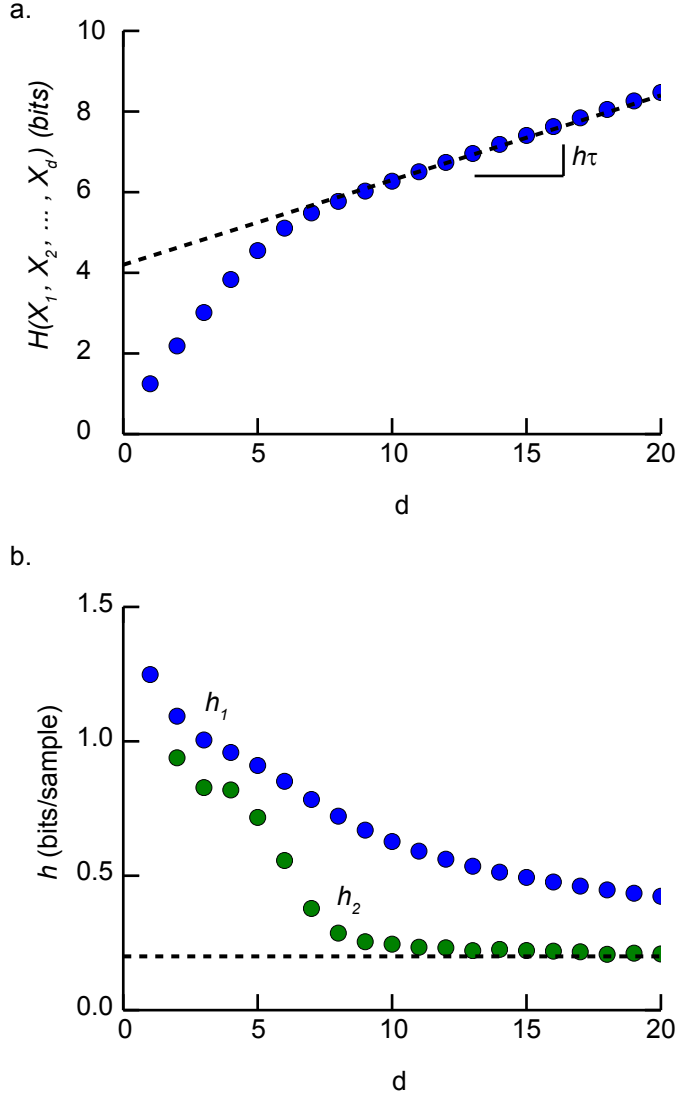
Figure 3.2: Pattern entropy and entropy rate. a) An example of the growth of the pattern entropy, $H_d = H(X_1, X_2, \ldots, X_d)$, as a function of $d$. The asymptotic linear growth is indicated by a dashed line. Although this figure is intended as an illustration of concepts of pattern entropy and entropy rate, experimental data are shown here. The pattern entropy rate was calculated by applying the Cohen-Procaccia method (Equation 3.9) to the time series $N_w(t)$, from the photon-counting feedback loop, with $\lambda_0 T_d = 3200$, $\tau = w = T_d/4$, and $\varepsilon = 400$ photons. Note that there are two linear scaling regions of $H_d$. Small embedding dimensions, or pattern lengths, are insufficient to predict the dynamics, leading to a fast increase of $H_d$ with $d$. b) Approximations of the entropy rate based on Equations 3.5 and 3.8. Both $h_1$ and $h_2$ approach the same limit, but $h_2$ approaches much more quickly with increasing embedding dimension.

As mentioned previously $h_1 = h_2$ for stationary systems. Equation (3.6) be re-written in another form that is more convenient experimentally. By the same logic as Equation (3.4), we can write

$$H(X_d|X_{d_1}, \ldots, X_1) = H(X_d, X_{d-1}, \ldots, X_1) - H(X_{d-1}, X_{d-2}, \ldots, X_1), \qquad (3.7)$$

which leads to

$$h_2(X) = \lim_{d \to \infty} \frac{1}{\tau} \left[ H(X_d, X_{d-1}, \ldots, X_1) - H(X_{d-1}, X_{d-2}, \ldots, X_1) \right]. \qquad (3.8)$$

Like Equation 3.5, this formula for the entropy rate indicates a linear growth of the pattern entropy with $d$. Whereas Equation 3.5 calculates the average entropy per symbol in a large pattern, Equation 3.8 calculates the slope of the growth of the pattern entropy with $d$. It can be argued that $h_2$ will give a better approximation of the entropy rate for finite $d$ [85], and Figure 3.2 suggests that this is the case.

### 3.3.1 Entropy Calculations

The first step to computing the $(\varepsilon, \tau)$ entropy rate of an experimental signal is to generate a list of points in $d$-dimensional space using time delay embedding with a delay of $\tau$. These vectors can be regarded as samples of a $d$-dimensional probability distribution over phase space. The entropy of this probability distribution, $H_d = H(X_1, X_2, \ldots, X_d)$. In principle $H_d$ can be calculated by building a histogram with boxes of width $\varepsilon$ and applying Shannon's formula, Equation 3.1 [83]. In practice, direct application of this approach requires a very large amount of data when the embedding dimension is large. Cohen and Procaccia proposed a more efficient

algorithm to estimate the pattern entropy [85] in the context of estimating metric entropy from experimental data. First, one randomly selects a small number $M$ of reference points from the time series. $M$ is usually small compared to the length of the time series. In our case we observed only small differences between $M = 5000$ and $M = 20000$. For each reference point $i$, one computes $n_i(\varepsilon)$, the fraction of the points in the dataset within a box of width $\varepsilon$ centered on the reference point. The only difference between a direct calculation of the Shannon entropy, and the Cohen-Procaccia procedure is that in a direct calculation, a rectangular array of bins is used, rather than a set of bins centered on random points chosen from the data set. In searching for neighbors for the $i$th reference point, we exclude points within a time window of $\tau$ of that point, as suggested by Theiler [86]. The pattern entropy is then estimated by

$$H_d(\varepsilon) = -\frac{1}{M} \sum_{i=1}^{M} \log_2 n_i(\varepsilon). \tag{3.9}$$

It is a general feature of unpredictable signals that $H_d$ grows linearly with $d$ in the limit that $d$ is large, and the entropy rate is the slope of this linear increase, as indicated in Equation 3.8. Cohen and Procaccia argued that Equation 3.8 approaches the correct value of the entropy rate at a lower dimension than Equation 3.5. Figure 3.2 shows an anecdotal example where this is the case.

We will see that the calculation of $H_d$ from Equation 3.9 requires a large amount of data. Some authors have suggested using the correlation entropy, $H_d^{(2)}$, in place of $H_d$. [10, 76, 77].

$$H_d^{(2)}(\varepsilon) = -\log_2 \frac{1}{M} \left( \sum_{i=1}^{M} n_i(\varepsilon) \right) \tag{3.10}$$

## 3.4 Entropy rate of a constant rate Poisson process

In this section, I give a few basic results about the entropy rate of a Poisson process. This is relevant to the discussion of a photon-counting optoelectronic feedback loop because the arrival of photons generated by a laser at a photon-counting detector is described by a Poisson process. The results given in this section are far from new, but will provide context for later results, and it can be helpful to show how the methods described here can be applied in a simple case.

A Poisson process describes events (like photon arrivals) that occur at random times. The probability per unit time for an event to occur is constant, and the probability that an event occurs at time $t$ is independent of whether or not an event occurs at time $t'$.

Because the events in different points in time are statistically independent, it's very easy to evaluate the entropy rate. I will assume that we have divided time into small bins of width $\tau$, and that it is possible to sample system much faster than the event rate, so $\tau\lambda_0 \ll 1$. I will consider the case where $\tau\lambda_0 \gg 1$ later in this section. The probability that one or more events occurs in a time bin is $1 - e^{\lambda_0\tau} \approx \lambda_0\tau$. I will now consider a random variable $Y_i$, which takes a value 1 if one or more photons arrive in bin $i$, and 0 if no photons arrive. The probability mass function of $Y_i$ is

$$p(Y_i = 0) = 1 - p_0$$

$$p(Y_i = 1) = p_0$$

(3.11)

The entropy rate can be trivially evaluated from either Equation 3.5 or Equa-

tion [3.6](#).

$$h = \frac{-1}{\tau} \left[ (1 - p_0) \log_2 (1 - p_0) + p_0 \log_2 (p_0) \right] \tag{3.12}$$

In photon counting experiments, it is possible to time photon arrivals to a high degree of precision. We used a clock with a speed of $1/\tau$=151.1515 MHz, and state-of-the-art detectors can tag photon arrivals to tens of ps. On the other hand, the maximum count rates resolvable by detectors are on the order of $10^7$ counts/second. So, we are interested in the limit that $\tau \to 0$. Recalling that $p_0 \approx \lambda_0 \tau$, and expanding to lowest order, we have

$$h = \lambda_0 \left( \frac{\lambda_0}{\ln 2} - \log_2 \lambda_0 \tau \right) \tag{3.13}$$

There are a few comments to make here. The entropy rate grows without bound as $\tau \to 0$, but the growth is logarithmic. This presents a limitation to the scalability of random number generation using photon-counting detectors. To put in real numbers, the experimental system described in Chapter [2](#) has a temporal resolution of $\tau$=6.62 ns. If $\lambda_0 = 2 \times 10^6$ counts/s, the entropy rate is $h = 15.4$ Mbits/s. If the timing resolution could be increased to $\tau$=66.2 ps, which is on the order of the state of the art, then we would have $h = 28.6$ Mbits/s. Improving the timing resolution of a detector by a factor of 100 will not increase the bit rate by a factor of 100 but instead will yield a relatively small increase of about 6.6 bits per photon. In contrast, when either a chaotic system or amplified spontaneous emission is used to generate random numbers, the entropy rate can scale more favorably with $\tau$. As discussed in Section [3.5](#), the entropy rate of a chaotic system is determined by

its positive Lyapunov exponents, which can be on the order of hundreds of gigabits per second [12, 57]. These fast dynamical timescales allow one to take advantage of fast digitizers to harvest entropy at high rates.

Another point to make here is that bias and entropy rate are distinct concepts. As $\tau \to 0$, the distribution of $Y_i$ is increasingly biased in favor of 0, and yet the entropy rate grows.

### 3.4.1  Entropy rate from inter-arrival intervals

Another way to harvest entropy from a Poisson process would be to use the inter-arrival intervals. Time will still be discretized in bins of width $\tau$, but now the random variable we will consider is $T_i$, the time interval between the $(i - 1)$th photon arrival and the $i$th photon arrival.Since time is divided into bins of width $\tau$, $T_i$ takes on discrete values: $\tau$, $2\tau$, and so on.

The variables $T_i$ are independent and identically distributed, and this distribution is given by a geometric distribution. This is a direct consequence of the statistical independence of different time bins, and the assumption that the rate is constant.

$$p(t_i = k\tau) = p_0(1 - p_0)^k \text{ for } k\text{=1,2,...,}\infty \tag{3.14}$$

From 3.5, we have

$$h = \frac{-1}{\bar{t}} \sum_{k=1}^{\infty} p_0(1 - p_0) \log_2 p_0(1 - p_0) \tag{3.15}$$

Where $\bar{t} = \tau/p_0$ is the average of $t_i$. This sum can be evaluated in closed form, and

42

we have

$$h = \frac{-1}{\tau} \left[ (1 - p_0) \log_2 (1 - p_0) + p_0 \log_2 (p_0) \right], \tag{3.16}$$

which is identical to Equation 3.12. So, measuring inter-arrival times will yield exactly the same entropy rate as measuring $Y_i$.

## 3.4.2 Can intensity modulation increase entropy rates?

So far, I have only discussed constant-rate Poisson processes. In the previous chapter, I described a system in which feedback is used to modulate the intensity of a weak light source, so that variations in the photon arrival rate were seen at the detector. It is natural to ask if these rate fluctuations increase the entropy rate of the signal compared to a constant-rate process. It turns out that the Poisson process has the highest possible entropy of any process consisting of a sequence of discrete events with a given average inter-event interval.

This can be shown using Lagrange multipliers. We will assume that we are harvesting entropy from the intervals between events, $T_i$, as in the last section. The average inter-event interval will be denoted $\bar{t}$. It may be the case that when rate fluctuations are present, the inter-event intervals are no longer independent or identically distributed. I will assume that the process which determines the inter-arrival intervals is stationary, but individual photon arrivals are not necessarily independent. So $p(t_i = k) = p(t_j = k)$, but $p(t_i | t_{i-1}, t_{i-2}, \ldots, t_{i-d}) \neq p(t_i | t_{j-1}, t_{j-2}, \ldots, t_{j-d})$.

It is well-known [83] that for any random variables $X_1, X_2, \ldots X_d$,

$$H(X_1, X_2, \ldots X_d) \leq H(X_1) + H(X_2) + \cdots + H(X_d) \tag{3.17}$$

From Equation 3.5, we then have

$$h \leq \frac{-1}{\bar{t}} \sum_{k=1}^{\infty} p(k) \log_2 p(k) \tag{3.18}$$

I will now maximize the right-hand-side of 3.18 subject to the constraints that the distribution has a well-defined mean, is defined for integers $k$ greater than 1, and is normalized. Introducing the Lagrange multipliers $\alpha$ and $\beta$, the variational equations are:

$$\frac{\partial}{\partial p(k)} \left[ \alpha \left( \bar{t} - \tau \sum_{k=1}^{\infty} k p(k) \right) + \beta \left( 1 - \sum_{k=1}^{\infty} p(k) \right) + \sum_{k=1}^{\infty} p(k) \log_2 p(k) \right] = 0 \tag{3.19}$$

This can be solved for $p_k$.

$$p(k) = 2^{-\alpha \tau k - 1 - \beta} \tag{3.20}$$

This has the form of a geometric distribution. The values of $\alpha$ and $\beta$ are set by the constraint equations. The result will be Equation 3.14 with $p_0 = 1/\bar{t}$. The conclusion is that, if entropy is harvested from the time intervals between a series of events with a well-defined average inter-event interval, a Poisson process will yield the highest possible entropy rate.

### 3.4.3 Counting windows and $\varepsilon$

In Chapter 2, I used the variable $N_w(t)$, the number of photon counts in the interval $[t-w, t]$, to analyze the behavior of the photon-counting feedback loop. One advantage of this variable is that it shows the chaotic character of the dynamics, at least as far as having similar time traces and autocorrelation functions. Another example is that it can be directly compared to a Poisson process with a constant

44

rate. In a Poisson process, the distribution number of events, $N$, to arrive in an interval $[t - w, t]$ is

$$p(N) = \frac{\bar{N}^N}{N!} e^{-\bar{N}}. \tag{3.21}$$

In a constant-rate process, the expected number of events is $\bar{N} = w\lambda_0$

In a constant-rate process, successive samples are uncorrelated if $\tau \geq w$. The entropy rate is then straightforward to calculate from Equations 3.1 and 3.5. There is not a closed-form solution, but in a certain limit, it is possible to make a crude approximation that works fairly well. In the limit that $\lambda_0 w \gg 0$, the Poisson distribution (Equation 3.21) approaches the Gaussian distribution with a mean and a variance of $\lambda_0 w$. If $\sqrt{\lambda_0 w} \gg \varepsilon$, the sum in Equation 3.1 can be approximated by an integral. In this case, we can approximate the entropy rate of a Poisson process with a counting window as

$$h = \frac{1}{\tau} \log_2 \left( \sqrt{\frac{2\pi e w \lambda_0}{\epsilon}} \right). \tag{3.22}$$

Note that this entropy's dependence on $\epsilon$ is $-\log_2 \epsilon$. The logarithmic dependence on $\epsilon$ is common in noisy systems [76, 80, 84]. Figure 3.3 shows the comparison of the entropy rate calculated from Equation 3.22 to the entropy rate calculated from experimental photon count data.

## 3.5   Entropy rate of chaotic systems

In chaotic systems, unpredictability is due to the sensitive dependence on initial conditions. Because small perturbations grow exponentially in time, chaotic
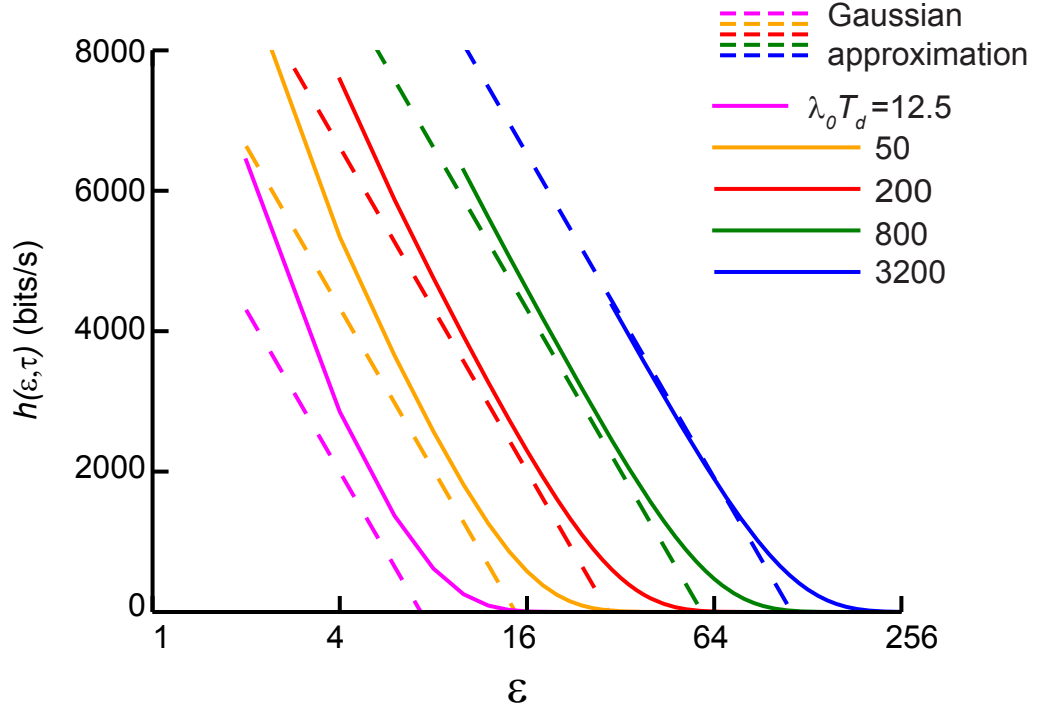
Figure 3.3: Entropy rate calculations for constant-rate Poisson processes with $\lambda_0 T_d = 3200$, 800, 200, 50, and 12.5, with $T_d = 1.734$ ms. These data were recorded using the experimental system described in Chapter 2, but with the feedback disconnected. The solid lines were calculated using the Cohen-Procaccia algorithm, applied to $N_w(t)$ with $w = T_d/4$. Equation 3.9. The dashed lines were calculated using Equation 3.22.

Figure 3.4: Dependence of $h(\varepsilon, \tau)$ on $\varepsilon$ for a) $\tau = T_d/4$ and b) $\tau = 3T_d/4$. In this figure, $\varepsilon$ has the same units as the normalized intensity $I(t)$, which varies between 0 and 1. As one would expect, the dependence of $h$ on $\varepsilon$ is flat, as long as $\varepsilon$ is small compared to the size of the attractor. For both $\tau = T_d/4$ and $\tau = 3T_d/4$, the level of this plateau slowly decreases with increasing embedding dimension $d$, and appears to approach $h_{ks}$.

47

systems generate information. The growth of uncertainty is quantified by the Lyapunov exponents $\mu_i$, and in particular the largest exponent, $\mu_1$. Positive Lyapunov exponents and entropy rate both quantify unpredictability and there is a close relationship between these two quantities. One would expect that if a chaotic system is sampled infrequently ($\tau\mu_1 \gg 1$), successive samples will be uncorrelated because of the growth of uncertainty between measurements. On the other hand, if the interval between successive samples is small ($\tau\mu_1 \ll 1$), one expects strong correlations between adjacent samples and a reduced entropy per sample. Experimental and theoretical work using semiconductor lasers has shown that these considerations are crucial to physical random number generation using chaotic dynamics [64–66]. In the limit that $\tau, \varepsilon \to 0$, $h(\varepsilon, \tau)$ will approach a finite value, the Kolmogorov-Sinai (or metric) entropy, $h_{ks}$ [10, 87–89]. The metric entropy is related to the Lyapunov exponents, $\mu_i$, by

$$h_{ks} = \frac{1}{\log(2)} \sum_{\mu_i > 0} \mu_i. \tag{3.23}$$

We calculated the spectrum of Lyapunov exponents from Equation 2.1, with all of the parameters given in Chapter 2 [50, 90]. There is only one positive Lyapunov exponent with a value of $\mu_1/\log(2) = 345$ bits/s. The Kaplan-Yorke dimension [91] calculated from the Lyapunov spectrum is 3.56.

The ($\varepsilon, \tau$) entropy will have qualitatively different behavior as $\varepsilon \to 0$ depending on the physical origin of unpredictability [10, 80]. In chaotic systems, the entropy rate does not depend on either the sampling rate or the sampling resolution. This property of chaotic systems imposes a theoretical limitation on physical random

number generation. Increasing the speed and resolution of a measurement device cannot in principle increase the entropy that can be harvested from a deterministic chaotic system beyond $h_{ks}$. In contrast to deterministic systems, the, entropy rate of stochastic signals diverges like $-\log(\varepsilon)$ for finite $\tau$ [76, 80].
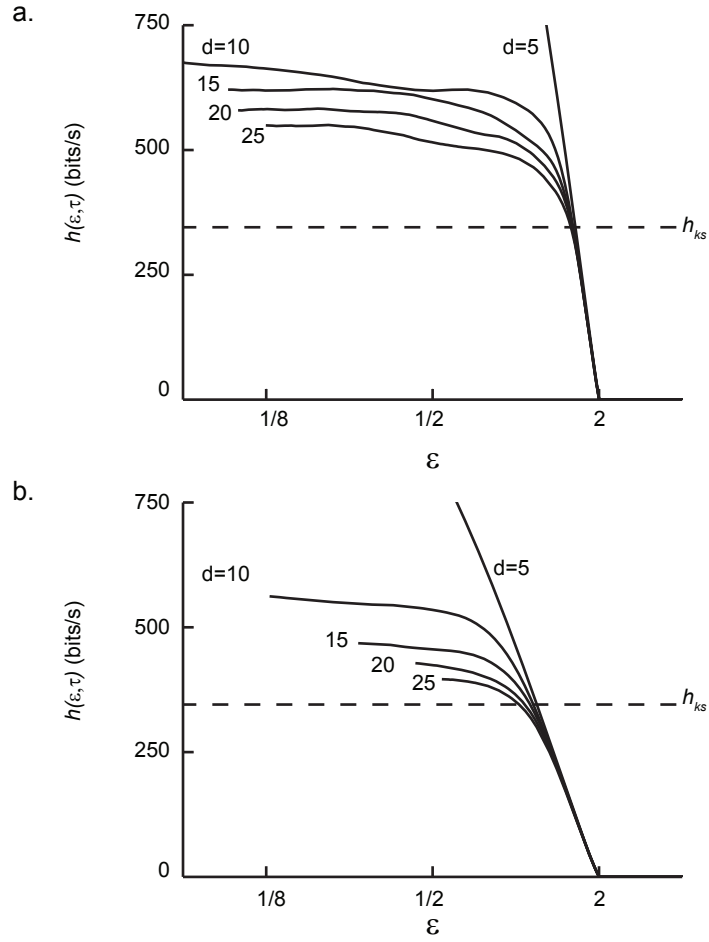
Figure 3.4 shows the dependence of $h(\varepsilon, \tau)$ on $\varepsilon$ for $\tau = T_d/4$ and $\tau = (3/4)T_d$. In this figure, $\varepsilon$ has the same units as the normalized intensity $I(t)$, which varies between 0 and 1. As one would expect, $h$ in independent of $\varepsilon$ as long as $\varepsilon$ is small compared to the size of the attractor. With both $\tau = T_d/4$ and $\tau = 3T_d/4$, the level of this plateau slowly decreases with increasing embedding dimension $d$, and appears to approach $h_{ks}$.

Figure 3.4 shows that the convergence of the entropy estimate with increasing $d$ is rather slow. The comparison of Figure 3.4 a) and 3.4 b) suggests that $\tau = (1/4)T_d$ is too small to resolve the expected entropy rate, $h_{ks}$. Care should be taken when applying this method. The slow convergence of the entropy estimate could lead to too-large estimates of the entropy. Comparing the curves in Figure 3.4 a) for $d = 10$ and $d = 15$, one might imagine that the entropy rate estimate given by these curves is close to its asymptotic value for high $d$, but such an estimate would be off by a factor of two.

## 3.6  Entropy generation in a photon-driven feedback loop

To analyze the photon count data from the experiment described in Chapter 2, we computed $N_w(t)$, the number of photon counts in the interval $[t - w, t]$. We
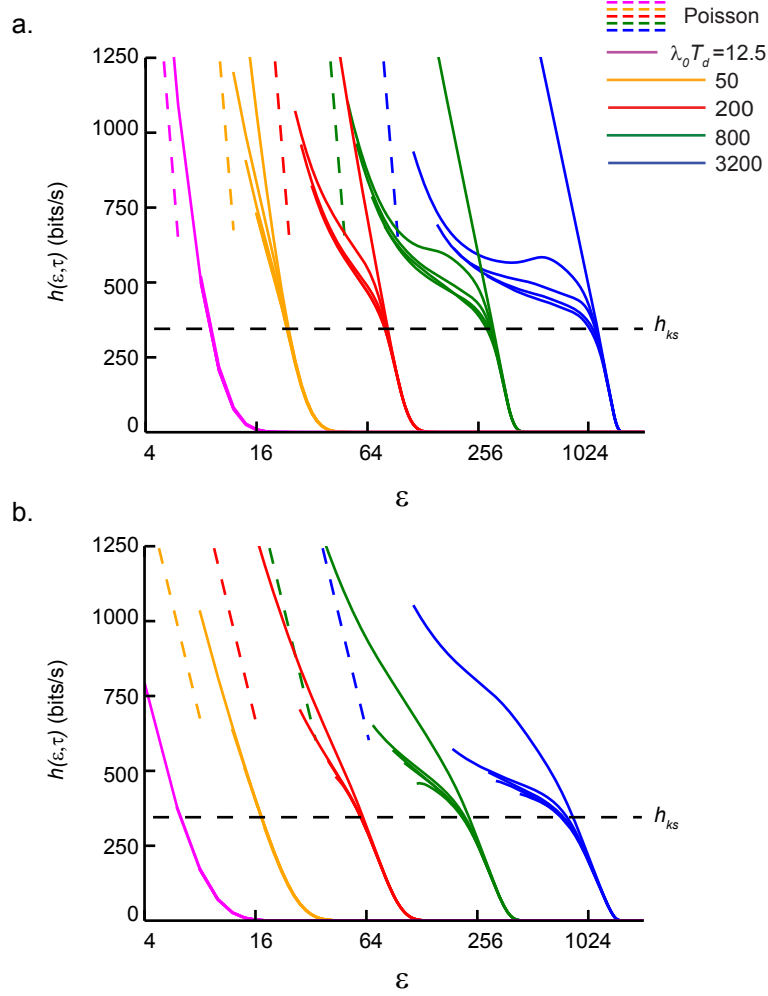
Figure 3.5: Entropy rate of experimental time series. The entropy is calculated from $N_w(t)$, and $\varepsilon$ is measured in photons. $\tau = T_d/4$ is shown in a), and $\tau = (3/4)T_d$ is shown in b). Embedding dimensions of d=5,10,15,20, and 25 are shown. At low photon rates we see a divergence characteristic of a Poisson processes. As the photon rate increases, the dependence of the entropy on $\varepsilon$ becomes progressively flatter, and approaches $h_{ks}$. Across photon rates, we see a divergence of the entropy rate for small $\varepsilon$. The Poisson curves were calculated using Equation 3.22 with a rate of $\lambda_0$.

also chose a rather large value of $\tau$, on the order of $T_d$. These two choices allowed us to detect deterministic chaos in the experimental time series.

Figure 3.5 shows the entropy per unit time calculated from the experiment with both $\tau = (1/4)T_d$ and $\tau = (3/4)T_d$. We see that as the photon rate increases, the dependence of the entropy on $\varepsilon$ becomes progressively flatter at high $\varepsilon$. Furthermore, in the region that this flattening is present, the value of $h(\varepsilon, \tau)$ is close to $h_{ks}$. The flattening of $h(\varepsilon, \tau)$ at high photon rate is another indication that this system behaves more deterministically in the high photon-rate regime. At all photon rates, we see $h(\varepsilon, \tau)$ sharply increases as $\varepsilon$ decreases, which is due to the shot noise inherent in the system. It is natural to compare the entropy rates we observe to a constant-rate Poisson process with the same average rate. In Figure 3.5 a), we see the entropy rate approaching the rate of the Poisson process given by the dashed lines for small $\varepsilon$. In Figure 3.5 b), it is harder to infer the asymptotic behavior for small $\varepsilon$, because we were unable to resolve the value of $h$ with sufficiently small $\varepsilon$.

It's also worth noting that in comparing Figure 3.4, and 3.5, the difference between $\tau = (1/4)T_d$ and $\tau = (3/4)T_d$ is more pronounced in simulation than experiment. The entropy rate also converges faster as $d$ increases in experiment than in simulation.

## 3.7   Comments

At the outset of this project, we had a rather simple question: does discrete noise, for example arising from individual photon arrivals, increase the unpredictabil-

ity of a chaotic system? Another, related question, is whether chaos "amplifies" the discrete noise. As I describe in Chapter 2, we were able to give some insight into these questions by examining the qualitative appearance of the time series and Poincaré sections (Figure 2.3), the variance of $N_w(t)$ (Figure 2.4) and the autocorrelation functions (Figure 2.2). The autocorrelation function was sharply peaked at low photon rates, indicating a lack of temporal correlations. As the photon rate increased, the autocorrelation function developed a complex, oscillatory character with correlations lasting for tens of ms, similar to the deterministic system. The qualitative appearance of both the time series and Poincaré sections confirmed that, as the photon rate $\lambda_0$ increases, deterministic chaos develops from noise. So, in a sense, The lower photon rates are noisier.

We then set out to show these trends by quantifying entropy production. It quickly became apparent that we could not avoid considering three parameters: $w$ (the counting window), $\varepsilon$ (resolution in value), and $\tau$ (time resolution) if we wanted to understand the roles of chaos and shot noise. If we employ the smallest value of $\tau$ possible, and count individual photon arrivals, we are left with the straightforward result of Subsection 3.4.2, that the constant rate Poisson process has the highest achievable entropy. Furthermore, the entropy scales with the photon rate in a straightforward manner, given in Equation 3.13. We are then left with an unsatisfying conclusion: a constant-intensity light source with a high photon rate gives the largest entropy rate. This analysis is unsatisfying because it fails to capture the unpredictability in the chaotic wave forms shown in Figure 2.2. It also fails to capture the comparatively noisy character of the time traces for lower photon rates. In

order to resolve these features of the dynamics, we had to introduce coarse graining in both time ($\tau$ and $w$) and value, $\varepsilon$. The choice of ($\tau$ and $w$) allow for us to resolve the slow intensity fluctuations and the associated uncertainty. The dependence of the entropy on $\epsilon$ showed that at small scales, Poisson shot noise dominates, and at large scales, the chaotic dynamics can be resolved.

### 3.7.1 Broader context

Two prevalent methods have attracted attention for optical random number generation: those based on single photon detection from strongly attenuated light sources [13, 14], and those based on digitized high-speed fluctuations from chaotic lasers [11]. In the former case, the entropy is claimed to originate entirely from quantum mechanical uncertainty, yet in practice these methods are also subject to unpredictable drift and environmental variations. In the latter case, the entropy is attributed to the dynamical unpredictability of chaos, but the unavoidable presence of spontaneous emission is thought to play a role in seeding these macroscopic fluctuations [64, 66]. The system presented here is unprecedented in that it can approach macroscopic chaos from the single photon limit, thereby revealing the transition from noise to chaos. Moreover, the analysis offers a unified measure of entropy that captures both behaviors, and clarifies the relationship between sampling frequency, measurement resolution and entropy rate.

The designer of a physical random number generator must choose the sampling rate and resolution that they will use to collect numbers from a physical

system. These decisions will impact the entropy rate. Heuristically, finer discretization (smaller $\varepsilon$) and more frequent sampling (smaller $\tau$) lead to higher entropy rates, but without the methods presented here it is difficult to assess the dependence of the entropy rate on these parameters in any given system. The statistical tests that are usually used to evaluate physical random number generation [21, 22] were not designed to answer these questions, but rather to certify that a stream of bits is free of bias and correlation. If a random number generator employs post processing (as most do), existing statistical tests applied to the output binary sequence provide no insight into whether the entropy originates from the physical process or the post-processing algorithm employed. We offer a new approach to determine the entropy of a physical process that clarifies the origin and nature of uncertainty and informs the choice of sampling rate and measurement resolution.

# Chapter 4:   Cluster Synchronization and Symmetries in Networks

*This chapter is based on work from the following publications*

## 4.1   Overview

This chapter focuses on synchronization patterns that can emerge in networks of coupled dynamical systems. The symmetries of a network can be used both to predict the synchronization patterns, and to analyze their stability.

This chapter is organized as follows. Section 4.2 provides background and motivation, and introduces the mathematical formulation of the problem of cluster synchronization. Section 4.3 describes the relationship between the symmetries of a network and the possible cluster synchronization patterns. Section 4.4 describes, very briefly, the linear stability analysis of global synchronization. Section 4.5 describes the linear stability analysis of cluster synchronization. Section 4.6

describes the a coordinate transformation that is necessary for this analysis. Section 4.7 describes the experimental system that I used to obtain the experimental demonstration of cluster synchronization shown in Section 4.8. Section 4.9 briefly describes the generalization of the symmetry-based approach to a much larger class of synchronization patterns.

## 4.2   Background

Synchronization in complex networks is essential to the proper functioning of a wide variety of natural and engineered systems, ranging from electric power grids to neural networks [92]. Global synchronization, in which all nodes evolve in unison, is a well-studied effect, the conditions for which are often related to the network structure through the master stability function [27]. Equally important, and perhaps more commonplace, is partial or cluster synchronization (CS), in which patterns or sets of synchronized elements emerge [26]. Recent work on cluster synchronization has been restricted to networks where the synchronization pattern is induced either by tailoring the network geometry or by the intentional introduction of heterogeneity in the time delays or node dynamics [46, 93–99]. These anecdotal studies illustrate the interesting types of cluster synchronization that can occur, and suggest a broader relationship between the network structure and synchronization patterns. Recent studies have begun to draw a connection between network symmetry and cluster synchronization, although all have considered simple networks where the symmetries are apparent by inspection [23–25]. More in-depth studies have been done involving

bifurcation phenomena and synchronization in ring and point symmetry networks [100, 101]. Finally, a form of cluster synchronization can occur in situations where input and output couplings match in a cluster, but there is no symmetry [101, 102].

Here we address the more common case where the intrinsic network symmetries are neither intentionally produced nor easily discerned. We present a comprehensive treatment of cluster synchronization, which uses the tools of computational group theory to reveal the hidden symmetries of networks and predict the patterns of synchronization that can arise. We use irreducible group representations to find a block diagonalization of the variational equations that can predict the stability of the clusters. We further establish and observe a generic symmetry breaking bifurcation termed *isolated desynchronization*, in which one or more clusters lose synchrony while the remaining clusters stay synchronized. The analytical results are confirmed through experimental measurements in a spatiotemporal electro-optic network. By statistically analyzing the symmetries of several types of networks, as well as electric power distribution networks, we argue that symmetries, clusters, and isolated desynchronization can occur in many types of complex networks and are often found concurrently. Throughout we use the abbreviation ID for isolated desynchronization.

## 4.2.1  Coupling – adjacency matrix and Laplacian matrix

Two types of matrices are very commonly used to describe networks [103]: the adjacency matrix and Laplacian matrix. The adjacency matrix is denoted by $A$.

The element $A_{ij}$ is 1 if nodes $i$ is connected to node $j$, and 0 otherwise. Here, we only discuss the case of bidirectional coupling, where $A_{ij} = A_{ji}$, but there are many cases where one might want to consider a network in which there are unidirectional couplings. It's also common to have weighted connections. In this case, the value of $A_{ij}$ is not necessarily 0 or 1, and specifies the strength of the connection between $i$ and $j$. Most of the formalism discussed in this chapter will probably carry over to both weighted and unidirectional connections, but this has not been explored in detail. Typically, the diagonal entries of $A$ are set to 0.

The Laplacian matrix is the same as the adjacency matrix, except for the values of the diagonal elements. In the Laplacian matrix, normally denoted $L$, the diagonal entries are given by the opposite of the row sums.

$$L_{ij} = A_{ij} \text{ for } i \neq j$$
$$L_{ii} = -\sum_{j \neq i} A_{ij}$$

(4.1)

As a consequence of this definition, $\sum_j L_{ij} = 0$. In the next section, I will discuss how this allows for global synchronization.

Except where otherwise noted, this chapter discusses adjacency matrix coupling where all of the links are bidirectional and of equal weight.

## 4.2.2 General model of networks of coupled identical systems

A set of general dynamical equations to describe a network of $N$ coupled identical oscillators are

$$\dot{\mathbf{x}}_i(t) = \mathbf{F}(\mathbf{x}_i(t)) + \sigma \sum_j A_{ij} \mathbf{H}(\mathbf{x}_j), \ i = 1, ..., N,$$

(4.2)

where $\mathbf{x}_i$ is the $n$-dimensional state vector of the $i$th oscillator, $\mathbf{F}$ describes the dynamics of each oscillator, $A$ is a coupling matrix that describes the connectivity of the network, $\sigma$ is the overall coupling strength, and $\mathbf{H}$ is the output function of each oscillator. Eq. 4.2 or its equivalent forms provide the dynamics for many networks of oscillators including all those in Refs. [23–27, 92, 93, 95–97, 99]. This includes some cases of time delays in the coupling functions. As noted in Ref. [92] it is only necessary for the form of the equations of motion or, more importantly, the variational equations to have the form of Eq. 4.2 near the synchronization manifolds. The form of Eq. (4.2) also applies to discrete time systems or more general coupling schemes [104]. And the same form emerges in the more general case for the variational equations where the vector field and the coupling combine into one function, viz. $\mathbf{F}(\mathbf{x}_i(t), \{\mathbf{x}_j(t)\})$, where the argument in brackets is the input of all nodes connected to node $i$, so long as the nodes are treated as having the same basic dynamics. See Ref. [104] for more explanation. Generalizations of Eq. (4.2) have been studied in Refs. [46, 94, 98, 105]. The types of natural and man-made systems which can be modeled by equations of the same form as Eq. (4.2) is large [103, 106].

The same analysis as presented here will apply to more general dynamics. Here, for simplicity, we take all nodes to have identical dynamics and be bidirectionally coupled to other nodes in the network by couplings of the same weight, i.e. $A_{ij}$ is taken to be the (symmetric) adjacency matrix of 1's and 0's with the factor of $\sigma$ controlling the weight of the couplings. The vector field $\mathbf{F}$ can contain self feedback terms. Here we take the self feedback to be identical for all nodes.

59

## 4.3 Symmetries and cluster synchronization

Symmetries are relabelings of the nodes of a network that do not change the equations of motion. Figure 4.1 shows a network with a few symmetries that are apparent by visual inspection. For example, the network can be reflected about the three different axes indicated. It can also be rotated about the central node, either clockwise or counter-clockwise. In total, this network has six symmetries, including the trivial symmetry (the identity). The symmetries of the network form a (mathematical) group $\mathcal{G}$. Each symmetry $g$ of the group can be described by a permutation matrix $R_g$ that re-orders the nodes. These permutation matrices commute with the adjacency matrix, i.e. $A = R_g^T A R_g$ for each $R_g$. As a result, the dynamical equations are unchanged by these operations.

The set of symmetries (or automorphisms) [100, 107] of a network can be quite large, even for small networks, but they can be calculated from $A$ using widely available discrete algebra routines [108, 109]. Figure 4.2a shows three graphs generated by randomly removing 6 edges from an otherwise fully connected 11-node network. Although the graphs appear similar and exhibit no obvious symmetries, the first instance has no symmetries (other than the identity permutation), while the others have 32 and 5,760 symmetries, respectively. So for even a moderate number of nodes (11) finding the symmetries can become impossible by inspection.

Once the symmetries are identified, the nodes of the network can be partitioned into $M$ clusters by finding the "orbits" of the symmetry group: the disjoint sets of nodes that, when all of the symmetry operations are applied, permute among
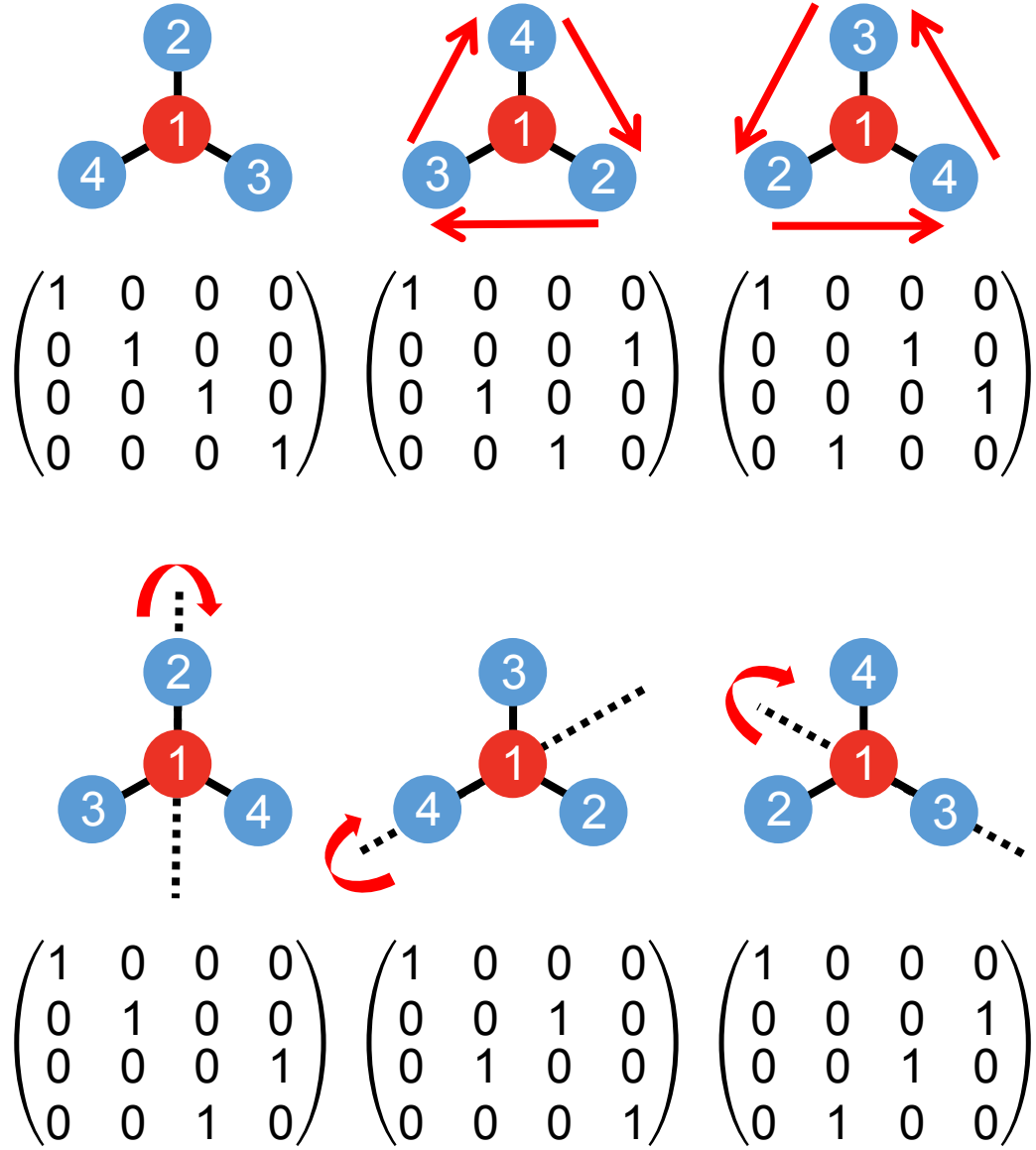
Figure 4.1: Symmetries and clusters in a simple network. All of the symmetry operations of this graph are shown, as well as the permutation matrices that represent them. Note that the outer nodes, 2,3, and 4 can change position under the operations, but node 1 cannot be permuted with 2,3, or 4. It is possible for nodes 2,3, and 4 to synchronize independently of 1. A solution of this form is allowed because if the nodes synchronize in this way, the equations of motion for nodes 2,3,and 4 will be identical.

one another [100]. Because Eq. (4.2) is essentially unchanged by the permutations the dynamics of the nodes in each cluster can be equal, which is exact synchronization. Hence, there are $M$ synchronized motions $\{\mathbf{s}_1, ..., \mathbf{s}_M\}$, one for each cluster. In Fig. 4.2a, the nodes have been colored to show the clusters. For the first example, which has no symmetries, the network divides into $M = N$ trivial clusters with one node in each. The other instances have 5 and 3 clusters, respectively. Once the clusters are identified, Eq. (4.2) can be linearized about a state where synchronization is assumed among all of the nodes within each cluster. This linearized equation is the variational equation and it determines the stability of the clusters.
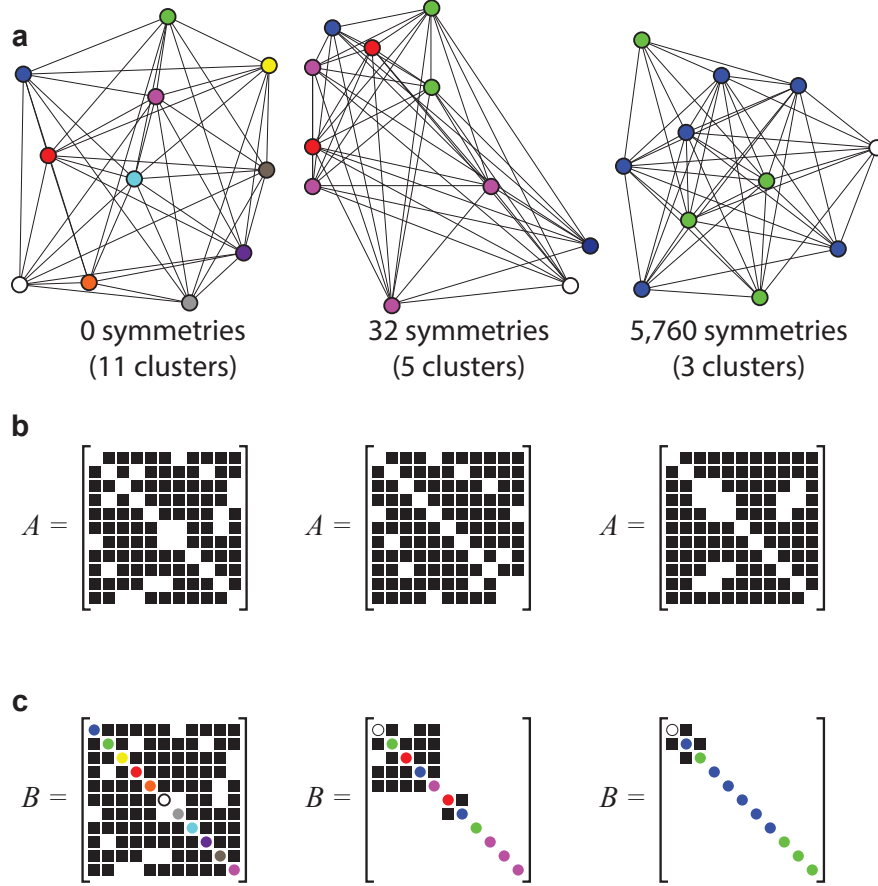
Figure 4.2: Three randomly generated networks with varying amounts of symmetry and associated coupling matrices. (a) Nodes of the same color are in the same synchronization cluster. The colors show the maximal symmetry the network dynamics can have given the graph structure. (b) A graphic showing the structure of the adjacency matrices of each network (black squares are 1, white squares are 0). (c) Block diagonalization of the coupling matrices $A$ for each network. Colors denote the cluster, as in (a). The $2 \times 2$ transverse block for the 32 symmetry case comes from one of the IRRs being present in the permutation matrices two times. The matrices for the 32 symmetry case are given in Equations 4.13,4.14 and 4.15.

## 4.4 Master stability function formalism

The master stability function (MSF) [27] is widely used to analyze the stability of global synchronization in networks with Laplacian coupling. My goal here is to give a very brief review of this technique because the linear stability analysis of cluster synchronization we present here is an extension of the MSF formalism, and a lot of concepts from the MSF formalism will carry over to the analysis of cluster synchrony. In particular, the concepts of the synchronization manifold and the transverse directions will be very important in both.

We consider a system of coupled oscillators described by

$$\dot{\mathbf{x}}_i(t) = \mathbf{F}(\mathbf{x}_i(t)) + \sigma \sum_j L_{ij} \mathbf{H}(\mathbf{x}_j), \; i = 1, ..., N, \tag{4.3}$$

This is the same as Equation 4.2, except that the Laplacian is used in place of the adjacency matrix. By design, Equation 4.3 admits a globally-synchronous solution $\mathbf{x_s} = \mathbf{x_1} = \mathbf{x_2} = \ldots \mathbf{x_s}$. Because the coupling is Laplacian, i.e. the row sums are 0, in the case of global synchronization we have $\sum_j L_{ij} \mathbf{H}(\mathbf{x_s}) = 0$, and Equation 4.3 reduces to

$$\dot{\mathbf{x}}_s(t) = \mathbf{F}(\mathbf{x}_s(t)). \tag{4.4}$$

That is, all of the oscillators evolve in time in exactly the same way as a single oscillator would. This synchronous solution always exists, but is not always stable. To analyze the stability of global synchrony, we consider small perturbations $\delta\mathbf{x}_i(t)$ away from the synchronous solution $\mathbf{x_s}$.

$$\mathbf{x_i}(t) = \mathbf{x_s}(t) + \delta\mathbf{x}_i(t) \tag{4.5}$$

We will then expand Equation 4.3 to first order in this perturbation, obtaining an non-autonomous, linear system of differential equations for $\delta\mathbf{x}_i(t)$.

$$\delta\dot{\mathbf{x}}_i(t) = D\mathbf{F}(\mathbf{x}_s(t))\delta\mathbf{x}_i(t) + \sigma\sum_j L_{ij}D\mathbf{H}(\mathbf{x}_s)\delta\mathbf{x}_j(t) \tag{4.6}$$

Where $D\mathbf{F}$ and $D\mathbf{H}$ are the Jacobian matrices of $\mathbf{F}$ and $\mathbf{H}$.

An important simplification comes from expressing Equation 4.6 in the basis of the eigenvectors of the Laplacian matrix, $\mathbf{v}_i$.

$$\boldsymbol{\eta}_i = \mathbf{v}_i^T \otimes I_n\delta\mathbf{x} \tag{4.7}$$

Here, $I_n$ is the $n \times n$ identity matrix, and the $\otimes$ symbol denotes the Kronecker product. $\boldsymbol{\eta}_i$, is a vector quantity with the same dimensionality as the dynamics of a single node, $n$.

$$\dot{\boldsymbol{\eta}}_i(t) = [D\mathbf{F}(\mathbf{x}_s(t)) + \sigma\lambda_i D\mathbf{H}(\mathbf{x}_s)]\boldsymbol{\eta}_i(t) \tag{4.8}$$

Here, $i$ indexes the eigenvectors and eigenvalues ($\lambda_i$) of the Laplacian.

The strength of the MSF formalism is that it decouples network connectivity from the dynamics. Given a particular dynamical system, (e.g. Lorenz oscillators), the stability of global synchronization can be determined from the eigenvalues of the Laplacian matrix alone. By writing the variational equations is this basis, the different modes of the network dynamics uncouple. Equation 4.6 is $nN$-dimensional: it has $N$ nodes, and each node has $n$ dimensional dynamics. In contrast, Equation 4.8 is $n$-dimensional. Furthermore, $\sigma\lambda_i$ can be viewed as a parameter that encapsulates the coupling strength and the network topology. The magnitudes of the perturbations $\eta_i(t)$, will either grow or shrink exponentially in time. This rate of

growth or decay is referred to as a transverse Lyapunov exponent. The systematic dependence of the transverse Lyapunov exponents on the $\sigma \lambda_i$ is called the master stability function.

Laplacian matrices have always a trivial eigenvector, $\mathbf{v}_1 = [1, 1, \ldots, 1]$, with an eigenvalue of 0. In the context of synchronization, this vector has a physical interpretation: perturbations in this direction effect all nodes equally, and so do not break synchrony. The other eigenvectors are perpendicular to $\mathbf{v_1}$, and perturbations along these directions will tend to drive the network out of synchrony.

The analysis of cluster synchronization will proceed along very similar lines. It will not be possible to reduce the dimensionality of the problem as it is in the case of global synchrony. In the case of cluster synchrony, there will be more synchronous directions. If there are $M$ clusters, there will be $M$ orthogonal vectors that do not break cluster synchrony. It will also be possible to find directions that are transverse to a particular cluster. Section 4.6 describes how to find these directions, the basis vectors of the IRR coordinate system. Section 4.5 describes the form that the variational equations take in this coordinate system.

## 4.5   Variational equations in IRR Coordinates

Equation (4.2) is expressed in the "node" coordinate system, where the subscripts $i$ and $j$ are identified with enumerated nodes of the network. Beyond identifying the symmetries and clusters, group theory also provides a powerful way to transform the variational equations to a new coordinate system in which the trans-

formed coupling matrix $B = TAT^{-1}$ has a block diagonal form that matches the cluster structure, as described below. The transformation matrix $T$ is not a simple node re-ordering, nor is it an eigendecomposition of $A$. The process for computing $T$ is nontrivial, and involves finding the irreducible representations (IRR) of the symmetry group. We call this new coordinate system the "IRR coordinate system." In section 4.6 we show the steps necessary to obtain the symmetries, clusters, and the transformation $T$.

Once we have $T$ we can transform the variational equations as follows. Let $\mathcal{C}_m$ be the set of nodes in the $m$th cluster with synchronous motion $\mathbf{s}_m(t)$. Then the original variational equations about the synchronized solutions are (in vectorial form and in the node coordinates),

$$\delta\dot{\mathbf{x}}(t) = \left[\sum_{m=1}^{M} E^{(m)} \otimes D\mathbf{F}(\mathbf{s}_m(t)) + \sigma A \sum_{m=1}^{M} E^{(m)} \otimes D\mathbf{H}(\mathbf{s}_m(t))\right] \delta\mathbf{x}(t), \qquad (4.9)$$

where the $Nn$-dimensional vector $\delta\mathbf{x}(t) = [\delta\mathbf{x}_1(t)^T, \delta\mathbf{x}_2(t)^T, ..., \delta\mathbf{x}_N(t)^T]^T$ and $E^{(m)}$ is an $N$-dimensional diagonal matrix such that

$$E_{ii}^{(m)} = \begin{cases} 1, & \text{if } i \in \mathcal{C}_m, \\ 0, & \text{otherwise,} \end{cases} \qquad (4.10)$$

$i = 1, ..., N$. Note that $\sum_{m=1}^{M} E^{(m)} = I_N$, where $I_N$ is the $N$-dimensional identity matrix.

Applying $T$ to Eq. (4.9) we arrive at the variational matrix equation shown in Eq. (4.11),where $\boldsymbol{\eta}(t) = T \otimes I_n \, \delta\mathbf{x}(\mathbf{t})$, $J^{(m)}$ is the transformed $E^{(m)}$, and $B$ is the

block diagonalization of the coupling matrix $A$,

$$\dot{\boldsymbol{\eta}}(t) = \left[ \sum_{m=1}^{M} J^{(m)} \otimes D\mathbf{F}(\mathbf{s}_m(t)) + \sigma B \otimes I_n \sum_{m=1}^{M} J^{(m)} \otimes D\mathbf{H}(\mathbf{s}_m(t)) \right] \boldsymbol{\eta}(t), \quad (4.11)$$

where we have linearized about synchronized cluster states $\{\mathbf{s}_1, ..., \mathbf{s}_M\}$, $\boldsymbol{\eta}(t)$ is the vector of variations of all nodes transformed to the IRR coordinates and $D\mathbf{F}$ and $D\mathbf{H}$ are the Jacobians of the nodes' vector field and coupling function, respectively. We note that this analysis holds for any node dynamics, steady state, periodic, chaotic, etc.

We can write the block diagonal $B$ as a direct sum $\bigoplus_{l=1}^{L} I_{d^{(l)}} \otimes C^l$, where $C^l$ is a (generally complex) $p_l \times p_l$ matrix with $p_l =$ the multiplicity of the $l$th IRR in the permutation representation $\{R_g\}$, $L =$ the number of IRRs present, and $d^{(l)} =$ the dimension of the $l$th IRR, so that $\sum_{l=1}^{L} d^{(l)} p_l = N$ [110, 111]. For many transverse blocks $C^l$ is a scalar, i.e. $p_l = 1$. However, the trivial representation ($l = 1$) which is associated with the motion in the synchronization manifold has $p_1 = M$. Note that the vector field $\mathbf{F}$ can contain a self feedback term $\beta \mathbf{x}_i$ as in the experiment and other feedbacks are possible, e.g. row sums of $A_{ij}$, as long as those terms commute with the $R_g$. In all these cases, the $B$ matrix will have the same structure.

Figure 4.2c shows the coupling matrix $B$ in the IRR coordinate system for the three example networks. The upper-left block is an $M \times M$ matrix that describes the dynamics within the synchronization manifold. The remaining diagonal blocks describe motion transverse to this manifold and so are associated with loss of synchronization. Thus, the diagonalization completely decouples the transverse variations from the synchronization block, and partially decouples the variations

among the transverse directions. In this way the stability of the synchronized clusters can be calculated using the separate, simpler, lower dimensional ODEs of the transverse blocks to see if the non-synchronous transverse behavior decays to zero.

## 4.6 Calculating the IRR transformation

Below are the steps necessary to determine the symmetries of the network, obtain the clusters, find the irreducible representations (IRRs), and the most crucial part, calculate the transformation $T$ from the node coordinates to the IRR coordinates that will block diagonalize $A$, since $A$ commutes with all symmetries of the group [112].

Using the discrete algebra software [108, 109] it is straightforward to determine the group of symmetries of $A$, extract the orbits which give the nodes in each cluster and extract the permutation matrices $R_g$, and use the character table of the group and the traces of the $R_g$'s to determine which IRRs are present in the node-space representation of the group. *Remark:* This step is discussed in any book on representations of finite groups (e.g. Ref. [107]). After this we put each $R_g$ into its appropriate conjugacy class. To generate the transformaion $T$ from the group information and we have written code on top of the discrete algebra software which for each IRR present constructs the projection operator $P^{(l)}$ [107] from the node coordinates onto the subspace of that IRR, where $l$ indexes the set of IRRs present. This is done by calculating,

$$P^{(l)} = \frac{d^{(l)}}{h} \sum_{\mathcal{K}} \alpha_{\mathcal{K}}^{(l)} \sum_{g \in \mathcal{K}} R_g \qquad (4.12)$$

69

where $\mathcal{K}$ is a conjugacy class, $\alpha_{\mathcal{K}}^{(l)}$ is the character of that class for the $l$th IRR, $d^{(l)}$ is the dimension of the $l$th IRR and $h$ is the order (size) of the group. *Remark: The trivial representation (all IRR matrices=1 and $\alpha^{(l)} = 1$) is always present and is associated with the synchronization manifold. All other IRRs are associated with transverse directions.* Next we use singular value decomposition on $P^{(l)}$ to find the basis for the projection subspace for the $l$th IRR. Finally, we construct $T$ by stacking the row basis vectors of all the IRRs which will form an $N \times N$ matrix.

We show the results of this applied to the 32-symmetry case in Fig. 4.2:

$$A = \begin{bmatrix} 0 & 1 & 1 & 1 & 0 & 1 & 1 & 1 & 1 & 1 & 1 \\ 1 & 0 & 1 & 1 & 1 & 1 & 0 & 1 & 1 & 1 & 1 \\ 1 & 1 & 0 & 1 & 1 & 1 & 1 & 1 & 0 & 1 & 1 \\ 1 & 1 & 1 & 0 & 1 & 1 & 1 & 1 & 1 & 1 & 1 \\ 0 & 1 & 1 & 1 & 0 & 1 & 1 & 1 & 1 & 1 & 0 \\ 1 & 1 & 1 & 1 & 1 & 0 & 1 & 1 & 1 & 1 & 1 \\ 1 & 0 & 1 & 1 & 1 & 1 & 0 & 1 & 1 & 1 & 1 \\ 1 & 1 & 1 & 1 & 1 & 1 & 1 & 0 & 1 & 0 & 1 \\ 1 & 1 & 0 & 1 & 1 & 1 & 1 & 1 & 0 & 1 & 1 \\ 1 & 1 & 1 & 1 & 1 & 1 & 1 & 0 & 1 & 0 & 0 \\ 1 & 1 & 1 & 1 & 0 & 1 & 1 & 1 & 1 & 0 & 0 \end{bmatrix} \quad (4.13)$$

The nontrivial clusters are the nodes [1, 8], [2, 3, 7, 9], [4, 6], [5, 10] (the numbering of nodes matches the row and column numbers of $A$). The transformation matrix is,

$$
T = \frac{1}{2}
\begin{bmatrix}
0 & 0 & 0 & 0 & 0 & 0 & 0 & 0 & 0 & 0 & 2 \\
0 & 0 & 0 & -\sqrt{2} & 0 & -\sqrt{2} & 0 & 0 & 0 & 0 & 0 \\
-\sqrt{2} & 0 & 0 & 0 & 0 & 0 & 0 & -\sqrt{2} & 0 & 0 & 0 \\
0 & 0 & 0 & 0 & -\sqrt{2} & 0 & 0 & 0 & 0 & -\sqrt{2} & 0 \\
0 & -1 & -1 & 0 & 0 & 0 & -1 & 0 & -1 & 0 & 0 \\
-\sqrt{2} & 0 & 0 & 0 & 0 & 0 & 0 & \sqrt{2} & 0 & 0 & 0 \\
0 & 0 & 0 & 0 & -\sqrt{2} & 0 & 0 & 0 & 0 & \sqrt{2} & 0 \\
0 & 0 & 0 & -\sqrt{2} & 0 & \sqrt{2} & 0 & 0 & 0 & 0 & 0 \\
0 & -1 & 1 & 0 & 0 & 0 & -1 & 0 & 1 & 0 & 0 \\
0 & 0 & \sqrt{2} & 0 & 0 & 0 & 0 & 0 & -\sqrt{2} & 0 & 0 \\
0 & -\sqrt{2} & 0 & 0 & 0 & 0 & \sqrt{2} & 0 & 0 & 0 & 0
\end{bmatrix}
\tag{4.14}
$$

And the block diagonal coupling matrix is, $0.75$

$$
B =
\begin{bmatrix}
0 & -\sqrt{2} & -\sqrt{2} & 0 & -2 & 0 & 0 & 0 & 0 & 0 & 0 \\
-\sqrt{2} & 1 & 2 & 2 & 2\sqrt{2} & 0 & 0 & 0 & 0 & 0 & 0 \\
-\sqrt{2} & 2 & 1 & 1 & 2\sqrt{2} & 0 & 0 & 0 & 0 & 0 & 0 \\
0 & 2 & 1 & 1 & 2\sqrt{2} & 0 & 0 & 0 & 0 & 0 & 0 \\
-2 & 2\sqrt{2} & 2\sqrt{2} & 2\sqrt{2} & 2 & 0 & 0 & 0 & 0 & 0 & 0 \\
0 & 0 & 0 & 0 & 0 & -1 & -1 & 0 & 0 & 0 & 0 \\
0 & 0 & 0 & 0 & 0 & -1 & -1 & 0 & 0 & 0 & 0 \\
0 & 0 & 0 & 0 & 0 & 0 & 0 & -1 & 0 & 0 & 0 \\
0 & 0 & 0 & 0 & 0 & 0 & 0 & 0 & -2 & 0 & 0 \\
0 & 0 & 0 & 0 & 0 & 0 & 0 & 0 & 0 & 0 & 0 \\
0 & 0 & 0 & 0 & 0 & 0 & 0 & 0 & 0 & 0 & 0
\end{bmatrix}
\tag{4.15}
$$

$B$ has a block-diagonal structure. The $5 \times 5$ block describes motion in the synchronization manifold. Each of the 5 vectors acted on by this block corresponds to a cluster. The other blocks correspond to transverse directions. Note that the $2 \times 2$ block couples transverse perturbations to the red and blue clusters shown in Figure 4.1 b. This means that the red and blue clusters are intertwined. For given parameter values, either both or neither of these clusters synchronize.

## 4.7 Experimental system

Figure 4.3a shows the optical system used to study cluster synchronization. Light from a 1550 nm light emitting diode (LED) passes through a polarizing beam-splitter (PBS) and quarter wave plate (QWP), so that it is circularly polarized when it reaches the spatial light modulator (SLM). The SLM surface imparts a programmable spatially-dependent phase shift $x$ between the polarization components of the reflected signal, which is then imaged, through the polarizer, onto an infrared camera [32]. The relationship between the phase shift $x$ applied by the SLM and the normalized intensity $\mathcal{I}$ recorded by the camera is $\mathcal{I}(x) = (1 - \cos x)/2$. The resulting image is then fed back through a computer to control the SLM.

The SLM (Boulder Nonlinear Systems P512-1550) has an active area of $7.68 \times 7.68$ mm$^2$ and a resolution of 512 x 512 pixels. The camera (Goodrich SU320KTSW-1.7RT/RS170) has an indium gallium arsenide focal plane array (FPA) with $320 \times 256$ pixels and an area of 8 x 6.4 mm$^2$. Using a lens assembly, the SLM was imaged onto the camera with the magnification and orientation adjusted so that each $2 \times 2$ pixel area on the SLM is projected onto a camera pixel. The camera's frame rate was about 8 Hz and was synchronized with the SLM's refresh rate.

Each oscillator in equation (5) corresponds to a square patch of $16 \times 16$ pixels on the SLM, which is imaged onto an $8 \times 8$ pixel region of the camera's FPA. The intensity $\mathcal{I}(x)$ is the average of camera pixel values in this area. The same phase shift $x$ is applied by each of the SLM pixels in the patch. We employ a spatial calibration and lookup table to compensate for inhomogeneities in the SLM.
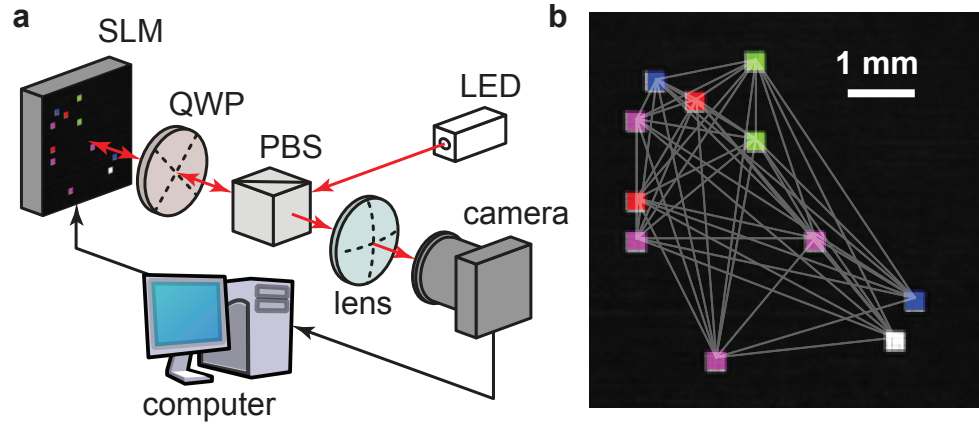
Figure 4.3: Experimental configuration. a) Light is reflected from the SLM, and passes though polarization optics, so that the intensity of light falling on the camera is modulated according the phase shift introduced by the SLM. Coupling and feedback are implemented by a computer. b) An image of the SLM recorded by the camera in this configuration. Oscillators are shaded to show which cluster they belong to, and the connectivity of the network is indicated by superimposed gray lines. The phase shifts applied by the square regions are updated according to equation (4.16).

The dynamical oscillators that form the network are realized as square patches of pixels selected from a $32 \times 32$ tiling of the SLM array. Figure 4.3b shows an experimentally measured camera frame captured for one of the 11-node networks considered earlier in Fig. 4.2 (A full video is presented in the Supplementary Movie 1). The patches have been falsely colored to show the cluster structure, and the links of the network are overlaid to illustrate the connectivity. The phase shift of the $i$th region, $x_i$, is updated iteratively according to:

$$x_i^{t+1} = \left[ \beta \mathcal{I}(x_i^t) + \sigma \sum_j A_{ij} \mathcal{I}(x_j^t) + \delta \right] \mod 2\pi \qquad (4.16)$$

where $\beta$ is the self feedback strength, and the offset $\delta$ is introduced to suppress the trivial solution $x_i = 0$. Eq. (4.16) is a discrete time equivalent of Eq. (4.2). Depending on the values of $\beta$, $\sigma$ and $\delta$, Eq. (4.16) can show constant, periodic or chaotic dynamics. There are no experimentally-imposed constraints on the adjacency matrix $A_{ij}$, which makes this system an ideal platform to explore synchronization in complex networks.

## 4.8 Experimental results

Figure 4.4 plots the time-averaged root-mean square (RMS) synchronization error for all four of the nontrivial clusters shown in Fig. 4.3b, as a function of the feedback strength $\beta$, holding $\sigma$ constant. We find qualitatively similar results if $\sigma$ is chosen as a bifurcation parameter with $\beta$ held constant. In Fig. 4.4c-e, we plot the observed intracluster deviations $(x_i^t - \overline{x}^t)$ for three specific values of $\beta$ indicated by the vertical lines in Fig. 4.4a-b, showing different degrees of partial synchronization
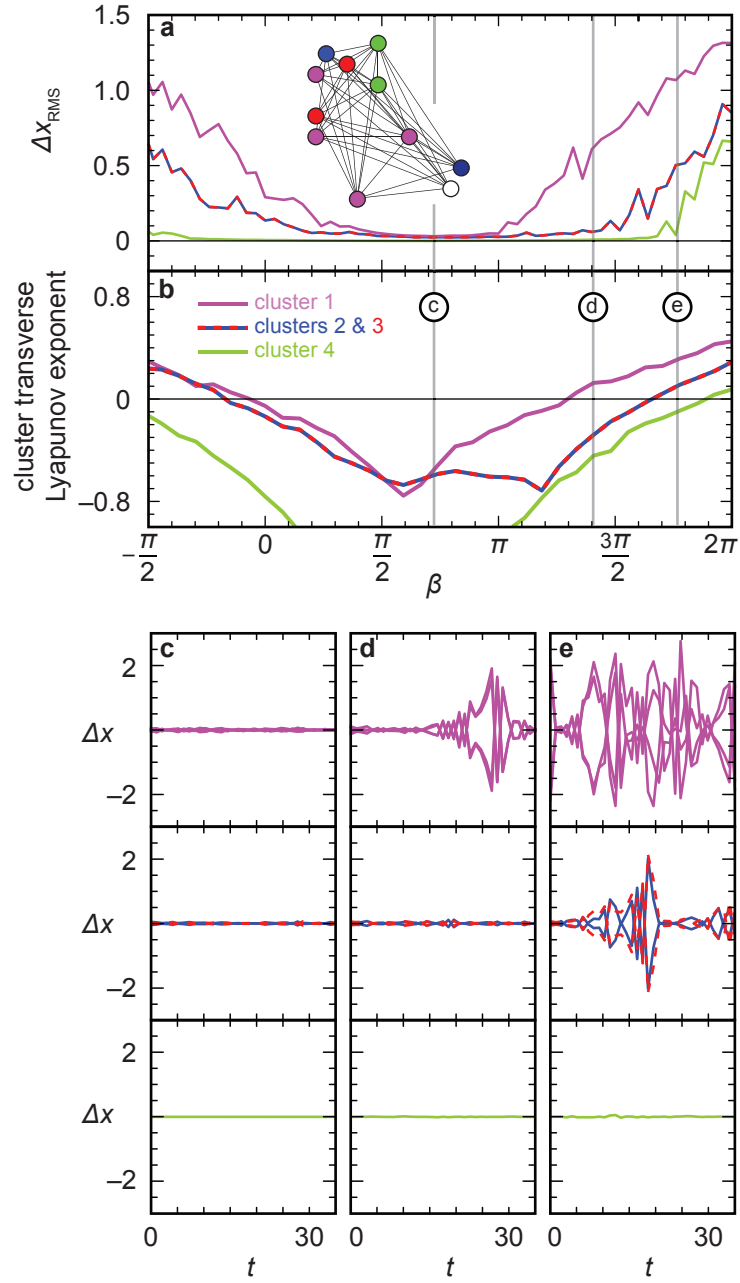
Figure 4.4: Experimental observation of isolated and intertwined desynchronization. a) Cluster synchronization error as the self feedback, $\beta$ is varied. For all cases considered, $\delta = 0.525$ and $\sigma = 0.6\pi$. Colors indicate the cluster under consideration and are consistent with Fig. 4.2. b) MLE calculated from simulation. c-e) Synchronization error time traces for the four clusters, showing the isolated desynchronization of the magenta cluster and the isolated desynchronization of the intertwined blue and red clusters.

that can occur, depending on the parameters.

The phase shifts imparted by each oscillator $x_i^t$ are recorded and used to determine the degree of synchronization, as shown in Fig 3. An individual oscillator's deviation from synchronization at a given time as shown in Fig. 3c-e is measured by $\Delta x_i^t = (x_i^t - \bar{x}^t)$, where $\bar{x}^t$ denotes a spatial average of the phases of all of the nodes within a particular cluster at time t. To quantify the degree of synchronization within a cluster as shown in Fig. 3a, we calculate the RMS synchronization error $\Delta x_{\text{RMS}} \equiv \left( \overline{\langle (x_i^t - \bar{x}^t)^2 \rangle_T} \right)^{1/2}$, where $\langle \bullet \rangle_T$ indicates an average over a time interval $T$ (here taken to be 500 iterations).

Together, Fig. 4.4a and Figs. 4.4c-e illustrate two examples of a bifurcation commonly seen in experiment and simulation: isolated desynchronization, where one or more clusters lose stability, while all others remain synchronized. At $\beta = 0.72\pi$ (Fig. 4.4c), all four of the clusters synchronize. At $\beta = 1.4\pi$ (Fig. 4.4d), the magenta cluster, which contains four nodes, has split into two smaller clusters of 2 nodes each, while the other two clusters remain synchronized.

Between $\beta = 0.72\pi$ and $\beta = 1.76\pi$, two clusters, shown in Fig. 4.2 as red and blue, undergo isolated desynchronization together. In Fig. 4.4a, the synchronization error curves for these two clusters are visually indistinguishable. The synchronization of these two clusters is intertwined: they will always either synchronize together or not at all. While it is not obvious from a visual inspection of the network that the red and blue clusters should form at all, their intertwined synchronization properties can be understood intuitively by examining the connectivity of the network. Each of the two nodes in the blue cluster is coupled to exactly one node in the red

cluster. If the blue cluster is not synchronized, the red cluster cannot synchronize because its two nodes are receiving different input. The group analysis treats this automatically and yields a transverse $2 \times 2$ block in Fig. 4.2c.

The isolated desynchronization bifurcations we observe are predicted by computation of the maximum Lyapunov exponent (MLE) of the transverse blocks of Eq. (4.11), shown in Fig. 4.4. The region of stability of each cluster is predicted by a negative MLE. While there are four clusters in this network, there are only three MLEs: the two intertwined clusters are described by a 2-dimensional block in the block-diagonalized coupling matrix $B$. These stability calculations reveal the same bifurcations as seen in the experiment.

### 4.8.1 Subgroup decomposition and isolated desynchronization

The existence of isolated desynchronizations in the network experiments raises several questions. Since the network is connected why doesn't the desynchronization pull other clusters out of sync? What is the relation of ID to cluster structure and network symmetry? Is ID a phenomenon that is common to many networks? We provide answers to all these questions using geometric decomposition of a group that was developed in [113, 114]. This technique enables a finite group to be written as a direct product of subgroups $\mathcal{G} = \mathcal{H}_1 \times ... \times \mathcal{H}_\nu$ where $\nu$ is the number of subgroups and all the elements in one subgroup commute with all the elements in any other subgroup. This means that the set of nodes permuted by one subgroup is disjoint from the set of nodes permuted by any other subgroup. Then each cluster (say, $\mathcal{C}_j$) is

permuted only by one of the subgroups (say, $\mathcal{H}_k$), but not by any others. There can be several clusters permuted by one subgroup. This is the case of the red and blue clusters in the 32 symmetry network in Fig.4.2, because the associated $\mathcal{H}_k$ cannot have a geometric decomposition, but may have a more structured decomposition such as a wreath product [115].

We can show that the above decomposition guarantees that the nodes associated with different subgroups all receive the same *total* input from the other subgroups' nodes. Hence, nodes of each cluster will not see the effects of individual behavior of the other clusters associated with different subgroups. This enables the clusters to have the same synchronized dynamics even when another cluster desynchronizes. If that state is stable we have ID.

To see this let $\mathcal{H}_k$, a subgroup of $\mathcal{G}$, permute only cluster $\mathcal{C}_m$ and $\pi$ be the permutation on the indices of nodes in $\mathcal{C}_m$ for one permutation $R_g$, $g \in \mathcal{H}_k$. Assume $\mathbf{x}_i$ is not in $\mathcal{C}_m$ so it is not permuted by $R_g$ and recall that $A$ commutes with all permutations in $\mathcal{G}$, then we have (just concentrating on the terms from $\mathcal{C}_m$),

$$[R_g \dot{\mathbf{x}}(t)]_i = \dot{\mathbf{x}}_i(t) = ... + \sigma [R_g A \mathbf{H}(\mathbf{x})]_i = ... + \sigma [A R_g \mathbf{H}(\mathbf{x})]_i = ... + \sigma \sum_{j \in \mathcal{C}_m} A_{ij} \mathbf{H}(\mathbf{x}_{\pi(j)}),$$

$$(4.17)$$

where $\pi(l)$ is, in general, another node in $\mathcal{C}_m$ and the sums over other clusters are unchanged. This shows that all nodes in $\mathcal{C}_m$ are coupled into the $i$th node in the same way (the same $A_{ij}$ factor). Similarly, if we use a permution $R_{g'}$ on the cluster $\mathcal{C}_{m'}$ containing $\mathbf{x}_i$ we can show that all the nodes of $\mathcal{C}_{m'}$ are coupled in the same

way to the nodes in $\mathcal{C}_m$. Hence, nodes of $\mathcal{C}_{m'}$ each receive the same input sum from the nodes of $\mathcal{C}_m$ whether the nodes of $\mathcal{C}_m$ are synchronized or not. This explains how the cluster $\mathcal{C}_m$ can become desynchronized, but the nodes of $\mathcal{C}_{m'}$ can still be synchronized – they all have the same input despite the $\mathcal{C}_m$ desynchronization, thus making the $\mathcal{C}_{m'}$ synchronous state flow invariant. If it is also stable, this is the case of ID. This argument is easily generalized to the case when $\mathcal{H}_k$ permutes nodes of several clusters as this will just add other similar sums to Eq. (4.17). The latter case explains the intertwined desynchronization in the experiment and is a more general form of ID.

## 4.9   Generalizations

The symmetry-based analysis described allows for the linear stability analysis of cluster synchrony in arbitrary networks. This is a major step forward, but there is more to do.

So far, we have described how to analyze the stability of one synchronization pattern. The orbits of the isomorphism group specify the maximally-symmetric pattern, the pattern with the smallest number of clusters possible with adjacency matrix coupling. We have already seen that other cluster-synchronized states are possible. After an isolated desynchronization, the network is often in a dynamical state that still has clusters. We need a formalism that will predict the stability of these patterns.

We also have not considered the case of Laplacian coupling. We already know

that Laplacian coupling allows for global synchronization, and we will see that it allows for more complex synchronization patterns as well.

We will see that a given network can support a large number of synchronization patterns. One very simple example of a 5-node network we will consider has 12 possible synchronization patterns. I don't know how the number of patterns will scale with the size of the network, but the number of possible synchronization patterns in a large network has the possibility of being combinatorially huge. Consider, for example, how many ways an all-to-all coupled network of $N$ oscillators could possibly split into two equal clusters. Of course, a huge variety of unequal clusterings are also possible in an all-to-all coupled network [116]. As I will describe in Chapter 5, a nonlocal ring coupling configuration also supports a vast (and yet unquantified) number of multistable "incoherent" states.

So, for now, enumerating all of the synchronization patterns possible in a large network is a challenge, because there are often a lot of them. But, thanks to recent work by Francesco Sorrentino and Lou Pecora, it is now possible to predict and analyze the stability of every possible cluster-synchronous state [117]. In this section, I will give a simple example network with 5 nodes, and 12 possible synchronization patterns. I will describe how to predict those patterns, and briefly indicate how the linear stability analysis will proceed. Details can be found in [117]. Finally, I will show the experimental confirmation of some of the new types of patterns.

### 4.9.1  Subgroup clusters

The network we will consider is given by the Laplacian matrix

$$
L = \begin{bmatrix}
-3 & 1 & 0 & 1 & 1 \\
1 & -3 & 1 & 0 & 1 \\
0 & 1 & -3 & 1 & 1 \\
1 & 0 & 1 & -3 & 1 \\
1 & 1 & 1 & 1 & -4
\end{bmatrix} . \tag{4.18}
$$

This network and all of the cluster synchronization patterns it supports are shown in Figure 4.5. The patterns A1,..., A5 arise due to subgroups of the graph's automorphism group. The decomposition of a group into a direct product of subgroups, i.e. $\mathcal{G} = \mathcal{H}_1 \times ...\mathcal{H}_i... \times \mathcal{H}_\nu$, can be accomplished using computational group theory software [113, 114]. An individual subgroup $\mathcal{H}_i$ can be excluded, and a new group can be constructed $\mathcal{G}' = \mathcal{H}_1 \times ... \times \mathcal{H}_\nu$. The new group $\mathcal{G}'$ has its own orbits, and the orbits of each subgroup will yield a cluster pattern, just as the orbits of the full group do. The construction of the variational equations follows the same lines as described in Sections 4.6 and 4.5, except one considers $\mathcal{G}'$ rather than the whole group.

### 4.9.2  Laplacian coupling and merged clusters

Laplacian coupling allows for merged clusters. For example, L1 is the merger of the trivial cluster, node (5), with the cluster (1,2,3,5). In general, merged clusters are formed by merging clusters that arise due the symmetries of the adjacency matrix. Not all clusters can merge. For example, in the pattern A2, node (5) can't join either of the other clusters. There isn't really a good way to determine which mergers are possible, except by evaluating each one individually. It is straightforward, but
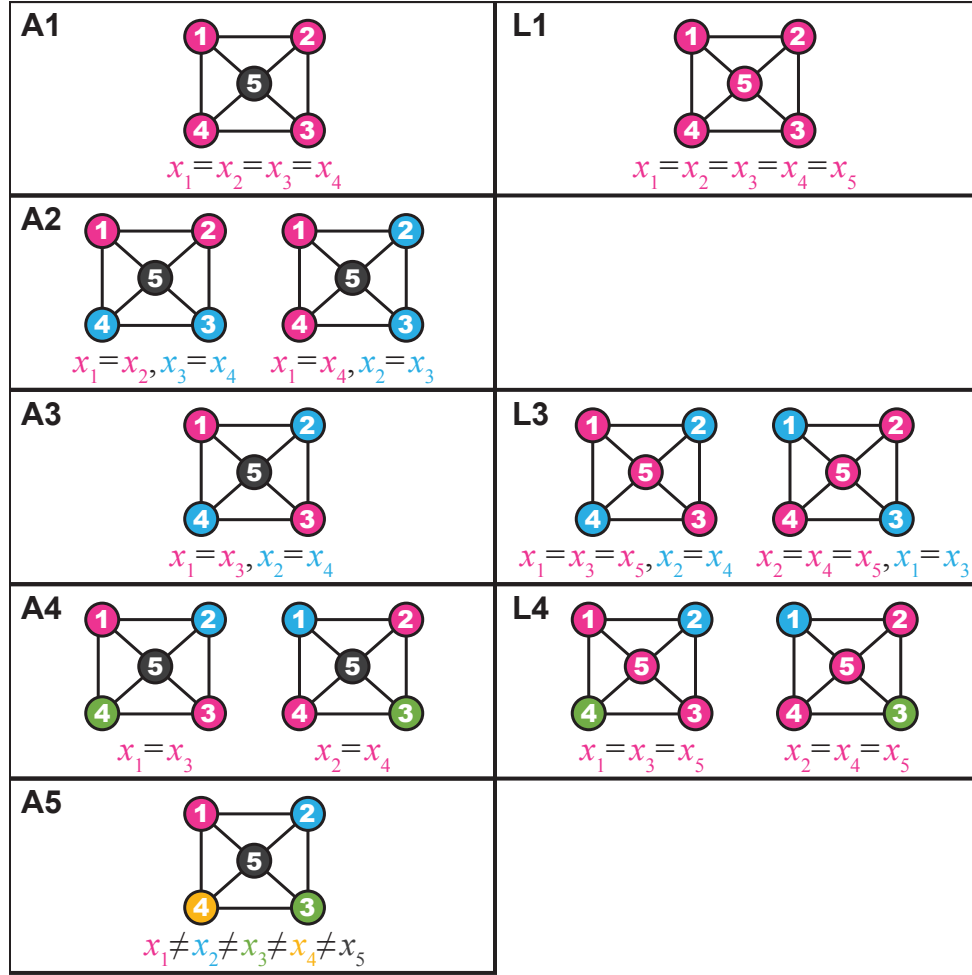
Figure 4.5: All of the synchronization patterns of a small network. The patterns A1,...,A5 are due to symmetries of the adjacency matrix. The patterns L1, L3, and L4 are only possible with Laplacian coupling.

slightly tedious, to verify by hand that the synchronization patterns L1, L3, and L4 satisfy the equations of motion.

There is a better way to determine if it is possible for a given merger to happen than direct examination of the equations of motion. Note that, according to Equation 4.3, the coupling term vanishes between synchronized nodes. Deleting links between nodes that are synchronized in a *proposed* merged-cluster state leads to a new, *dynamically-equivalent network*. If the proposed synchronization pattern is allowed by the symmetries of the *dynamically-equivalent network*, then the merged cluster state is possible. Merged cluster states will have both new synchronous and new transverse directions.

### 4.9.3 Experimental observation

We show subgroup and Laplacian clusters using the experimental system described in 4.7. Figure 4.6 shows the experimental synchronization error for each synchronization pattern as a function of the parameter $\sigma$. For these measurements, $\beta = 1.45\pi$, and $\sigma$ was decreased from $\pi$ to 0 in steps of $\pi/50$, with 1000 iterations at each value of $\sigma$. The phases $x_i$ were not reinitialized when the values of $\sigma$ were updated. We plot the pattern synchronization error. This quantity measures the extent to which the nodes synchronize in one of the patterns shown in Figure 4.5, and is defined as the average over all clusters under consideration (e.g. the clusters $(1, 5, 3)$ and $(2, 4)$ for L3), of the time average of $\langle |x_i - \langle x \rangle | \rangle$, where $\langle \bullet \rangle$ denotes the average over the nodes in a cluster.
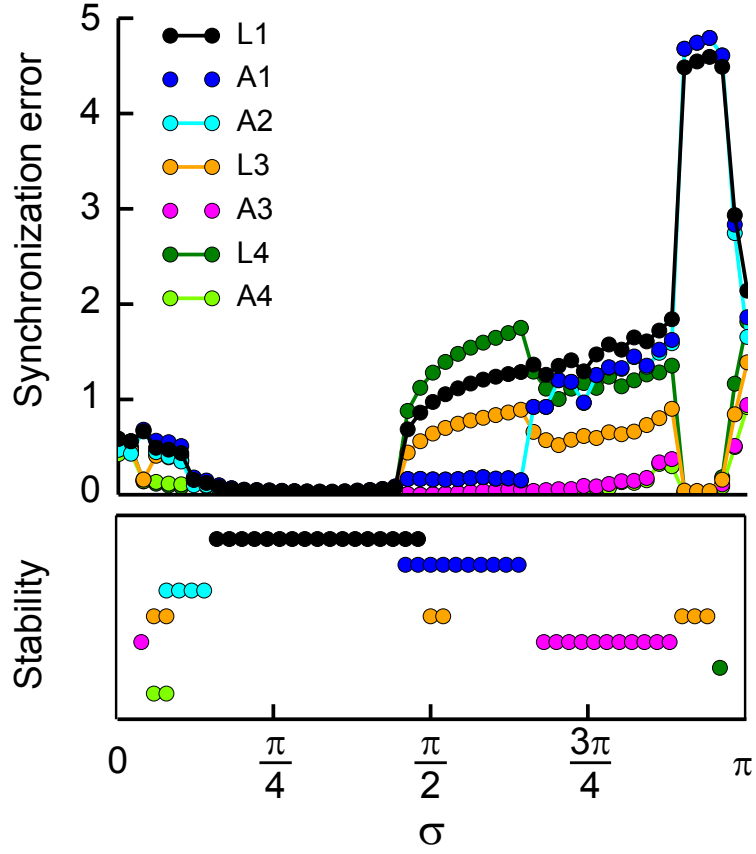
Figure 4.6: The experimental synchronization error for each synchronization pattern as a function of the parameter $\sigma$. Underneath we plot the results of our stability analysis applied to each one of the cluster synchronization patterns, where a colored dot labels the values of $\sigma$ for which the corresponding pattern is stable.

## Chapter 5:  Chimeras in Coupled-Map Lattices

*This chapter is based on work from the following publication*

*Aaron M. Hagerstrom, Thomas E. Murphy, Rajarshi Roy, Philipp Hövel, Iryna Omelchenko, and Eckehard Schöll. Experimental observation of chimeras in coupled-map lattices. Nature Physics, 8(9):658–661, 2012.*

## 5.1   Introduction and outline

Chimera states were first recognized in a ring of coupled phase oscillators by Kuramoto and Battogtokh in 2002 [29]. Networks of phase oscillators are widely studied in part because the phase oscillator model describes the generic behavior of systems near a Hopf bifurcation with weak coupling [28], and in part because in many cases low-dimensional models of infinitely large populations can be constructed [118]. Depending on the strength of the coupling, a large population of globally-coupled phase oscillators will either show synchronous "coherent" behavior, or unsynchronized "incoherent" behavior. When nonlocal coupling is used instead, both behaviors can be present at the same time: networks with nonlocal coupling can have large, coexisting spatial regions of synchrony and incoherence. These regions of qualitatively different behaviors are surprising because the coupling in these models is homogeneous. There's no reason why one particular part of a ring should

synchronize while another part does not. This coexistence of seemingly incongruous behaviors inspired Abrams and Strogatz to name these dynamical states after a creature from Greek mythology with a goat's head, a lion's head, and a snake for a tail [30]. Hundreds of papers have been written about Chimera states exploring various types of coupling, different local dynamics, coupling with time delay, the effect of parameter heterogeneity, their metastability as a function of size, and many other things [30, 119–121, 121–129].

Before 2012, there were no experimental demonstrations of chimeras. Now there are several. This chapter describes one of the first two experimental realizations of chimera states. The other experiment was performed by Mark Tinsley, Simba Nkomo, and Ken Showalter, who observed chimera states in two coupled populations of chemical oscillators [33]. Their experiment was inspired by a theoretical paper from 2008 which presented a low-dimensional analytical model of two coupled populations of phase oscillators [119]. This theoretical paper was also the inspiration for an experiment by Erik Martens, Shashi Thutupalli, Antoine Fourrière, and Oskar Hallatschek, who used metronomes as phase oscillators, and constructed two coupled populations by placing the metronomes on swings coupled by a spring [36]. Chimera states have also been observed in time-delayed feedback loops [37, 38]. Time-delayed systems have an infinite-dimensional phase space which can be thought of as analogous to a spatial domain. Chimera states have also been observed in electrochemical systems including some with global coupling [34, 35].

Many models which display chimera states have nonlocal coupling. In a spatial domain, oscillators are said to be nonlocally coupled if each oscillator has a finite

range of influence, rather than being coupled to the whole system, or only to an infinitesimally small local area. In systems consisting of a finite number of oscillators, coupling is said to be nonlocal if a given oscillator is coupled to other oscillators within a distance that is an appreciable fraction of the system size. Global coupling, in which all oscillators receive the same signal [116], and local coupling [130–135] were much more widely studied prior to the discovery of chimeras, in part because it was hard to think of experimental situations in which nonlocal coupling might come about. Shima and Kuramoto argued that nonlocal coupling could arise in reaction-diffusion systems if one reagent diffused much more slowly than another [31].

When we wrote our paper in 2012, it was generally believed that chimera states require nonlocal coupling. Now, in 2015, chimeras have been described in models with purely local coupling [136] and in both models [137] and experiments [34, 35] with global coupling. It's also worth noting that more than a decade before chimeras in phase oscillators were described by Kuramoto and Battogtokh, Kaneko described dynamical states in globally-coupled iterated maps with a coexistence of a few large synchronized clusters and many small unsynchronized clusters [116]. These states probably deserve to be called chimeras.

The chimera states we describe here exist in a coupled-map lattice (CLM) [130–135] in one or two [138] dimensions. Although we use the term "oscillator" to describe the iterated maps in the experiment, the local dynamics of an individual oscillator are not oscillatory. Each oscillator acts like a chaotic iterated map when it is not coupled to other oscillators. Even though individual oscillators behave chaotically, we will see situations where a network of coupled oscillators is periodic.

The network is updated in discrete time, and so the temporal periodicity of a given lattice site will be an integer number of iterations. In the chimeras we describe, all of the nodes are synchronized, in the sense that the entire system is periodic with the same period. In this case the terms "coherence" and "incoherence" refer to spatial behavior rather than temporal behavior. We use the term coherent to refer to smooth profiles, and incoherent to refer to spatial profiles with a large number of discontinuities. These types of chimeras in coupled map lattice were first theoretically considered and numerically simulated in refs. [139, 140].

### 5.1.1 Organization of this chapter

Section 5.2 describes the chimera states we observed, and the dependence of the dynamics on parameter values in both simulation and experiment. Two parameters are particularly important: the coupling radius $r$, and the coupling strength $\epsilon$.

At large $\epsilon$, we see smooth spatial profiles. At low $\epsilon$, we see incoherent patterns with many spatial discontinuities. Section 5.3 derives an approximation for a critical coupling strength at which a discontinuity develops.

Our chimera states have incoherent regions. These should be thought of as finite-sized regions, rather than thin boundaries between neighboring smooth regions. In Section 5.4, we show simulation data which demonstrates that the incoherent region scales with the number of oscillators, $N$.

We see patterns with different spatial wavenumbers. Intuitively, a smaller coupling radius leads to patterns with higher wavenumber. In Section 5.5 we show

that patterns with different wavenumbers are related by a simple scaling argument.

## 5.2  Coupled-map lattices in experiment

Figure 5.1 shows the experimental setup of the optical CML. This is the same device described in Chapter 4. The device employs a phase spatial light modulator (SLM) and an infrared camera in feedback configuration. Both the SLM and the camera frames are partitioned into an $M \times M$ array of square regions. These regions correspond to nodes in the network of coupled maps. The phase shift $x_{i,j}$ and intensity $\mathcal{I}$ for a given region $(i, j)$ are related by

$$\mathcal{I}(x_{i,j}) = \frac{1}{2} \left(1 - \cos x_{i,j}\right), \qquad i, j = 0, \ldots, M - 1. \tag{5.1}$$

The intensity has been normalized to be between 0 and 1. A lens is used to project an image of the SLM onto an infrared camera, which records the two-dimensional intensity pattern $\mathcal{I}(x_{i,j})$. We construct a network of iterated maps by using the computer to communicate between the camera and the SLM. Time evolution of the network is achieved by iteratively updating the phase applied by each region of the SLM in a way that depends upon the intensity measured by the camera.

### 5.2.1  Chimeras in 1D and 2D

We present results for two different coupling schemes shown schematically in Figures 5.1(b) and 5.1(c). In the one-dimensional (1D) configuration, the elements in the array are arranged as a ring with periodic boundary conditions. The SLM is
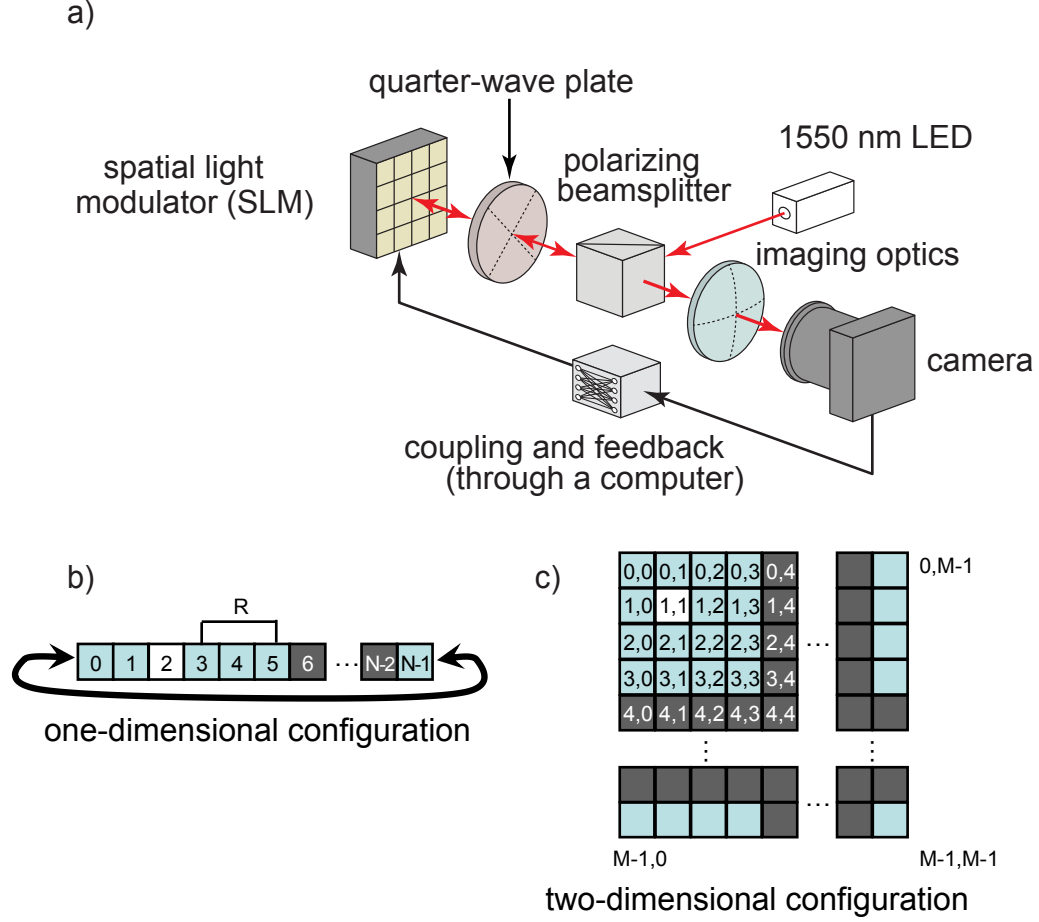
Figure 5.1: Experimental device and coupling configuration. a) Optical configuration. Polarization optics create a nonlinear relationship between the spatially dependent phase shift applied by the SLM and the intensity of the light falling on the camera. Feedback and coupling are implemented using a computer. b) One- and c) two-dimensional coupling configurations are shown schematically. Because the elements are coupled diffusively to their neighbors within a range $R$ in either one or two dimensions with periodic boundary conditions, the coupling is identical for all oscillators.

treated as a 1D lattice with the elements coupled in a raster-ordered arrangement. If $x_i^t$ is the phase of the $i$th element in the ring at the $t$th iteration, and $\mathcal{I}(x_i^t)$ is the intensity measured by the corresponding region in the camera, then the phase is updated according to

$$x_i^{t+1} = 2\pi a \left\{ \mathcal{I}\left(x_i^t\right) + \frac{\epsilon}{2R} \sum_{j=-R}^{R} \left[\mathcal{I}\left(x_{i+j}^t\right) - \mathcal{I}\left(x_i^t\right)\right] \right\} \tag{5.2}$$

where $i = 0, \ldots, N-1$ in the 1D ring configuration and the index $i$ is periodic modulo $N$. Thus each element is coupled diffusively to all of the elements within a distance $R$ on either side, and $\epsilon$ describes the strength of the coupling. The parameter $a$ controls the temporal dynamics of an isolated map. We choose $a = 0.85$ such that the local map $x^{t+1} = f(x^t) \equiv 2\pi a \mathcal{I}(x^t)$ is chaotic with a Lyapunov exponent $\lambda \approx 0.58$.

We also examine a two-dimensional (2D) coupling scheme. In this configuration, each element is coupled to its neighbors within a square region, and the boundary conditions are periodic in both dimensions.

$$x_{i,j}^{t+1} = 2\pi a \left\{ \mathcal{I}\left(x_{i,j}^t\right) + \frac{\epsilon}{4R^2} \sum_{k,l=-R}^{R} \left[\mathcal{I}\left(x_{i+k,j+l}^t\right) - \mathcal{I}\left(x_{i,j}^t\right)\right] \right\} \tag{5.3}$$

Figures 5.2(a) and 5.2(b) characterize the dependence of the dynamics of the 1D and the 2D systems on coupling strength and range by plotting a measure of temporal entropy (see Section 5.2.2) in order to characterize the periodicity of the dynamics. The color maps were obtained through numerical simulation of equations (5.2) and (5.3). A period-2 profile will have an entropy of 1 bit, and a chaotic profile will have an entropy close to 9 bits, since 512 bins were used. We see spatial profiles

91
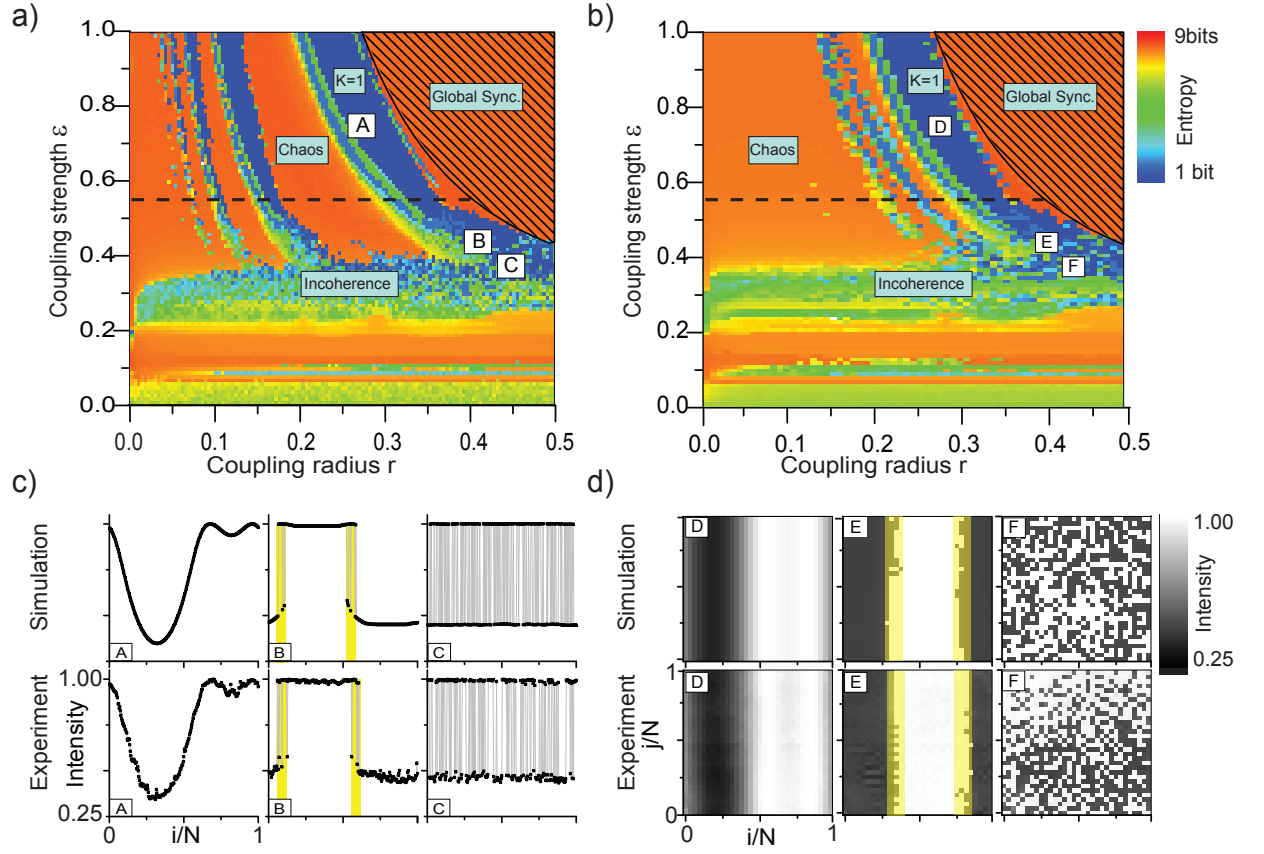
Figure 5.2: Parameter space of the 1D and 2D CML systems. a) Parameter space of the one-dimensional configuration ($N = 256$ elements). Blue corresponds to low entropy and periodicity, orange corresponds to high entropy and chaos. The dashed line indicates the critical coupling strength $\epsilon_c = 0.54$ b) Parameter space of the two-dimensional configuration ($128 \times 128$ lattice). There is a prominent $K = 1$ tongue, and two tongues with more complex spatial patterns. c) Experimental and numerical realizations of the 1D system. In the middle panel, B, the incoherent region is highlighted in yellow. Labels A (coherence), B (chimera), C (incoherence) show positions in the parameter space of panel a). d) Experimental and numerical realizations of the 2D system. In the middle panel, E, the incoherent region is highlighted.

that are periodic in time, as well as profiles that are chaotic in time. There is a rich variety of both coherent and incoherent spatial structures. The thin vertical regions marked $K = 1, 2, 3$ in figure 5.2(a) indicate conditions for which the dynamical state is periodic in time and forms a spatially periodic standing-wave pattern with a spatial wavenumber of $K$. Within each of these regions, there is a transition from spatial coherence to incoherence with decreasing coupling strength $\epsilon$, as predicted in [139, 140].

Equations (5.2) and (5.3) admit a globally synchronous solution. The hatched region in Figures 5.2(a) and 5.2(b) indicate the region in parameter space for which global synchrony is stable, which is identical between the 1D and 2D systems.

A comparison of the 1D and 2D systems reveals that these systems show equivalent behavior within a limited region in parameter space. In the 2D system there is a prominent region marked $K = 1$, which contains profiles that are homogeneous in one direction. Every solution of the 1D problem corresponds to a solution of the 2D problem that is uniform in one direction, i.e., $x_{i,j} = x_i$. While $K = 2, 3 \ldots$ profiles also exist in principle, only the $K = 1$ profile is observed in simulation and experiment in the 2D system within the evolution time we consider. Simulations also reveal two smaller regions that contain complex profiles with spatial structures that cannot be realized in one dimension.

Figure 5.2(c) shows experimental and numerical realizations of three profiles from the $K = 1$ region. The sequence A,B,C shows a progression from spatial coherence to spatial incoherence. All profiles have a temporal period of 2. At a coupling radius $r \equiv R/N = 70/256 \approx 0.27$ and $\epsilon = 0.75$ (A), the profile has a

smooth spatial variation. At $r = 105/256 \approx 0.41$, $\epsilon = 0.44$ (B), the profile shows two large domains of coherent, synchronized behavior separated by narrow but finite, regions of incoherent behavior highlighted in yellow. Numerical evidence indicates that the width of these regions as a fraction of the system size remains constant as N increases, and hence this is not a boundary effect (see Section 5.4). While the entire profile is periodic in time, the dynamics of the coherent and incoherent regions are qualitatively different in their degree of spatial coherence: within the incoherence intervals there are numerous admissible combinations of upper and lower states whose multiplicity scales exponentially with the system size [139]. This mixture of qualitatively different behaviors is analogous to the chimera states discussed in references [29,30,119,122–124], where an array of identical oscillators splits into two domains: one coherent and phase locked, the other incoherent and desynchronized. Unlike the chimeras in continuous-time phase oscillators [29, 30], the generalized chimeras here and in [139,140] have two coherent parts (with high and low intensity, respectively) and two incoherent parts, as a result of their mechanism of nascence from the completely coherent $K = 1$ spatial profile. Finally, at $r = 115/256 \approx 0.45$, $\epsilon = 0.375$ (C), the profile is completely incoherent. The same scenario occurs in the $K = 2$ and $K = 3$ regions and can be interpreted through a spatial rescaling described in Section 5.5.

Figure 5.2(d) shows snapshots of experimental and numerical realizations of the 2D system in a $32 \times 32$ lattice, obtained with similar parameter values to those used in Figure 5.2(b). All of these realizations are periodic in time with period 2, except (E), which has a period of 4 in the experimental realization shown. Like

the 1D system, the 2D system undergoes a coherence-incoherence transition as $\epsilon$ is decreased. At $r = 9/32 \approx 0.28$, $\epsilon = 0.75$, the system exhibits a smooth profile (D). For $r = 13/32 \approx 0.41$ and $\epsilon = 0.44$, there is a chimera-like coexistence of coherence and incoherence (E). Finally, at $r = 14/32 \approx 0.44$ and $\epsilon = 0.375$, the system is fully incoherent (F).

## 5.2.2  Periodicity quantification

In Figures 5.2(a) and 5.2(b), the color of each point corresponds to a single numerical simulation. Lattice sizes of 256 for the 1D case and $128 \times 128$ for the 2D case were used. Initially, the phase of each node is random and uniformly distributed between 0 and $2\pi$. In each simulation we discard 50000 transient iterations. Using the next 5000 iterations, we construct one histogram for each of the $N$ nodes in the network, binning the values the phase achieves in these iterations. 512 bins were used. Thus we estimate $p_i^n$, the fraction of the time that node $i$ will spends in the $n$th bin. From these statistics we obtain the entropy, which is then averaged over the $N$ nodes in the system

$$H = -\frac{1}{N} \sum_{i=0}^{N-1} \sum_{n=0}^{511} p_i^n \log_2 p_i^n. \tag{5.4}$$

We note that for this system the temporal behavior of the whole network is either chaotic or periodic, and the spatial average of the entropy will not differ substantially from the entropy of any given node. We also note that this calculation only characterizes the temporal behavior of the system, and does not distinguish between spatial coherence and incoherence.

## 5.3 Critical coupling strength

The development of a spatial discontinuity can be explained analytically. We derive the critical coupling strength $\epsilon_c$ at which the smooth profile breaks up giving rise to the incoherence regions (B) of figure 5.2(c). Considering the spatially continuous version of equation (5.2) and solutions with wavenumber $K = 1$ and period-2 dynamics in time, the system dynamics are given by alternating profiles $x^0(u)$ and $x^1(u)$ for even and odd time steps, respectively. By evaluating the spatial derivative of this equation with the profiles $x^0(u)$ at the positions where the smooth profiles break up, we obtain two equations which, when multiplied, will yield a condition for the critical coupling strength.

Starting from the system equation (5.2)

$$x_i^{t+1} = f\left(x_i^t\right) + \frac{\epsilon}{2R} \sum_{j=-R}^{R} \left[f\left(x_{j+i}^t\right) - f\left(x_i^t\right)\right], \tag{5.5}$$

where we define the local map as $f(x) = 2\pi a \mathcal{I}(x)$, we obtain its spatially continuous version for $N \to \infty$ and $r = R/N$:

$$
\begin{aligned}
x^{t+1}(u) =& f\left(x^t(u)\right) \\
&+ \frac{\epsilon}{2r} \int_{u-r}^{u+r} \left[f\left(x^t(v)\right) - f\left(x^t(u)\right)\right] dv.
\end{aligned}
\tag{5.6}
$$

Let us consider a solution with wave number $K = 1$ and period-2 dynamics in time. Hence we can reduce the dynamics by even and odd time steps $x^0(u)$ and $x^1(u)$, respectively:

$$x^{1-j}(u) = (1 - \epsilon)f\left(x^j(u)\right) + \frac{\epsilon}{2r} \int_{u-r}^{u+r} f\left(x^j(v)\right) dv \tag{5.7}$$
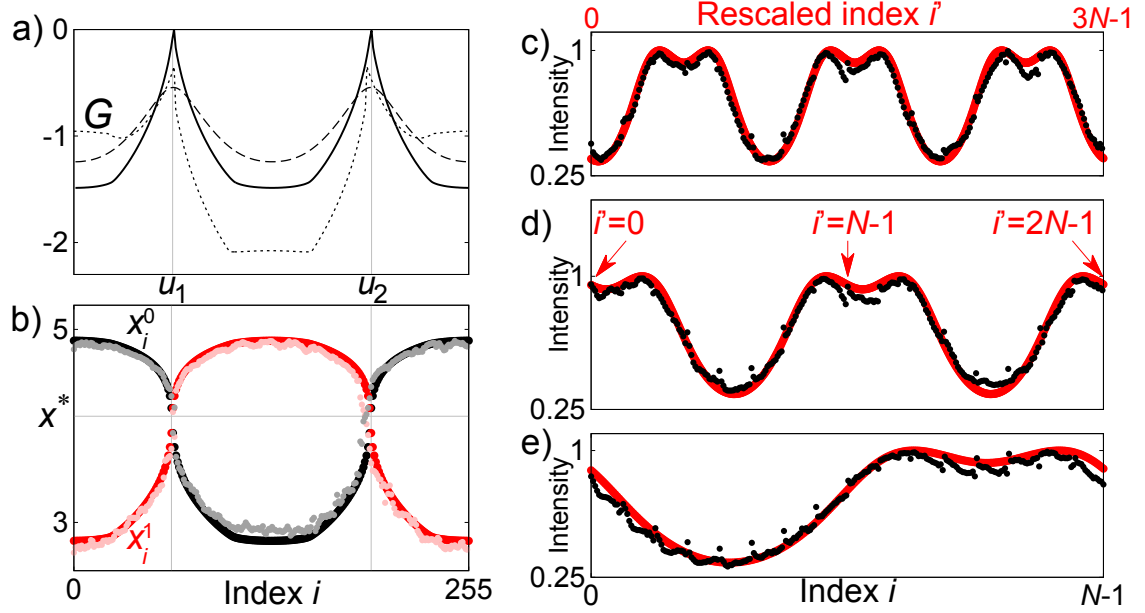
Figure 5.3: Critical coupling and scaling of coherent profiles. a) Condition $G$ for breaking of the smooth profile. The solid curve corresponds to the critical coupling strength $\epsilon_c = 0.54$. The dashed and dotted curves refer to $\epsilon = 0.675 > \epsilon_c$ and $\epsilon = 0.475 < \epsilon_c$, respectively. b) Snapshots of the period-2 solution for even ($x_i^0$ (black)) and odd ($x_i^1$ (red)) time steps at the critical coupling strength of panel (a). The light red and gray dots refer to the experiment. Points $u_1$, $u_2$ are discontinuity points, where the profile breaks, and $x^*$ marks the fixed point of the local map. Other parameters: $N = 256$, $a = 0.85$, $r = 88/256 \approx 0.34$. c)-e) Scaling of coherent intensity profiles. The measured coherent profiles with spatial periods $K = 1, 2, 3$ shown in black for coupling radius (c) $r_3 = 22/256 \approx 0.09$, (d) $r_2 = 33/256 \approx 0.13$, and (e) $r_1 = 66/256 \approx 0.26$. The profile $K = 1$ numerically obtained from equations (5.2),(5.1) and its rescaled profile are shown in red in panels c) and d),e), respectively. Other parameters: $a = 0.85$, $\epsilon = 0.8$, and $N = 256$.

with $j = 0, 1$. Taking the spatial derivative yields

$$\partial_u x^{1-j}(u) = (1 - \epsilon)\partial_u f\left(x^j(u)\right)\partial_u x^j(u) +$$

$$+ \frac{\epsilon}{2r}\left[f\left(x^j(u+r)\right) - f\left(x^j(u-r)\right)\right]. \tag{5.8}$$

At the points where the smooth profile breaks up, the spatial derivative $\partial_u x^j(u)$ becomes infinite. Considering that $\partial_u x^0(u), \partial_u x^1(u)$ diverge to infinity, we can neglect the coupling term on the right-hand side. Multiplying the equations for even and odd time steps we obtain:

$$\partial_u x^0(u)\partial_u x^1(u) = \left[(1 - \epsilon)^2 \partial_u f\left(x^0(u)\right)\partial_u f\left(x^1(u)\right)\right]$$

$$\times \partial_u x^0(u)\partial_u x^1(u), \tag{5.9}$$

which yields the following condition

$$1 = (1 - \epsilon)^2 \partial_u f\left(x^0(u)\right)\partial_u f\left(x^1(u)\right). \tag{5.10}$$

As the local dynamics is governed by the map $f(x) = \pi a(1 - \cos x)$ and its derivative is equal to $f'(x) = \pi a \sin x$, we introduce the function

$$G(u) = (\pi a)^2(1 - \epsilon)^2 \sin(x^0(u))\sin(x^1(u)) - 1 \tag{5.11}$$

as a deviation from the previous condition (5.10).

For fixed coupling radius $r$ and fixed $\epsilon$ we can numerically calculate $x^0(u), x^1(u)$. For the critical coupling strength $\epsilon_c$ the condition $G(u^*) = 0$ holds at discontinuity points $u^*$.

In order to obtain an analytic approximation for the critical coupling strength $\epsilon_c$, we assume $x^0(u) = x^1(u) = x^*$ at the discontinuity points $u^*$, where $x^*$ is a fixed
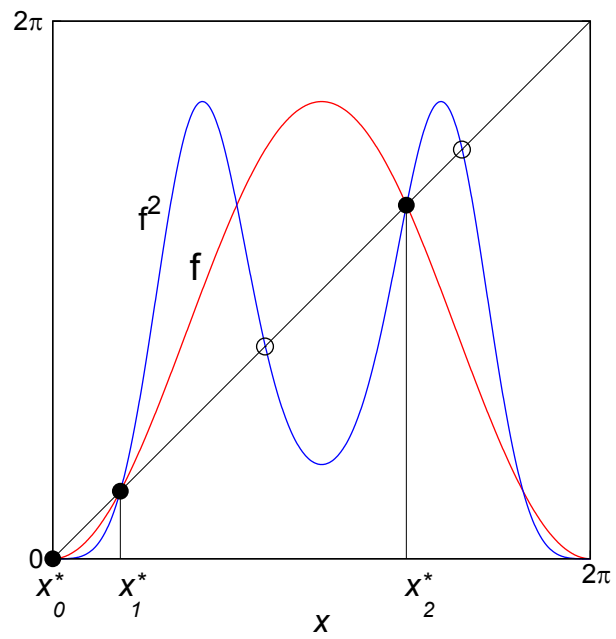
Figure 5.4: Local map $f(x) = 2\pi a \mathcal{I}(x) = \pi a(1 - \cos x)$ (red) and its twice iterate $f^2$ (blue) for $a = 0.85$. The filled and open circles refer to the fixed points of $f$ and the twice iterated $f^2$.

point $x^* = \pi a(1 - \cos x^*)$ of the map, hence

$$G(u) = (\pi a)^2 (1 - \epsilon_c)^2 \sin^2 x^* - 1 = 0. \tag{5.12}$$

This leads to

$$\epsilon_c = 1 \mp \frac{1}{(\pi a)|\sin x^*|}, \tag{5.13}$$

where the minus sign should be chosen since the lower value of $\epsilon_c$ represents the threshold where the smooth profile breaks up with decreasing coupling strength $\epsilon$, and the spatial coherence is lost. The map $f(x) = \pi a(1 - \cos x)$ has three fixed points $x_0^* = 0$, $x_1^* \approx 0.79$, and $x_2^* \approx 4.13$ for $a = 0.85$, as shown in Figure 5.4.

The solutions with $K = 1$ in space and period-2 in time shown in Figure 5.3(b) can be understood qualitatively as follows: part of the network is in the upper state, part is in the lower state, and both states alternate with period 2. These two states correspond very roughly to the two fixed points of the twice iterated map above and below the fixed point $x_2^* \approx 4.13$. They have bifurcated from $x_2^*$ which has become unstable in the twice iterated map, and the discontinuity point between these is the fixed point $x_2^*$ (see Figure 5.4). Hence, the approximation $x^* \approx x_2^*$ in Equation (5.13) leads to $\epsilon_c \approx 0.55$, which is close to the result obtained numerically in Figures 5.3(a) and 5.3(b).

One can even obtain an approximate full analytical solution (for $a > 0.6$) by Taylor expanding the local map $f$ about $\pi$ using

$$\cos x_2^* \approx -1 + \frac{1}{2}\psi^2, \tag{5.14}$$

where $\psi = x_2^* - \pi$. This gives an equation for the fixed point

$$\pi + \psi \approx \pi a \left( 2 - \frac{1}{2}\psi^2 \right) \tag{5.15}$$

and hence

$$\psi \approx \frac{1}{\pi a}(-1 + \sqrt{1 + 2\pi^2 a(2a - 1)}). \tag{5.16}$$

This gives $\psi \approx 0.96$, $x_2^* \approx 4.10$, and $\epsilon_c \approx 0.54$, which agrees with the observed behavior of both the experimental system and simulations to a few percent.

## 5.4   Scaling of the incoherent regions in chimera states with N

To illustrate the relationship between the size of the incoherent regions high-lighted in yellow in Figs. 5.2(c),(d), and the finite size ($N$) of the experimental lattice, we focus on the 1D case in Fig. 5.2(c) panel (B). While these incoherent regions are small, they are finite and not just a boundary between the coherent domains. The size of the incoherent region as a fraction of the system size remains approximately constant as the system size is increased in numerical simulations, which indicates that it is not a finite-size boundary effect. This is shown in Fig. 5.5, which depicts snapshots for $N = 256$ and $N = 1024$, and a decreasing sequence of coupling strengths $\epsilon = 0.44, 0.42$, and $0.40$, with the same coupling radius $r \approx 0.41$ as in panel B of Fig. 5.2(c). Furthermore, Fig. 5.5 demonstrates that the inco-herence regions become wider for decreasing coupling strength $\epsilon$ as expected in the transition scenario from spatial coherence to complete incoherence via chimera states (cf. [139, 140]). The initial conditions in Fig. 5.5 are carefully prepared to
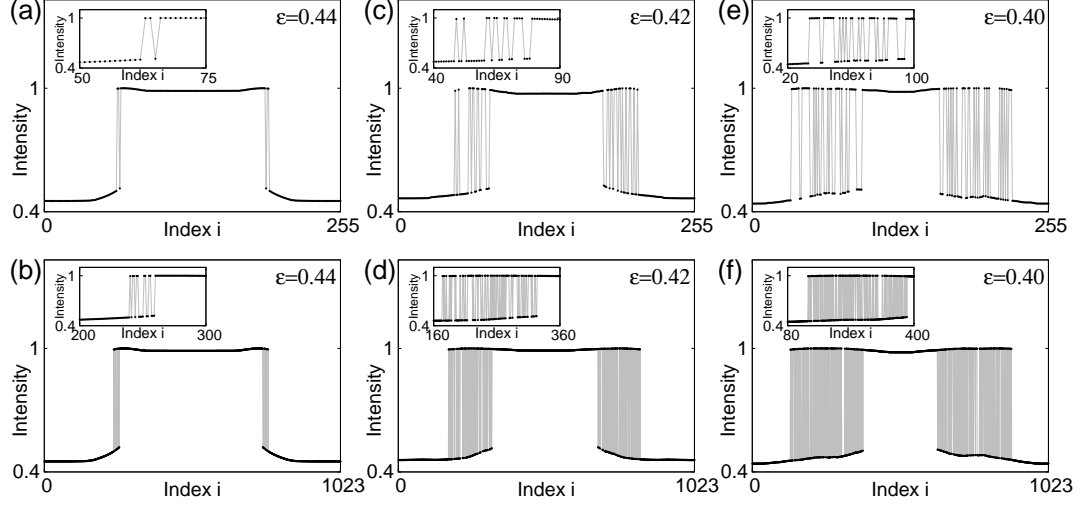
Figure 5.5: Simulations to illustrate scaling with system size of the incoherent regions for the 1D system. Snapshots for (a),(c),(e) $N = 256$, and (b),(d),(f) $N = 1024$. Decreasing coupling strength is used in panels (a),(b) $\epsilon = 0.44$, (c),(d) $\epsilon = 0.42$, (e),(f) $\epsilon = 0.40$. Other parameters: $a = 0.85$, $r = 0.41$. Transients of 1000 time steps were neglected. The insets show the enlarged left incoherence region for each snapshot.

generate chimera states. We divided the ring of $N$ elements into four equal parts, and used $\mathcal{I}(x_i^0 = 4.5) \approx 0.6$ and $\mathcal{I}(x_i^0 = 2.5) \approx 0.9$ on the segments $\dfrac{i}{N} \in \left[-\dfrac{1}{8}, \dfrac{1}{8}\right]$ and $\dfrac{i}{N} \in \left[\dfrac{3}{8}, \dfrac{5}{8}\right]$, respectively, and random sequences of these two values for the other two parts, which contain the incoherent domains as subsets [139, 140]. The experimental measurements presented in Fig. 5.2 were made with random initial conditions. The role of initial conditions in the emergence of chimera states and the existence of multistability needs to be explored in the future.

Figure 5.6: Coherent profiles with space periods $K = 1, 2, 3$ according to equation (5.2) for coupling radius (a) $r_1 = 66/256 \approx 0.26$, 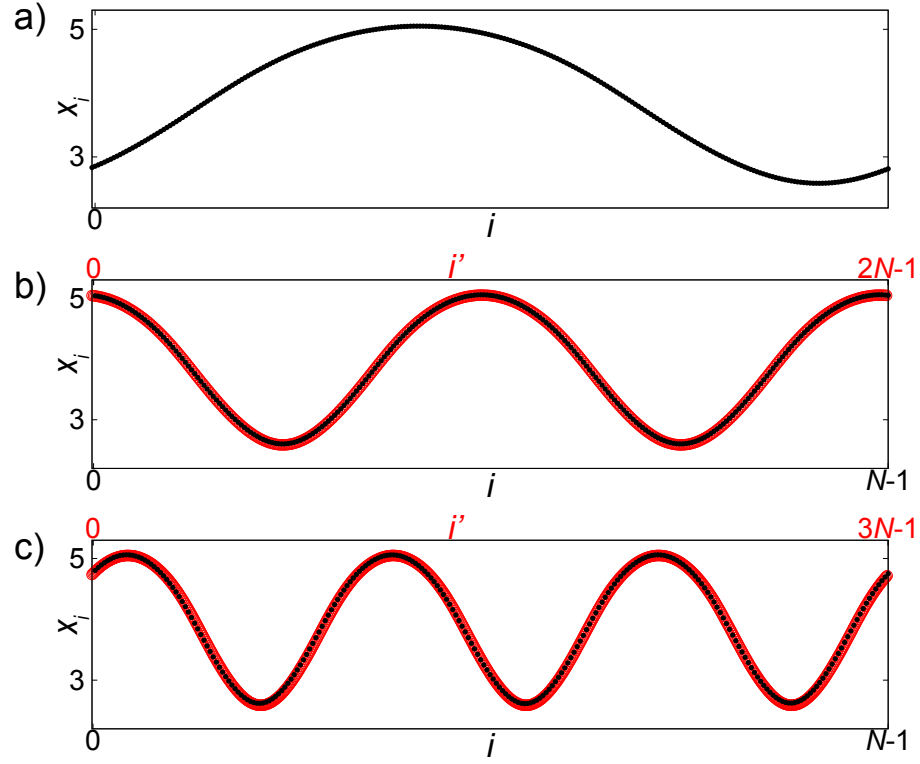(b) $r_2 = 33/256 \approx 0.13$, and (c) $r_3 = 22/256 \approx 0.09$ shown in black. The rescaled coherent profile $K = 1$ in panels (b),(c) is shown in red. Other parameters: $a = 0.85$, $\epsilon = 0.8$, and $N = 256$.

## 5.5 Spatial rescaling and coherent patterns with $K=1,2,3...$

To obtain the scaling relation for coherent profiles, we consider again the thermodynamic limit $N \to \infty$ and the spatially continuous version of system (5.2):

$$x^{t+1}(u) = f(x^t(u)) + \frac{\epsilon}{2r} \int_{u-r}^{u+r} \left[ f(x^t(v)) - f(x^t(u)) \right] dv, \qquad (5.17)$$

where $f(x) = 2\pi a \mathcal{I}(x)$, $r = R/N$ is a coupling radius, and the coherent solution $x_i^t$, $i = 0, \ldots, N-1$, of the system (5.2) approaches a corresponding smooth profile $x^t(u)$, where $u \in [0, 1]$.

In the following, we consider the case that the coupling strength $\epsilon$ is fixed. Let there exist a state $x_{K'}(u)$ with spatial period $K'$. The dynamics of this state is governed by

$$x_{K'}^{t+1}(u) = f(x_{K'}^t(u)) + \frac{\epsilon}{2r} \int_{u-r}^{u+r} \left[ f(x_{K'}^t(v)) - f(x_{K'}^t(u)) \right] dv, \qquad (5.18)$$

The solution $x_{K'}(u)$ will be compared with the state $x_K(u)$ with spatial period $K$. Our goal is to show that the dynamics of $x_{K'}(u)$ is identical to the dynamics of $x_K(\tilde{u})$ at a rescaled space position $\tilde{u} = (uK')/K$ for a correspondingly rescaled coupling radius $\tilde{r} = (rK')/K$. For simplicity, we will consider that $K' = 1$, and we assume that $x_{K'}(u) = x_K(u/K)$. The dynamics of the solution $x_K$ of Equation (5.18) with rescaled $u \to u/K$ and rescaled coupling radius $r \to r/K$ is governed by

$$x_K^{t+1}\left(\frac{u}{K}\right) = f\left(x_K^t\left(\frac{u}{K}\right)\right) + \frac{\epsilon K}{2r} \int_{(u-r)/K}^{(u+r)/K} \left[ f\left(x_K^t(v)\right) - f\left(x_K^t\left(\frac{u}{K}\right)\right) \right] dv, \quad (5.19)$$

Let $v = w/K$, then

$$x_K^{t+1}\left(\frac{u}{K}\right) = f\left(x_K^t\left(\frac{u}{K}\right)\right) + \frac{\epsilon}{2r} \int_{u-r}^{u+r} \left[ f\left(x_K^t\left(\frac{w}{K}\right)\right) - f\left(x_K^t\left(\frac{u}{K}\right)\right) \right] dw. \quad (5.20)$$

104

With the use of the above mentioned assumption $x_K^t(u/K) = x_{K'}^t(u)$, we obtain

$$x_K^{t+1}\left(\frac{u}{K}\right) = f(x_{K'}^t(u)) + \frac{\epsilon}{2r}\int_{u-r}^{u+r}\left[f(x_{K'}^t(w)) - f(x_{K'}^t(u))\right]dw = x_{K'}^{t+1}(u), \quad (5.21)$$

i.e., identical dynamical evolution.

This is depicted in Figure 5.6, which illustrates the scaling of the coherent profiles obtained from numerical simulations of equation (5.2) with $a = 0.85$, $\epsilon = 0.8$, and $N = 256$. Coherent profiles with $K = 1, 2, 3$ for a coupling radius (a) $r_1 = 66/256 \approx 0.26$, (b) $r_2 = 33/256 \approx 0.13$, and (c) $r_3 = 22/256 \approx 0.09$ are shown in black. The rescaled coherent profile for $K = 1$ in the panels (b) and (c) is shown in red.

To conclude this argument, if in the system (5.17) the coupling strength $\epsilon$ is fixed and there exist two solutions $x_{K'}$ and $x_K$ with space periods $K'$ and $K$, respectively, then $x_{K'}(u) = x_K(uK'/K)$ for corresponding coupling radii $r$ and $(rK')/K$, respectively.

## 5.6   Concluding remarks

In this chapter, we showed that the CLM chimeras described in [139, 140] can be implemented in experiment. We also described some of their basic properties, including the development of a spatial discontinuity with decreasing $\epsilon$, and the existence of patterns with different spatial wavenumbers. We also showed that there are both one-dimensional and two-dimensional systems with similar behavior, although, strangely, Chimeras with wavenumbers $K$ other than 1 are not seen in the two-dimensional system. The multistability of the chimera states, however, is an important question that remains unaddressed.

As far as I am aware, it remains a complete mystery why, for large $\epsilon$ there are coherent states and an apparently monostable (up to a translation) attractor, whereas for low $\epsilon$, there are many multistable, incoherent attractors. The argument from Section 5.3 describes the development of a spatial discontinuity with decreasing $\epsilon$ but it does not explain the multistability of incoherent states. When we wrote this paper, we did not know about the application of group theory to cluster synchrony. The incoherent patterns are probably subgroup clusters, and it may be possible to say something about their stability now.

## Chapter 6: Unanswered questions

The majority of this thesis was devoted to describing what we did and why. This Chapter focuses on what we didn't do. The goal of this chapter is to briefly mention some questions that became apparent during our investigation that might lead to interesting future work.

## 6.1 Entropy and the photon-counting feedback loop

Time-delayed feedback loops have an infinite-dimensional phase space, and support high-dimensional dynamics. Generally speaking, the larger the time delay is in comparison to the filter time constants, the higher the dimensionality of the dynamics. To obtain the results presented in Chapters 2 and 3, I deliberately chose long filter time constants in order to observe low-dimensional dynamics. Time series analysis techniques that rely on phase-space reconstruction, like the Cohen-Procaccia procedure, tend not to perform well on high dimensional data, because one needs an exceptionally large amount of samples to fill phase space sufficiently to resolve the shape of the attractor.

From the point of view of random number generation, high-dimensional dynamics may offer additional security compared to low dimensional systems. An

hypothetical attacker who wants to predict the future state of a high-dimensional system might try to perform a phase-space embedding. Or, in other words, they might try to count the number of occurrences of pattern of length $d$, to determine which patterns are most common. The high-dimensionality of the system will pose an obstacle to these methods.

On the other hand, one might be able to predict the dynamics of one chaos-based random number generator by synchronizing a second chaotic system to it. This leads to several interesting questions.

The first question is, how does the synchronization error between two photon-counting feedback loops depend on the photon rate $\lambda_0$? There may be an information-theoretic argument that gives some insight into the synchronization error as a function of $\lambda_0$. The synchronization could be measured using several information-theoretic quantities including mutual information, the Kullback-Liebler divergence, or the Jensen-Shannon divergence. It's not clear which would be best.

The synchronization of two chaotic feedback loops could be used to construct an upper bound for the entropy rate of a random number generator. Consider two unidrectionally coupled feedback loops. The output of the first, which is our random number generator, will be called $X_n$. The second, which will try to synchronize to $X_n$, and therefore predict it, will be called $Y_n$. $Y_n$ will be the output of a feedback loop driven by all of the previous random numbers $X_{n-1}, X_{n-2}, ....$ In other words, the second loop, $Y$ is a model that one can use to predict the next sample, $X_n$. If the two loops are partially synchronized, then the conditional entropy $H(X_n|Y_n) < H(X_n)$. In general, $H(X_n|Y_n) \geq H(X_n|X_{n-1}, X_{n-2}, \dots)$. So it is clearly true that

$h \leq (1/\tau)H(X|Y)$. However, because phase space embeddings of high-dimensional signals don't work very well, the conditional entropy might give a tighter bound on the entropy rate than the Cohen-Procaccia method.

Another issue that could be addressed by synchronization is the effect of noise on the unpredictability of the dynamics. When we started the work on the photon-counting feedback loop, one of our ideas was provide an explicit demonstration that the sensitivity to initial conditions present in chaos amplifies microscopic noise. We still have not done this. However, it is possible to measure finite-time Lyapunov exponents using synchronization between two loops [141]. It should also be possible to perform an analogous experiment with the photon-counting system. This would be an explicit measurement of how the uncertainty in the state of this system grows in time. One might expect diffusive growth ($\sim \sqrt{t}$) of the distance in phase space between two trajectories in the shot-noise dominated regime, and exponential growth in the high-photon rate limit.

## 6.2   Synchronization in networks of coupled systems

In the study of cluster synchrony, we have so far considered both Laplacian coupling and adjacency matrix coupling. We have only done a little bit of work on networks with directed links between nodes. It remains an open question whether any interesting new phenomena are present in the case of directed coupling that are not present with bidirectional coupling.

In my opinion, the biggest unresolved question regarding both chimeras and

cluster synchrony is whether the two phenomena are related. Chimera states are, after all, situations in which a large synchronized cluster forms, while many smaller clusters remain unsynchronized.

So far, we have largely avoided the issue of quantifying the number of possible cluster-synchronous states that a network can have. We did count the number of clusters and subgroups for a few different ensembles of random networks [142], but so far we have not tried to quantify the number of subgroup clusters and Laplacian merged clusters. This quantification would depend on the type of network. Scale-free networks would have different statistics from Erdős-Rényi, for example. All we know is that there are probably a lot of different possible cluster synchronization patterns possible in a given network. Some kind of quantification of these patterns might go a long way towards understanding chimera states.

In the context of coupled-map lattice chimeras, the multistability of chimera states and incoherent states needs to be quantified. Ref [139] argued that the multistability of the incoherent region scales exponentially with the system size. As far as I am aware, it remains a complete mystery why, for large $\epsilon$ there are coherent states with an apparently monostable (up to a translation) attractor, whereas for low $\epsilon$, there are exponentially many multistable, incoherent attractors. The argument from Section 5.3 describes the development of a spatial discontinuity with decreasing $\epsilon$ but it does not explain the multistability of incoherent states. When we wrote [32], we did not know about the application of group theory to cluster synchrony. The incoherent patterns may be subgroup clusters, and it may be possible to say something about their multiplicity and stability now.

Another question regarding coupled map lattice chimeras is why coherent profiles with $K$=2,3,4... are seen in the one-dimensional system, but not in the two dimensional system. This difference can be seen in comparing the parameter-space maps in Figure 5.2(a) and Figure 5.2(a). It is easy to see from inspection of Equations (5.2) and (5.3) that any solution of Equations (5.2) is automatically also a solution of Equation (5.3), if one assumes a spatial profile that is homogeneous in one direction. So, there are three possibilities: either wavenumbers higher than 1 are not stable in two dimensions, the basin of attraction of the higher wave numbers is so small that they are never seen, or the transient times to these states are so long that they are never seen.

On a more global scale, the the biggest question is how (and if) cluster synchronization and chimera states manifest in natural and technological systems. We now know that chimeras are possible in experiments. It remains an open question whether chimeras exist in natural contexts. Another interesting potential connection is that the symmetry-based analysis presented here might be relevant to predicting instabilities in the synchronization of the power grid.

# Bibliography

[1] Henri Poincaré. *Leçons de mécanique céleste: professèes á la Sorbonne. Théorie générale des perturbations planetaire. T. 1*, volume 1. Gauthier-Villars, 1905.

[2] Balthasar van der Pol. Forced oscillations in a circuit with non-linear resistance.(reception with reactive triode). *The London, Edinburgh, and Dublin Philosophical Magazine and Journal of Science*, 3(13):65–80, 1927.

[3] M. L. Cartwright and J. E. Littlewood. On nonlinear differential equations of second order, I. The equation $\ddot{y} + \kappa(1 - y^2)\dot{y} + y = b\lambda\kappa\cos(\lambda t + a)$, $\kappa$ large. *Journal of the London Mathematical Society*, 20:180–189, 1945.

[4] Edward N. Lorenz. Deterministic nonperiodic flow. *Journal of the Atmospheric Sciences*, 20(2):130–141, 1963.

[5] TienYien Li and James A. Yorke. Period three implies chaos. *American Mathematical Monthly*, 82(10):985–992, 1975.

[6] Brian R. Hunt and Edward Ott. Defining chaos. *Chaos*, 25(9):–, 2015.

[7] Stanislaw M. Ulam and John von Neumann. On combination of stochastic and deterministic processes-preliminary report. In *Bulletin of the American Mathematical Society*, volume 53, pages 1120–1120, 1947.

[8] M. Ranferi Gutiérrez, M. A. Reyes, and H. C. Rosu. A note on verhulst's logistic equation and related logistic maps. *Journal of Physics A: Mathematical and Theoretical*, 43(20):205204, 2010.

[9] Per Martin-Löf. The definition of random sequences. *Information and Control*, 9(6):602–619, 1966.

[10] Guido Boffetta, Massimo Cencini, Massimo Falcioni, and Angelo Vulpiani. Predictability: a way to characterize complexity. *Physics Reports*, 356(6):367–474, 2002.

[11] Atsushi Uchida, Kazuya Amano, Masaki Inoue, Kunihito Hirano, Sunao Naito, Hiroyuki Someya, Isao Oowada, Takayuki Kurashige, Masaru Shiki, Shigeru Yoshimori, Yoshimura Kazuyuk, and Peter Davis. Fast physical random bit generation with chaotic semiconductor lasers. *Nature Photonics*, 2(12):728–732, 2008.

[12] Ryohsuke Sakuraba, Kento Iwakawa, Kazutaka Kanno, and Atsushi Uchida. Tb/s physical random bit generation with bandwidth-enhanced chaos in three-cascaded semiconductor lasers. *Optics Express*, 23(2):1470–1490, 2015.

[13] James F. Dynes, Zhiliang L. Yuan, Andrew W. Sharpe, and Andrew J. Shields. A high speed, postprocessing free, quantum random number generator. *Applied Physics Letters*, 93(3):031109, 2008.

[14] Thomas Jennewein, Ulrich Achleitner, Gregor Weihs, Harald Weinfurter, and Anton Zeilinger. A fast and compact quantum random number generator. *Review of Scientific Instruments*, 71(4):1675–1680, 2000.

[15] ID Quantique. White paper: Random number generation using quantum physics. http://www.idquantique.com/wordpress/wp-content/uploads/quantis-whitepaper.pdf, 2010. accessed July 30, 2015.

[16] Michael Wahl, Matthias Leifgen, Michael Berlin, Tino Röhlicke, Hans-Jürgen Rahn, and Oliver Benson. An ultrafast quantum random number generator with provably bounded output bias based on photon arrival time measurements. *Applied Physics Letters*, 98(17):171105, 2011.

[17] Laurent Larger. Complexity in electro-optic delay dynamics: modelling, design and applications. *Philosophical Transactions of the Royal Society A: Mathematical,Physical and Engineering Sciences*, 371(1999), 2013.

[18] Thomas E. Murphy, Adam B. Cohen, Bhargava Ravoori, Karl R.B. Schmitt, Anurag V. Setty, Francesco Sorrentino, Caitlin R.S. Williams, Edward Ott,

and Rajarshi Roy. Complex dynamics and synchronization of delayed-feedback nonlinear oscillators. *Philosophical Transactions of the Royal Society A: Mathematical, Physical and Engineering Sciences*, 368(1911):343–366, 2010.

[19] Y. Chembo Kouomou, Pere Colet, Laurent Larger, and Nicolas Gastaud. Chaotic Breathers in Delayed Electro-Optical Systems. *Physical Review Letters*, 95:203903, 2005.

[20] Michael Peil, Maxime Jacquot, Yanne Kouomou Chembo, Laurent Larger, and Thomas Erneux. Routes to chaos and multiple time scale dynamics in broadband bandpass nonlinear delay electro-optic oscillators. *Physical Review E*, 79:026208, 2009.

[21] Andrew Rukhin, Juan Soto, James Nechvatal, Miles Smid, Elaine Barker, Stefan Leigh, Mark Levenson, Mark Vangel, David Banks, Alan Heckert, et al. NIST special publication 800-22. *A statistical test suite for random and pseudorandom number generators for cryptographic applications*, 2001.

[22] Georges Marsaglia. DIEHARD Test suite. http://www.stat.fsu.edu/pub/diehard/, 1998. accessed July 30, 2015.

[23] O. D'Huys, R. Vicente, T. Erneux, J. Danckaert, and I. Fischer. Synchronization properties of network motifs: Influence of coupling delay and symmetry. *Chaos*, 18:037116, 2008.

[24] V. Nicosia, M. Valencia, M. Chavez, A. Díaz-Guilera, and V. Latora. Remote synchronization reveals network symmetries and functional modules. *Physical Review Letters*, 110:174102, 2013.

[25] G. Russo and J-J. E. Slotine. Symmetries, stability, and control in nonlinear systems and networks. *Physical Review E*, 84:041929, 2011.

[26] C. Zhou and J. Kurths. Hierarchical synchronization in complex networks with heterogeneous degrees. *Chaos*, 16(1):015104, 2006.

[27] L. M. Pecora and T. L. Carroll. Master stability functions for synchronized coupled systems. *Physical Review Letters*, 80(10):2109–2112, 1998.

[28] Kuramoto, Y. . *Chemical Oscillations, Waves and Turbulence*. Springer-Verlag, Berlin, 1984.

[29] Y. Kuramoto and D. Battogtokh. Coexistence of Coherence and Incoherence in Nonlocally Coupled Phase Oscillators. *Nonlinear Phenomena in Complex Systems*, 5(4):380–385, 2002.

[30] Daniel M. Abrams and S. H. Strogatz. Chimera states for coupled oscillators. *Physical Review Letters*, 93(17):174102, 2004.

[31] Shin-ichiro Shima and Yoshiki Kuramoto. Rotating spiral waves with phase-randomized core in nonlocally coupled oscillators. *Physical Review E*, 69(3):036213, 2004.

[32] Aaron M. Hagerstrom, Thomas E. Murphy, Rajarshi Roy, Philipp Hövel, Iryna Omelchenko, and Eckehard Schöll. Experimental observation of chimeras in coupled-map lattices. *Nature Physics*, 8(9):658–661, 2012.

[33] Mark R. Tinsley, Simbarashe Nkomo, and Kenneth Showalter. Chimera and phase-cluster states in populations of coupled chemical oscillators. *Nature Physics*, 8(9):662–665, 2012.

[34] Lennart Schmidt and Katharina Krischer. Clustering as a prerequisite for chimera states in globally coupled systems. *Physical Review Letters*, 114:034101, 2015.

[35] Lennart Schmidt, Konrad Schönleber, Katharina Krischer, and Vladimir García-Morales. Coexistence of synchrony and incoherence in oscillatory media under nonlinear global coupling. *Chaos*, 24(1):013102, 2014.

[36] Erik Andreas Martens, Shashi Thutupalli, Antoine Fourrière, and Oskar Hallatschek. Chimera states in mechanical oscillator networks. *Proceedings of the National Academy of Sciences*, 110(26):10563–10567, 2013.

[37] Laurent Larger, Bogdan Penkovsky, and Yuri Maistrenko. Virtual chimera states for delayed-feedback systems. *Physical Review Letters*, 111(5):054103, 2013.

[38] Laurent Larger, Bogdan Penkovsky, and Yuri Maistrenko. Laser chimeras as a paradigm for multistable patterns in complex systems. *Nature Communications*, 6, 2015.

[39] Robert McCredie May. *Stability and complexity in model ecosystems*, volume 6. Princeton University Press, 2001.

[40] Leonard Mandel and Emil Wolf. *Optical coherence and quantum optics.* 1995. Equation (4) is found in section 14.9.2.

[41] Y. Kouomou Chembo, Laurent Larger, Ryad Bendoula, and Pere Colet. Effects of gain and bandwidth on the multimode behavior of optoelectronic microwave oscillators. *Optics Express*, 16(12):9067–9072, 2008.

[42] Lennert Appeltant, Miguel Cornelles Soriano, Guy Van der Sande, Jan Danckaert, Serge Massar, Joni Dambre, Benjamin Schrauwen, Claudio R Mirasso, and Ingo Fischer. Information processing using a single dynamical node as complex system. *Nature Communications*, 2:468, 2011.

[43] Apostolos Argyris, Dimitris Syvridis, Laurent Larger, Valerio Annovazzi-Lodi, Pere Colet, Ingo Fischer, Jordi García-Ojalvo, Claudio R Mirasso, Luis Pesquera, and K Alan Shore. Chaos-based communications at high bit rates using commercial fibre-optic links. *Nature*, 438(7066):343–346, 2005.

[44] Bhargava Ravoori, Adam B. Cohen, Jie Sun, Adilson E. Motter, Thomas E. Murphy, and Rajarshi Roy. Robustness of optimal synchronization in real networks. *Physical Review Letters*, 107(3):034102, 2011.

[45] Caitlin R. S. Williams, Francesco Sorrentino, Thomas E. Murphy, and Rajarshi Roy. Synchronization states and multistability in a ring of periodic

oscillators: Experimentally variable coupling delays. *Chaos*, 23(4):043117, 2013.

[46] Caitlin R. S. Williams, Thomas E. Murphy, Rajarshi Roy, Francesco Sorrentino, Thomas Dahms, and Eckehard Schöll. Experimental Observations of Group Synchrony in a System of Chaotic Optoelectronic Oscillators. *Physical Review Letters*, 110:064104, 2013.

[47] Adam B. Cohen. Synchronization and prediction of chaotic dynamics on networks of optoelectronic oscillators, 2011.

[48] Bhargava Ravoori. Synchronization of chaotic optoelectronic oscillators: Adaptive techniques and the design of optimal networks, 2011.

[49] Caitlin Rose Sanford Williams. Optoelectronic experiments on random bit generators and coupled dynamical systems, 2013.

[50] J. Doyne Farmer. Chaotic attractors of an infinite-dimensional dynamical system. *Physica D: Nonlinear Phenomena*, 4(3):366–393, 1982.

[51] Aaron Morgan Hagerstrom, Thomas Edward Murphy, and Rajarshi Roy. Harvesting entropy and quantifying the transition from noise to chaos in a photon-counting feedback loop. *Proceedings of the National Academy of Sciences*, 112(30):9258–9263, 2015.

[52] Elaine Barker and John Kelsey. NIST DRAFT Special Publication 800-90b recommendation for the entropy sources used for random bit generation. 2012.

[53] Nicholas Metropolis and Stanislaw Ulam. The Monte Carlo Method. *Journal of the American Statistical Association*, 44(247):335–341, 1949.

[54] Arjen Lenstra, James P Hughes, Maxime Augier, Joppe Willem Bos, Thorsten Kleinjung, and Christophe Wachter. Ron was wrong, Whit is right. Technical report, IACR, 2012.

[55] Zvi Gutterman, Benny Pinkas, and Tzachy Reinman. Analysis of the linux random number generator. In *Security and Privacy, 2006 IEEE Symposium on*, pages 15–pp. IEEE, 2006.

[56] Mike Hamburg, Paul Kocher, and Mark E. Marson. Analysis of Intels Ivy Bridge digital random number generator. http://www.cryptography.com/public/pdf/Intel_TRNG_Report_20120312.pdf, 2012. accessed July 30, 2015.

[57] Taiki Yamazaki and Atsushi Uchida. Performance of random number generators using noise-based superluminescent diode and chaos-based semiconductor lasers. *IEEE Journal of Selected Topics in Quantum Electronics*, 19(4):0600309–0600309, 2013.

[58] David P. Rosin, Damien Rontani, and Daniel J. Gauthier. Ultrafast physical generation of random numbers using hybrid Boolean networks. *Physical Review E*, 87:040902, 2013.

[59] Reidler, I. and Aviad, Y. and Rosenbluh, M. and Kanter, I. Ultrahigh-Speed Random Number Generation Based on a Chaotic Semiconductor Laser. *Physical Review Letters*, 103(2):024102, 2009.

[60] Ido Kanter, Yaara Aviad, Igor Reidler, Elad Cohen, and Michael Rosenbluh. An optical ultrafast random bit generator. *Nature Photonics*, 4(1):58–61, 2009.

[61] Neus Oliver, Miguel C. Soriano, David W. Sukow, and Ingo Fischer. Dynamics of a semiconductor laser with polarization-rotated feedback and its utilization for random bit generation. *Optics Letters*, 36(23):4632–4634, 2011.

[62] Neus Oliver, Miguel Cornelles Soriano, David W. Sukow, and Ingo Fischer. Fast random bit generation using a chaotic laser: approaching the information theoretic limit. *IEEE Journal of Quantum Electronics*, 49(11):910–918, 2013.

[63] Martin Virte, Emeric Mercier, Hugo Thienpont, Krassimir Panajotov, and Marc Sciamanna. Physical random bit generation from chaotic solitary laser diode. *Optics Express*, 22(14):17271–17280, 2014.

[64] Satoshi Sunada, Takahisa Harayama, Peter Davis, Ken Tsuzuki, Ken-ichi Arai, Kazuyuki Yoshimura, and Atsushi Uchida. Noise amplification by chaotic dynamics in a delayed feedback laser system and its application to nondeterministic random bit generation. *Chaos: An Interdisciplinary Journal of Nonlinear Science*, 22(4):047513, 2012.

[65] Takuya Mikami, Kazutaka Kanno, Kota Aoyama, Atsushi Uchida, Tohru Ikeguchi, Takahisa Harayama, Satoshi Sunada, Ken-ichi Arai, Kazuyuki

Yoshimura, and Peter Davis. Estimation of entropy rate in a fast physical random-bit generator using a chaotic semiconductor laser with intrinsic noise. *Physical Review E*, 85(1):016211, 2012.

[66] Takahisa Harayama, Satoshi Sunada, Kazuyuki Yoshimura, Jun Muramatsu, Ken-ichi Arai, Atsushi Uchida, and Peter Davis. Theory of fast nondeterministic physical random-bit generation with chaotic lasers. *Physical Review E*, 85:046215, 2012.

[67] Xiaowen Li, Adam B. Cohen, Thomas E. Murphy, and Rajarshi Roy. Scalable parallel physical random number generator based on a superluminescent LED. *Optics Letters*, 36(6):1020–1022, 2011.

[68] Caitlin R. S. Williams, Julia C. Salevan, Xiaowen Li, Rajarshi Roy, and Thomas E. Murphy. Fast physical random number generator using amplified spontaneous emission. *Optics Express*, 18(23):23584–23597, 2010.

[69] Mario Stipčević and Daniel J. Gauthier. Precise Monte Carlo simulation of single-photon detectors. In *SPIE Defense, Security, and Sensing*, pages 87270K–87270K. International Society for Optics and Photonics, 2013.

[70] Christian Gabriel, Christoffer Wittmann, Denis Sych, Ruifang Dong, Wolfgang Mauerer, Ulrik L. Andersen, Christoph Marquardt, and Gerd Leuchs. A generator for unique quantum random numbers based on vacuum states. *Nature Photonics*, 4(10):711–715, 2010.

[71] Antoine Bérut, Artak Arakelyan, Artyom Petrosyan, Sergio Ciliberto, Raoul Dillenschneider, and Eric Lutz. Experimental verification of Landauer's principle linking information and thermodynamics. *Nature*, 483(7388):187–189, 2012.

[72] James Sethna. *Statistical mechanics: entropy, order parameters, and complexity*, volume 14. Oxford University Press, 2006.

[73] Hugo Touchette. The large deviation approach to statistical mechanics. *Physics Reports*, 478(1):1–69, 2009.

[74] Christopher Jarzynski. Diverse phenomena, common themes. *Nature Physics*, 11(2):105–107, 2015.

[75] Édgar Roldán and Juan M. R. Parrondo. Estimating Dissipation from Single Stationary Trajectories. *Physical Review Letters*, 105:150607, 2010.

[76] M. Cencini, M. Falcioni, E. Olbrich, H. Kantz, and A. Vulpiani. Chaos or noise: Difficulties of a distinction. *Physical Review E*, 62(1):427, 2000.

[77] J. G. Caputo and P. Atten. Metric entropy: An experimental means for characterizing and quantifying chaos. *Physical Review A*, 35:1311–1316, 1987.

[78] C. P. Dettmann, E. G. D. Cohen, and Van Beijeren H. Statistical mechanics: Microscopic chaos from Brownian motion? *Nature*, 401(6756):875–875, 1999.

[79] P. Gaspard, M. E. Briggs, M. K. Francis, J. V. Sengers, R. W. Gammon, J. R. Dorfman, and R. V. Calabrese. Experimental evidence for microscopic chaos. *Nature*, 394(6696):865–868, 1998.

[80] Pierre Gaspard and Xiao-Jing Wang. Noise, chaos, and $(\varepsilon, \tau)$-entropy per unit time. *Physics Reports*, 235(6):291–343, 1993.

[81] David Andrieux, Pierre Gaspard, Sergio Ciliberto, Nicolas Garnier, Sylvain Joubaud, and Artyom Petrosyan. Entropy production and time asymmetry in nonequilibrium fluctuations. *Physical Review Letters*, 98(15):150601, 2007.

[82] D. Andrieux, P. Gaspard, S. Ciliberto, N. Garnier, S. Joubaud, and A. Petrosyan. Thermodynamic time asymmetry in non-equilibrium fluctuations. *Journal of Statistical Mechanics: Theory and Experiment*, 2008(01):P01002, 2008.

[83] Thomas M. Cover and Joy A. Thomas. *Elements of information theory*. John Wiley & Sons, 2012.

[84] Dean Prichard and James Theiler. Generalized redundancies for time series analysis. *Physica D: Nonlinear Phenomena*, 84(3):476–493, 1995.

[85] Aviad Cohen and Itamar Procaccia. Computing the Kolmogorov entropy from time signals of dissipative and conservative dynamical systems. *Physical Review A*, 31:1872–1882, 1985.

[86] James Theiler. Estimating fractal dimension. *Journal of the Optical Society of America A*, 7(6):1055–1073, 1990.

[87] Yakov Borisovich Pesin. Characteristic Lyapunov exponents and smooth ergodic theory. *Russian Mathematical Surveys*, 32(4):55–114, 1977.

[88] J.-P. Eckmann and D. Ruelle. Ergodic theory of chaos and strange attractors. *Reviews of Modern Physics*, 57(3):617, 1985.

[89] Giancarlo Benettin, Luigi Galgani, and Jean-Marie Strelcyn. Kolmogorov entropy and numerical experiments. *Physical Review A*, 14(6):2338, 1976.

[90] Karlheinz Geist, Ulrich Parlitz, and Werner Lauterborn. Comparison of different methods for computing Lyapunov exponents. *Progress of Theoretical Physics*, 83(5):875–893, 1990.

[91] Peter Grassberger and Itamar Procaccia. Measuring the strangeness of strange attractors. *Physica D*, 9:189–208, 1983.

[92] A. E. Motter, S. A. Myers, M. Anghel, and T. Nishikawa. Spontaneous synchrony in power-grid networks. *Nature Physics*, 9(3):191–197, 2013.

[93] A.-L. Do, Johannes Höfener, and Thilo Gross. Engineering mesoscale structures with distinct dynamical implications. *New Journal of Physics*, 14(11):115022, 2012.

[94] T. Dahms, J. Lehnert, and E. Schöll. Cluster and group synchronization in delay-coupled networks. *Physical Review E*, 86:016202, 2012.

[95] Chenbo Fu, Zhigang Deng, Liang Huang, and Xingang Wang. Topological control of synchronous patterns in systems of networked chaotic oscillators. *Physical Review E*, 87(3):032909, 2013.

[96] I. Kanter, M. Zigzag, A. Englert, F. Geissler, and W. Kinzel. Synchronization of unidirectional time delay chaotic networks and the greatest common divisor. *Europhysics Letters*, 93:6003, 2011.

[97] D. P. Rosin, D. Rontani, D. J. Gauthier, and E. Schöll. Control of synchronization patterns in neural-like boolean networks. *Physical Review Letters*, 110(10):104102, 2013.

[98] F. Sorrentino and E. Ott. Network synchronization of groups. *Physical Review E*, 76:056114, 2007.

[99] Vladimir N. Belykh, Grigory V. Osipov, Valentin S. Petrov, Johan A. K. Suykens, and Joos Vandewalle. Cluster synchronization in oscillatory networks. *Chaos*, 18:037106, 2008.

[100] M. Golubitsky, I. Stewart, and D.G. Schaeffer. *Singularities and groups in bifurcation theory*, volume II. Springer-Verlag, New York, NY, 1985.

[101] M. Golubitsky and I. Stewart. *The Symmetry Perspective: From Equilibrium to Chaos in Phase Space and Physical Space*. Berkhäuser-Verlag, Basel, 2002.

[102] Kevin Judd. Networked dynamical systems with linear coupling: Synchronisation patterns, coherence and other behaviours. *Chaos*, 23:043112, 2013.

[103] M. Newman. *Networks, An Introduction.* Oxford University Press, 2011. , Chap.18.

[104] Kenneth S. Fink, Gregg Johnson, Tom Carroll, Doug Mar, and Lou Pecora. Three-oscillator systems as universal probes of coupled oscillator stability. *Physical Review E*, 61(5):5080–5090, 2000.

[105] D. Irving and F. Sorrentino. Synchronization of dynamical hypernetworks: dimensionality reduction through simultaneous block-diagonalization of matrices. *Physical Review E*, 86:056102, 2012.

[106] Alex Arenas, Jurgen Kurths Albert Díaz-Guilera, Yamir Moreno, and Changsong Zhou. Synchronization in complex networks. *Physics Reports*, 469:93–153, 2008.

[107] M. Tinkham. *Group Theory and Quantum Mechanics.* McGraw-Hill, New York, NY, 1964.

[108] William Stein. *SAGE: Software for Algebra and Geometry Experimentation.* http://www.sagemath.org/sage/, http://sage.scipy.org/, 2013.

[109] The GAP Group. *GAP: Groups, Algorithms, and Programming, Version 4.4.* http://www.gap-system.org, 2005.

[110] F. Vallentin. Symmetry in semidefinite programs. *Linear Algebra Appl.*, 430(1):360–369, 2009.

[111] R. Goodman and N.R. Wallach. *Representations and Invariants of the Classical Groups.* Cambridge University Press, 1998.

[112] B. E. Sagan. *The Symmetric Group.* Wadsworth Brooks, Pacific Grove, CA, 1991.

[113] B. D. MacArthur and R. J. Sánchez-García. Spectral characteristics of network redundancy. *Physical Review E*, 80:026117, 2009.

[114] B. D. MacArthur, R.J. Sánchez-García, and J. W. Anderson. On automorphism groups of networks. *Discrete Applied Mathematics*, 156:3525–3531, 2008.

[115] B. Dionne, M. Golubitsky, and I. Stewart. Coupled cells with internal symmetry: I. wreath products. *Nonlinearity*, 9:559–574, 1996.

[116] Kunihiko Kaneko. Clustering, coding, switching, hierarchical ordering, and control in a network of chaotic elements. *Physica D: Nonlinear Phenomena*, 41(2):137–172, 1990.

[117] Francesco Sorrentino, Louis M. Pecora, Aaron M. Hagerstrom, Thomas E. Murphy, and Rajarshi Roy. Cluster Synchronization in Laplacian Coupled Systems: Beyond Symmetries. *Submitted to Physical Review Letters (arXiv preprint arXiv:1507.04381).*

[118] Edward Ott and Thomas M. Antonsen. Low dimensional behavior of large systems of globally coupled oscillators. *Chaos*, 18(3):037113, 2008.

[119] Daniel M. Abrams, Rennie Mirollo, S. H. Strogatz, and Daniel A. Wiley. Solvable model for chimera states of coupled oscillators. *Physical Review Letters*, 101(8):084103, 2008.

[120] Erik A. Martens, Carlo. R. Laing, and Steven. H. Strogatz. Solvable model of spiral wave chimeras. *Physical Review Letters*, 104(4):044101, 2010.

[121] Adilson E. Motter. Nonlinear dynamics: Spontaneous synchrony breaking. *Nature Physics*, 6(3):164–165, 2010.

[122] C. R. Laing. The dynamics of chimera states in heterogeneous Kuramoto networks. *Physica D*, 238(16):1569–1588, 2009.

[123] C. R. Laing. Chimeras in networks of planar oscillators. *Physical Review E*, 81(6):066221, 2010.

[124] C. R. Laing. Fronts and bumps in spatially extended Kuramoto networks. *Physica D*, 240(24):1960–1971, 2011.

[125] Erik A. Martens. Bistable chimera attractors on a triangular network of oscillator populations. *Physical Review E*, 82:016216, 2010.

[126] Erik A. Martens. Chimeras in a network of three oscillator populations with varying network topology. *Chaos: An Interdisciplinary Journal of Nonlinear Science*, 20(4):043122, 2010.

[127] Matthias Wolfrum and Oleh E. Omel'chenko. Chimera states are chaotic transients. *Physical Review E*, 84:015201, 2011.

[128] Gautam C. Sethia, Abhijit Sen, and Fatihcan M. Atay. Clustered chimera states in delay-coupled oscillator systems. *Physical Review Letters*, 100:144102, 2008.

[129] Abhijit Sen, Ramana Dodla, George L. Johnston, and Gautam C. Sethia. Understanding complex systems. (ed.) Atay, F. M. pages pp. 1–41. Springer-Verlag, Berlin, 2010.

[130] Irene Waller and Raymond Kapral. Spatial and temporal structure in systems of coupled nonlinear oscillators. *Physical Review A*, 30:2047–2055, 1984.

[131] K. Kaneko. Overview of coupled map lattices. *Chaos*, 2:279 –282, 1992.

[132] K. Kaneko. *Theory and applications of coupled map lattices*. John Wiley & Sons, Chichester, 1993.

[133] K. Kaneko. Period-doubling of kink-antikink patterns, quasiperiodicity in anti-ferro-like structures and spatial intermittency in coupled logistic lattice. *Progress of Theoretical Physics*, 72(3):480–486, 1984.

[134] Arkady S. Pikovsky, Michael Rosenblum, and Jürgen Kurths. *Synchronization: A universal concept in nonlinear sciences*, volume 12. Cambridge Univerity Press, Cambridge, 2003.

[135] S. Boccaletti, J. Kurths, G. Osipov, D. L. Valladares, and C. S. Zhou. The synchronization of chaotic systems. *Physics Reports*, 366:1–101, 2002.

[136] Carlo R. Laing. Chimeras in networks with purely local coupling. *arXiv preprint arXiv:1506.05871*, 2015.

[137] Gautam C. Sethia and Abhijit Sen. Chimera states: the existence criteria revisited. *Physical Review Letters*, 112(14):144101, 2014.

[138] Mark J. Panaggio and Daniel M. Abrams. Chimera states on a flat torus. *Physical Review Letters*, 110(9):094102, 2013.

[139] Iryna Omelchenko, Yuri L. Maistrenko, Philipp Hövel, and Eckehard Schöll. Loss of coherence in dynamical networks: spatial chaos and chimera states. *Physical Review Letters*, 106:234102, 2011.

[140] Iryna Omelchenko, Bruno Riemenschneider, Philipp Hövel, Yuri L. Maistrenko, and Eckehard Schöll. Transition from spatial coherence to incoherence in coupled chaotic systems. *Physical Review E*, 85:026212, 2012.

[141] Adam B. Cohen, Bhargava Ravoori, Thomas E. Murphy, and Rajarshi Roy. Using synchronization for prediction of high-dimensional chaotic dynamics. *Physical Review Letters*, 101(15):154102, 2008.

[142] Louis M. Pecora, Francesco Sorrentino, Aaron M. Hagerstrom, Thomas E. Murphy, and Rajarshi Roy. Cluster synchronization and isolated desynchronization in complex networks with symmetries. *Nature Communications*, 5, 2014.